

Industrial

Electronics

Biomedical

Civil

Aerospace

Computer

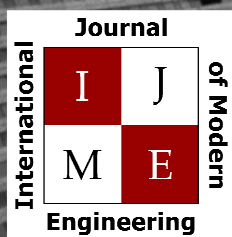
Electrical

Chemical

Mechanical



ENGINEERING



www.ijme.us

Print ISSN: 2157-8052
Online ISSN: 1930-6628



www.iajc.org

INTERNATIONAL JOURNAL OF MODERN ENGINEERING

ABOUT IJME:

- IJME was established in 2000 and is the first and official flagship journal of the International Association of Journal and Conferences (IAJC).
- IJME is a high-quality, independent journal steered by a distinguished board of directors and supported by an international review board representing many well-known universities, colleges and corporations in the U.S. and abroad.
- IJME has an impact factor of **3.00**, placing it among the top 100 engineering journals worldwide, and is the #1 visited engineering journal website (according to the National Science Digital Library).

OTHER IAJC JOURNALS:

- The International Journal of Engineering Research and Innovation (IJERI)
For more information visit www.ijeri.org
- The Technology Interface International Journal (TIIJ).
For more information visit www.tiij.org

IJME SUBMISSIONS:

- Manuscripts should be sent electronically to the manuscript editor, Dr. Philip Weinsier, at philipw@bgsu.edu.

For submission guidelines visit
www.ijme.us/submissions

TO JOIN THE REVIEW BOARD:

- Contact the chair of the International Review Board, Dr. Philip Weinsier, at philipw@bgsu.edu.

For more information visit
www.ijme.us/ijme_editorial.htm

INDEXING ORGANIZATIONS:

- IJME is currently indexed by 22 agencies.
For a complete listing, please visit us at www.ijme.us.

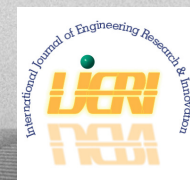
Contact us:

Mark Rajai, Ph.D.

Editor-in-Chief
California State University-Northridge
College of Engineering and Computer Science
Room: JD 4510
Northridge, CA 91330
Office: (818) 677-5003
Email: mrajai@csun.edu



www.tiij.org



www.ijeri.org

INTERNATIONAL JOURNAL OF MODERN ENGINEERING

The INTERNATIONAL JOURNAL OF MODERN ENGINEERING (IJME) is an independent, not-for-profit publication, which aims to provide the engineering community with a resource and forum for scholarly expression and reflection.

IJME is published twice annually (fall and spring issues) and includes peer-reviewed articles, book and software reviews, editorials, and commentary that contribute to our understanding of the issues, problems, and research associated with engineering and related fields. The journal encourages the submission of manuscripts from private, public, and academic sectors. The views expressed are those of the authors and do not necessarily reflect the opinions of the IJME editors.

EDITORIAL OFFICE:

Mark Rajai, Ph.D.
Editor-in-Chief
Office: (818) 677-2167
Email: ijmeeditor@iajc.org
Dept. of Manufacturing Systems
Engineering & Management
California State University-
Northridge
18111 Nordhoff Street
Northridge, CA 91330-8332

THE INTERNATIONAL JOURNAL OF MODERN ENGINEERING EDITORS

Editor-in-Chief:

Mark Rajai
California State University-Northridge

Production Editor:

Philip Weinsier
Bowling Green State University-Firelands

Subscription Editor:

Morteza Sadat-Hossieny
Northern Kentucky University

Executive Editor:

Paul Wilder
Vincennes University

Publisher:

Bowling Green State University-Firelands

Manuscript Editor:

Philip Weinsier
Bowling Green State University-Firelands

Technical Editors:

Michelle Brodke
Bowling Green State University-Firelands

Andrea Ofori-Boadu
North Carolina A&T State University

Marilyn Dyrud
Oregon Institute of Technology

Mandar Khanal
Boise State University

Web Administrator:

Saeed Namyar
Advanced Information Systems

TABLE OF CONTENTS

<i>Editor's Note: Scramjet Combustor Performance</i>	3
Philip Weinsier, IJME Manuscript Editor	
<i>Parametric Sensitivity Study of a Piezoaeroelastic Energy Harvester: The Role of RMS Values on Harvested Voltage</i>	5
Ameen EL-Sinawi, American University of Iraq Sulaimani, IRAQ Isam Janajreh, Khalifa University of Science and Technology, UAE	
<i>Effect of Geometric Modifications on Scramjet Combustor Performance</i>	16
Ayad Alhumadi, Old Dominion University; Alok K. Verma, Old Dominion University	
<i>An Analysis of Bone and Wood Charcoal Color Case-Hardened Steel Samples</i>	26
Alex Johnson, Millersville University of Pennsylvania; Blaise Mibeck, Energy and Environmental Research Center; Chris Beddoe, Energy and Environmental Research Center; Ravindra Thamma, Central Connecticut State University	
<i>Understanding the Influence of Collector Speed on the Properties of Electrospun Membranes for Use in Membrane Distillation</i>	33
Olawale Makanjuola, Khalifa University of Science and Technology; Khadije El Kadi, Khalifa University of Science and Technology; Isam Janajreh, Khalifa University of Science and Technology	
<i>Using Automated Horizon Detection to Determine Image Acquisition Time</i>	40
Curtis Cohenour, Ohio University	
<i>Deep Neural Networks and Universal Approximators</i>	45
Ying Liu, Savannah State University; Asad Yousuf, Savannah State University	
<i>Instructions for Authors: Manuscript Formatting Requirements</i>	51

IN THIS ISSUE (P.16)

SCRAMJET COMBUSTOR PERFORMANCE

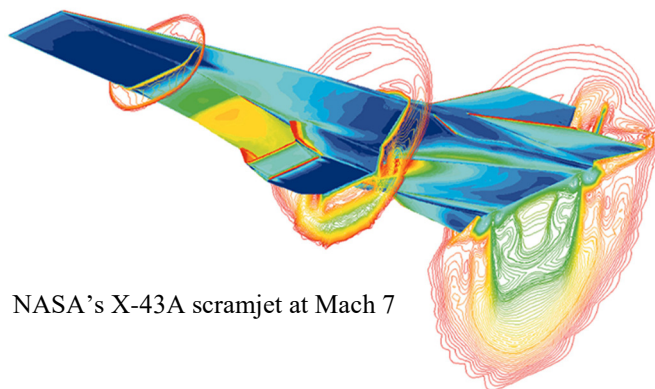
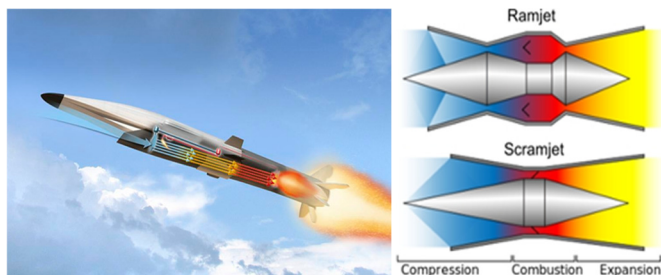
Philip Weinsier, IJME Manuscript Editor

As you likely already know, supersonic speed refers to something traveling faster than the speed of sound—at sea level, and assuming a dry-air air temperature of 68°F (20°C), this would be about 768 mph (1236 km/h). But instead of using actual speeds when referring to supersonic speeds, we typically use Mach numbers. For example, Mach 1 would be 768 mph; Mach 2 would be $2 \times 768 = 1536$ mph; Mach 4.5 would be $4.5 \times 768 = 3456$ mph, etc. Supersonic travel is not that unusual anymore, and speeds of Mach 5 and above have also been achieved and are commonly referred to as hypersonic.

So what things can travel at these hypersonic speeds? Here is one example of an experimental aircraft designed by NASA for hypersonic travel, the X-43A scramjet (supersonic combustion ramjet). The X-43A reigns as the fastest scramjet (Guinness World Records): Mach 9.6 or 7366 mph.

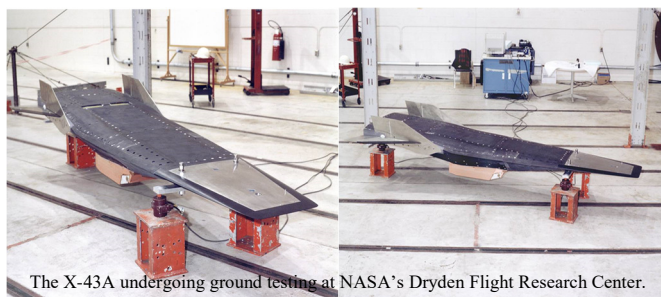


And what types of engines are pushing these aircraft so fast? As it flies, a ramjet uses the high pressure in front of the engine to force air through the tube, where the air is mixed with fuel and ignited. The heated air is then passed through a nozzle to accelerate it to supersonic speeds, which gives the ramjet its forward thrust. This air/fuel mixing technique, however, only works at subsonic speeds. The scramjet is an innovation of ramjet technology in which the combustion chamber is specially designed to operate with supersonic airflow. Note the differences in the renderings below.



NASA's X-43A scramjet at Mach 7

The problem is that combustion in a scramjet still must occur at subsonic speeds in the combustor. Thus, for a vehicle traveling supersonically, the air entering the inlet of the engine must be slowed to subsonic speeds, and shock waves present in the inlet cause performance losses for the propulsion system. Now you are ready for the feature article in this current issue of IJME in which the authors present their ideas and research on control of the air entering the isolator of a scramjet engine. Specifically, because of the high flow speed, the fuel must be mixed with air and be burned in a very short time. Therefore, the authors used two backsteps to create shockwaves in order to decelerate the air to subsonic speeds. This deceleration is required in order to increase the mixing efficiency and enable combustion.



The X-43A undergoing ground testing at NASA's Dryden Flight Research Center.

In this study, then, the effects of the backstep location, height, and angle on a supersonic hydrogen/air jet flame engine with a square cross-sectional area geometry were mathematically investigated. The mathematical model incorporated multi-species Navier–Stokes equations, the K-epsilon model, and the axisymmetric turbulence model. Shockwave effects were examined by changing the backstop location, height, and angle; special consideration was given to the combustion efficiency, thrust, pressure losses, and equivalence ratio of the scramjet combustor.

Editorial Review Board Members

Mohammed Abdallah	State University of New York (NY)	Thongchai Phairoh	Virginia State University (VA)
Paul Akangah	North Carolina A&T State University (NC)	Huyu Qu	Broadcom Corporation
Nasser Alaraje	Michigan Tech (MI)	Desire Rasolomampionona	Warsaw University of Tech (POLAND)
Ali Alavizadeh	Purdue University Northwest (IN)	Michael Reynolds	University of West Florida (FL)
Lawal Anka	Zamfara AC Development (NIGERIA)	Nina Robson	California State University-Fullerton (CA)
Jahangir Ansari	Virginia State University (VA)	Marla Rogers	Fastboot Mobile, LLC
Kevin Berisso	Ohio University (OH)	Dale Rowe	Brigham Young University (UT)
Pankaj Bhambri	Guru Nanak Dev Engineering (INDIA)	Karen Ruggles	DeSales University (PA)
Michelle Brodke	Bowling Green State University (OH)	Anca Sala	Baker College (MI)
Shaobiao Cai	Penn State University (PA)	Alex Sergeev	Michigan Technological University (MI)
Rajab Challoo	Texas A&M University Kingsville (TX)	Mehdi Shabaninejad	Zagros Oil and Gas Company (IRAN)
Isaac Chang	Illinois State University (IL)	Hiral Shah	St. Cloud State University (MN)
Shu-Hui (Susan) Chang	Iowa State University (IA)	Mojtaba Shivaie	Shahrood University of Technology (IRAN)
Rigoberto Chinchilla	Eastern Illinois University (IL)	Musibau Shofoluwe	North Carolina A&T State University (NC)
Phil Cochrane	Indiana State University (IN)	Amit Solanki	Government Engineering College (INDIA)
Curtis Cohenour	Ohio University (OH)	Jiahui Song	Wentworth Institute of Technology (MA)
Emily Crawford	Claflin University (SC)	Carl Spezia	Southern Illinois University (IL)
Dongyang (Sunny)Deng	North Carolina A&T State University (NC)	Michelle Surerus	Ohio University (OH)
Z.T. Deng	Alabama A&M University (AL)	Harold Terano	Camarines Sur Polytechnic (PHILIPPINES)
Sagar Deshpande	Ferris State University (MI)	Sanjay Tewari	Missouri University of Science & Techn (MO)
David Domermuth	Appalachian State University (NC)	Vassilios Tzouanas	University of Houston Downtown (TX)
Marilyn Dyrud	Oregon Institute of Technology (OR)	Abraham Walton	University of South Florida Polytechnic (FL)
Mehran Elahi	Elizabeth City State University (NC)	Haoyu Wang	Central Connecticut State University (CT)
Ahmed Elsayy	Tennessee Technological University (TN)	Jyhwen Wang	Texas A&M University (TX)
Cindy English	Millersville University (PA)	Liangmo Wang	Nanjing University of Science/Tech (CHINA)
Ignatius Fomunung	University of Tennessee Chattanooga (TN)	Boonsap Witchayangkoon	Thammasat University (THAILAND)
Ahmed Gawad	Zagazig University EGYPT	Shuju Wu	Central Connecticut State University (CT)
Kevin Hall	Western Illinois University (IL)	Baijian "Justin" Yang	Purdue University (IN)
Mohsen Hamidi	Utah Valley University (UT)	Eunice Yang	University of Pittsburgh Johnstown (PA)
Mamoon Hammad	Abu Dhabi University (UAE)	Xiaoli (Lucy) Yang	Purdue University Northwest (IN)
Gene Harding	Purdue Polytechnic (IN)	Hao Yi	Chongqing University (CHINA)
Bernd Haupt	Penn State University (PA)	Faruk Yildiz	Sam Houston State University (TX)
Youcef Himri	Safety Engineer in Sonelgaz (ALGERIA)	Yuqiu You	Ohio University (OH)
Delowar Hossain	City University of New York (NY)	Pao-Chiang Yuan	Jackson State University (MS)
Xiaobing Hou	Central Connecticut State University (CT)	Jinwen Zhu	Missouri Western State University (MO)
Shelton Houston	University of Louisiana Lafayette (LA)		
Ying Huang	North Dakota State University (ND)		
Charles Hunt	Norfolk State University (VA)		
Dave Hunter	Western Illinois University (IL)		
Christian Bock-Hyeng	North Carolina A&T University (NC)		
Pete Hylton	Indiana University Purdue (IN)		
John Irwin	Michigan Tech (MI)		
Toqeer Israr	Eastern Illinois University (IL)		
Sudershan Jetley	Bowling Green State University (OH)		
Rex Kanu	Purdue Polytechnic (IN)		
Reza Karim	North Dakota State University (ND)		
Manish Kewalramani	Abu Dhabi University (UAE)		
Tae-Hoon Kim	Purdue University Northwest (IN)		
Chris Kluse	Bowling Green State University (OH)		
Doug Koch	Southeast Missouri State University (MO)		
Resmi Krishnankuttyrema	Bowling Green State University (OH)		
Zaki Kuruppallil	Ohio University (OH)		
Shiyong Lee	Penn State University Berks (PA)		
Soo-Yen (Samson) Lee	Central Michigan University (MI)		
Chao Li	Florida A&M University (FL)		
Dale Litwhiler	Penn State University (PA)		
Mani Manivannan	ARUP Corporation		
G.H. Massiha	University of Louisiana (LA)		
Thomas McDonald	University of Southern Indiana (IN)		
David Melton	Eastern Illinois University (IL)		
Shokoufeh Mirzaei	Cal State Poly Pomona (CA)		
Sam Mryyan	Excelsior College (NY)		
Jessica Murphy	Jackson State University (MS)		
Rungun Nathan	Penn State Berks (PA)		
Arun Nambiar	California State University Fresno (CA)		
Aurenice Oliveira	Michigan Tech (MI)		
Troy Ollison	University of Central Missouri (MO)		
Reynaldo Pablo	Purdue Fort Wayne (IN)		
Basile Panoutsopoulos	Community College of Rhode Island (RI)		
Shahera Patel	Sardar Patel University (INDIA)		

PARAMETRIC SENSITIVITY STUDY OF A PIEZOAEROELASTIC ENERGY HARVESTER: THE ROLE OF RMS VALUES ON HARVESTED VOLTAGE

Ameen EL-Sinawi, American University of Iraq Sulaimani, IRAQ; Isam Janajreh, Khalifa University of Science and Technology, UAE

Abstract

Energy harvested by a piezo-coated airfoil depends on numerous parameters. These parameters affect the magnitude of the piezo voltage, or harvested energy, differently. The piezoaeroelastic model equations are used in this study were coupled and nonlinear and, hence, required an iterative numerical solution in order to evaluate the piezo voltage. The piezoaeroelastic model showed that the energy harvested by the piezo element was high when the structure went through occasional and bounded instability, such as flutter. Optimal harvested energy was produced by careful selection of the system's parameters without compromising structural safety. This work was intended to carry out parametric sensitivity in an attempt to harvest maximum energy, while maintaining structural integrity and safety.

Introduction

The need for intermittent low-power, wireless, and small electronic devices is on the rise, particularly for onboard equipment of unmanned air vehicles (UAV). Researchers have been considering energy harvesting from vibration through the use of piezoelectric materials (Zhou, Liao, & Li, 2005). Several published studies discussed the different techniques and mechanisms implemented that could enhance the level of the harvested power and tune the harvester into broader frequency ranges (Anton & Sodano, 2007; Tang, Yang, & Soh, 2009; Harne & Wang, 2013; Pellegrini, Tolou, Schenk, & Herder, 2013). Amongst these works, the flow-induced vibrations, or aeroelastic phenomena, were less fortunate and research in the area of piezoelectric harvesters utilizing ambient vibrations continues to emerge. Investigations into energy harvesting covers modeling (Erturk & Inman, 2008a), structural experimentations (Abdelkefi, Najjar, Nayfeh, & Ayed, 2011; Khameneifar, Arzanpour, & Moallem, 2013) and integration of piezoelectric materials into the vibrating structure (Yang & Tang, 2009; Kuna, 2010). A piezoaeroelastic airfoil depends on numerous parameters, whereby a well-tuned system can maximize the magnitude of the generated energy. Amongst these parameters are the magnitude of heave or plunge (h), linear stiffness (k_h) and damping (d_h) of the airfoil, torsional stiffness (k_θ) and damping of the airfoil (d_θ), wing span (l), wing mass (m_w), circuit load (Ω), and distance between center of mass and elastic axis (x_θ). In other studies, the authors effected piezoelectric energy harvesting from low-speed

wind and successfully tested experimental models in a wind tunnel that generated 0.1 mW power (Robbins, Marusic, Morris, & Novak, 2006; Akaydin, Elvin, & Andreopoulos, 2012). As far as air vehicles are concerned, buffeting and, to some extent, vortex-induced vibration (VIV) are the two common modes of energy harvesters. Both methods focus on flow-induced vibration and flow-structure interaction. Energy harvesting by VIV has attracted considerable interest in design, modeling, fabrication, and testing (Abdelkefi, Yan, Hajj, & Yan, 2013; Dai, Abdelkefi, Yang, & Wang, 2016; Mehmood, Abdelkefi, Hajj, Nayfeh, Akhtar, & Nuhait, 2013; Dai, Abdelkefi, & Wang, 2014a and 2014b; Mackowski & Williamson, 2013).

The idea came about in 2008 by the pioneering experimental work of Erturk and Inman (2008b) in which they used an airfoil-based aeroelastic—through micro-fiber composites (MFCs)—piezoelectric-integrated transducer for energy harvesting. On their airfoil (133 mm span x 127 mm chord length), four M8557PIMFC piezoceramic patches were installed and reported $7\mu\text{W}$ or harvested power when the airfoil was subjected to large angle of attack (20°), an electrical resistance of 98 k Ω , and a free stream speed of 15 m/s. Anton and Inman (2008) showed that a unmanned aerial vehicle (UAV) prototype—with a wing span of 1.8m x 1.1m, a weight of 0.9 kg, equipped with thin (0.3mm) and light-weight (3g) MFC M8507-P1 sheets (10.2cmx1.6cm), and installed near the roots of the wings—reported that the harvested energy was sufficient to fully charge the operational battery of the UAV.

From a modeling standpoint, much of the work in the area of UAV energy harvesting has been based on a lumped-mass model with a two-degree-of-freedom system of heave/plunging and pitching motions, as reported in the work of Bryant and Garcia (2009a and 2009b). Later work also performed wind tunnel flow-induced fluttering to the NACA0012 airfoil; however, the results did not describe the influence of the wing section geometry on the linear flutter speed nor flutter frequency, due to the dominance of the structural properties of the aeroelastic systems over the aerodynamic loads. They did indicate, however, a strong relationship between wing geometry (span, chord, and airfoil), wind speed, and the amount of harvested energy. Zhu's group (Zhu & Peng, 2009; Zhu, 2011; Zhu, Haase, & Wu, 2009) used similar 2DOF modeling for harvesting energy from heaving and pitching of a foil attached to an actuator system that feeds in a prescribed motion. The system consisted of a 2D thin-plate structural model and a 3D nonline-

air boundary-element model. As self-exciting motion was missing, and without the use of a transduction mechanism, their results did not capture the true physics of the energy harvester and is, thus, subject to debate. Niell and Elvin (2009) focused on the electromechanical aspect of the flutter speed on a cantilever pipe equipped with piezoelectric damping. They investigated the influence of piezoelectric coupling on the critical flutter speed, load resistance, capacitance, and location, and reported their dependence and controllability. Furthermore, they reported on the intimate and direct relationship between the piezoelectric electromechanical coupling coefficient and flutter speed. As for piezoelectric capacitance, it was shown to have a small effect on the flutter speed for the short circuit, while any increase in its value for the open circuit was accompanied with a decrease in flutter speed. These latter results indicate that an increase in the capacitance of the piezoelectric material is associated with a decrease in the electromechanical stiffness of the harvester.

Another study (Erturk, Vieira, Marqui, & Inman, 2010) investigated a frequency domain analysis and experimental validations for a 2DOF typical section as a wing-based piezoaeroelastic energy harvester. In their study, they focused on the problem of harvesting energy at the flutter boundary and analyzed the influence of piezoelectric coupling on linear flutter speed. They generated 10.7 mW of power for an electrical load resistance of 100 kΩ, and aligned the freestream velocity with a linear flutter speed of 9.30 m/s. Water flow-induced vibration, similar to wind flow, was extensively investigated. A piezoelectric polymer energy harvester was used in two studies (Taylor, Burns, Kammann, Powers, & Welsh, 2001; Allen & Smits, 2001) to convert flow energy in oceans and rivers into electrical energy. Song, Shan, Lv, and Xie (2015) used an upright cylinder energy harvester with a vortex-induced piezoelectric energy harvester in water and generated 84.49W. Two tandem cylinders undergoing VIV in water was investigated and produced 533W of power (Shan, Song, Fan, & Xie, 2016).

A review of the use of aeroelastic vibrations for energy harvesting was recently reported by Abdelkefi (2016). Recommendations in the field were discussed, including mathematical modeling, realistic loadings, and small-size power conditioning circuit optimization, in addition to prototype fabrication of energy harvesters. As the governing system has been discussed in many of the cited studies, a sweeping sensitivity study of the multiple harvester parameters was disbursed across several studies and thereby under different setups and conditions. Therefore, inferring the parametrical influence and their quantifications is not a simple task, particularly under the combined coupling of the fluid, structure, and electrical power generation, adding complexity and challenge to the problem. Nevertheless, harvesters with high flow efficiency now represent an increasing area of research interests.

This current research attempts to bridge this gap by performing a study of the effect of each of the system's parameters on the energy harvested from a piezoaeroelastic system. Conclusive findings on the relationship between parameters and the optimal energy harvested in such systems is presented here.

Methodology

Harvester Formulation

The authors' structural model was based on a 2DOF simple cantilever beam for the heave and pitching of a lumped-parameter model. Figure 1 depicts the form of the mass-spring-damper system. The cantilever equivalent values are the mass, spring stiffness, and damping coefficients, given by Equation 1:

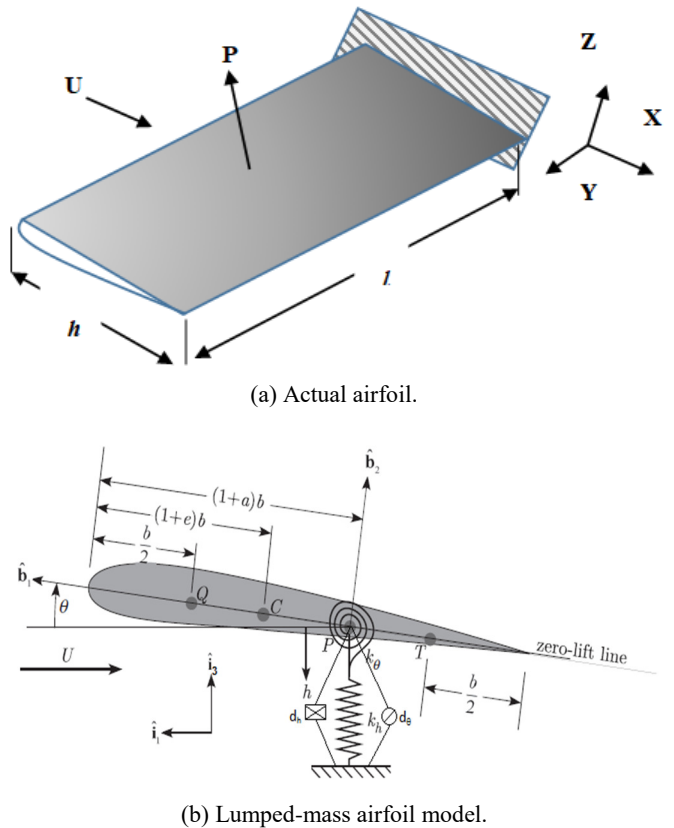


Figure 1. A cantilever wing subjected to point load, due to aerodynamic flow.

$$M\ddot{z} + C\dot{z} + Kz = F \quad (1)$$

where, M is the inertia matrix; C and K are the damping coefficient and the stiffness matrices of the spring in the lumped-parameter model, respectively; F is the loading matrix for air flow; and, z is the net displacement of the mass.

Here the dynamics of the system can be analyzed to obtain the natural frequency, $\omega_n = \sqrt{\frac{K}{M}}$, and damping ratio, $\zeta = \frac{C}{2\sqrt{MK}}$, which are dependent on material stiffness, damping coefficient, and density. The cantilever beam stiffness is $K = \frac{3EI}{l^3}$, where E is the elasticity modulus of the material; I is the area moment of inertia for the cross section of the beam; and, l is the length (span) of the beam. The system can be extended to include the piezoelectric effect by coupling the Lagrange equations. The dynamics of the overall system are expressed by Equation 2 (Abdelkefi, 2016):

$$m_t \ddot{h} + m_w x_\theta b \ddot{\theta} + d_h \dot{h} + k_h(h)h - \frac{\gamma \mathcal{N}}{l} = -L \quad (2.a)$$

$$m_w x_\theta b \ddot{h} + I_p \ddot{\theta} + d_\theta \dot{\theta} + k_\theta(\theta)\theta = M_L \quad (2.b)$$

$$C_p^{eq} \dot{v} + \frac{v}{R_l} + \gamma \dot{h} = 0 \quad (2.c)$$

where, h is the plunging or heave; θ is the pitch angle; v is the generated voltage; b is the semi-chord length; $x_\theta = \frac{r_{cg}}{b}$ is the normalized distance between the center of mass and the elastic axis; I_p is the mass moment of inertia about the elastic axis where the reference point P is taken; L is the aerodynamic lift; M_L is the moment about the elastic axis; d_h and d_θ are the damping coefficients for the plunge and pitch; and, k_h and k_θ are the corresponding transverse and torsional structural stiffnesses, respectively.

In this current study, the effect of non-linear stiffness was not explored; rather, fixed values were used instead of polynomial shapes in the form of Equations 3 and 4:

$$k_h(h) = k_{h_0} + k_{h_1}h + k_{h_2}h^2 + \dots \quad (3)$$

$$k_\theta(\theta) = k_{\theta_0} + k_{\theta_1}\theta + k_{\theta_2}\theta^2 + \dots \quad (4)$$

The coupled system can be written in terms of the variables h , θ , and v , as given in Equation 5:

$$\begin{pmatrix} m_t & m_w x_\theta b & 0 \\ m_w x_\theta b & I_p & 0 \\ 0 & 0 & C_p^{eq} \end{pmatrix} \begin{pmatrix} \ddot{h} \\ \ddot{\theta} \\ \dot{v} \end{pmatrix} + \begin{pmatrix} d_h & 0 & \frac{\gamma}{l} \\ 0 & d_\theta & 0 \\ \gamma & 0 & \frac{1}{R_l} \end{pmatrix} \begin{pmatrix} \dot{h} \\ \dot{\theta} \\ v \end{pmatrix} + \begin{pmatrix} k_h(h) & 0 \\ 0 & k_\theta(\theta) \\ 0 & 0 \end{pmatrix} \begin{pmatrix} h \\ \theta \end{pmatrix} = \begin{pmatrix} -L \\ M_L \\ 0 \end{pmatrix} \quad (5)$$

The state space system can also be rearranged and written as shown in Equation 6:

$$\begin{pmatrix} \dot{h} \\ \dot{\theta} \\ \ddot{h} \\ \ddot{\theta} \\ \dot{v} \end{pmatrix} = \mathbf{A} \begin{pmatrix} h \\ \theta \\ \dot{h} \\ \dot{\theta} \\ v \end{pmatrix} + \mathbf{B} \begin{pmatrix} 0 \\ 0 \\ -L \\ M_L \\ 0 \end{pmatrix} \quad (6)$$

The state vector, x , is defined as

$$x = (x_1 \ x_2 \ x_3 \ x_4 \ x_5)^T = (h \ \theta \ \dot{h} \ \dot{\theta} \ v)^T$$

and the input to the system as

$$u = (0 \ 0 \ -L \ M_L \ 0)^T$$

The problem is now setup in the state-space form, as described in Equation 7:

$$\dot{x} = \mathbf{A}x + \mathbf{B}u \quad (7)$$

The predictor-corrector method can be exploited for solving this equation, as it leverages the benefits of explicit and implicit methods that have been widely used (Abdelkefi 2016; Hamming, 1959; Nayfeh & Mook, 1979; Nayfeh, 2016). The difference between the predicted and corrected values provides a relative error of the solution and allows for tuning of the algorithm. The algorithm considers a differential equation with a time derivative and is written as shown in Equation 8:

$$\dot{y} = f(t, y) \quad (8)$$

The Adams-Bashworth-Moulton (ABM) method is used to solve for y , which is a fourth-order method, and the solution for y_{k+1} requires $y_k \dots y_{k-3}$. An initialization step is used to compute the first three points— y_0 , y_1 , and y_2 —by using the Runge Kutta method. Subsequent time steps can be predicted using the predictor, and the resultant is used implicitly as corrector, as shown in Equations 9a and 9b:

$$p_{k+1} = y_k + \frac{h}{24}(-9f_{k-3} + 37f_{k-2} - 59f_{k-1} + 55f_k) \quad (9.a)$$

$$y_{k+1} = y_k + \frac{h}{24}(f_{k-2} - 5f_{k-1} + 19f_k + 9f_{k+1}) \quad (9.b)$$

In general, the incoming wind results in aerodynamic load in the form of aerodynamic pressure distribution on the flying wing. This load can also be reduced into point lift and moment loads per the right-hand side term in Equation 5. The introduction of this load formulates the piezoaerodynamic problem that needs to be solved. The aerodynamic loads cause different modal responses and, depending on the structural properties and geometry, delineate the harvested energy (Hamming, 1959). The self-excited vibratory motion of fluttering is caused by coupled aerodynamic effects (i.e.,

the increase of wind speed and absence of sufficient structural damping). Table 1 lists the model parameters discussed in the work by Anton and Sodano (2007).

Table 1. Nominal model parameter values of the piezoelectric-aerodynamic coupled system.

VARIABLE	VALUE
m_w	1.5 kg
k_h	2860 N/m
d_h	7.5 kg/s
m_f	8.5 kg
k_θ	2×10^6 Nm/rad
d_θ	0.01 kgm^2/s
R_l	10k Ω
γ	1.55×10^{-3} N/v
C_p^{eq}	1 μF

Structural Damping

As noted previously, the focus of this current study was to study fluttering without compromising the integrity of the structure. Therefore, structural damping was required, which is classically induced via the inclusion of viscoelastic layering of the structure. This technique was present in the vehicle to absorb the cabin vibration and noise (Nayfeh and Mook, 1979). Alternatively, and considering the UAV wing application, the entire wing can be made of a viscoelastic material, which is readily available and inexpensive. Among those are different types of polyolefin (PE, PP, PS, etc.), which is considered a suitable material for small-scale wings. To this end, low-density polyethylene (LDPE) used in 3D printing was utilized in the fabrication of the wing itself and in preparation of the testing samples in order to assess the damping characteristic of the simulated model. Although the wing consisted of NACA0012 with a 3:1 span-to-cord ratio, the 3D-printed test samples were prepared at sizes of 40x10x4 mm and tested in both tensile and cantilever configurations using Instron-5kN and TA-Q800DMA instruments under static and dynamic (frequency sweep) imposed displacement, respectively.

These tests were used in order to obtain the mechanical properties of the material and, eventually, the overall stiffness and damping ratio for the wing configuration. Static testing was used to extract the Young's modulus, whereas dynamic testing (DMA) was used to determine the viscoelastic behavior of the polymeric wing presented by the complex modulus. The static test was conducted when the sample was fixed in the Instron (5kN capacity load cell) machine vertically and subjected to quasi-static imposed dis-

placement. For the DMA, the sample sat upright as a fixed-end cantilever beam and a sinusoidal displacement were induced at distance a from the fixed end. This sinusoidal strain ($\varepsilon(t)$) resulted in dynamic tensile stress ($\sigma(t)$); but, due to the viscoelasticity property of the LDPE, a phase shift was induced per the stress, strain, and the resulting Young's modulus of Equations 10-12, respectively:

$$\sigma(t) = \sigma_o \sin(\omega t + \delta) \quad (10)$$

$$\varepsilon(t) = \varepsilon_o \sin(\omega t) \quad (11)$$

$$E(t) = E_o \sin(\omega t + \delta) \quad (12)$$

where, δ is the phase angle between σ and ε .

The values for σ and E can be broken down into two components—one in-phase and the other 90° out-of-phase—to define the two moduli [i.e., the storage $E'(\omega)$ and the loss $E''(\omega)$]. These are given in Equation 13:

$$\sigma(t) = \varepsilon_o [E'(\omega) \sin(\omega t) + E''(\omega) \cos(\omega t)] \quad (13)$$

The first right-hand term is a measure of elastic energy, which is fully recovered, whereas the second right-hand term is a measure of the dissipated energy in the form of unrecoverable heat. Their ratio, E''/E' is the loss tangent or $\tan(\delta)$. As per Equation 12, the moduli are frequency dependent. At low frequencies, E' is nearly the same as the quasi-static E and displays negligible E'' contribution. However, as the frequency increases, E'' approaches E' and shifts from behaving nearly elastic to strongly viscoelastic. As the beam sample was fixed at one end, it was subjected to 15 values in a frequency sweep. This allowed capturing of both the storage E' and loss E'' moduli as functions of the frequency.

Results and Discussion

Flutter/Wing Material Analysis

Figure 2 shows the results of the tensile stress testing for the three different grades of LDPE. These quasi-static results obtained by Instron-5kN enable one to infer the elastic moduli. These values were 16.678, 42.264, and 482.187 MPa, measured at 0.2% strain for each of the soft, medium, and hard LDPE, respectively. The geometry, along with the measured/inferred experimental properties, can be used to determine the dynamic properties of the wing, particularly the stiffness (k) and natural response frequency (ω_n). Specifically, the stiffness is the k_h term in Equation 5. Table 2 lists the sample data and the inferred natural frequencies of each of the three samples. The concentrated load (F) near the

middle of the cantilever sample that was used, gave a maximum deflection $\hat{\delta}_{\max}$ according to Equation 14, and the beam stiffness is given according to Equation 15:

$$\hat{\delta}_{\max} = Fa^2(3l - a) / 6EI \quad (14)$$

$$k = 6EI / a^2(3l - a) \quad (15)$$

where, a is the span distance measured from the cantilever fixed end, having a length l , modulus E , and area moment of inertia I .

Table 2. Geometric and material properties of the cantilever beam samples (i.e., soft, medium, and hard).

Mat	Mass (g)	ρ (kg/m ³)	I (m ⁴)	E (Mpa)	K MPa.m	ω_n (rad/s)	ζ
Soft	1.280	800	4.91e-11	16.68	0.01487	3.41	0.348
Mid	1.440	900	4.91e-11	42.26	0.03768	5.12	0.150
Hard	1.600	1000	4.91e-11	482.1	0.42998	16.4	0.057

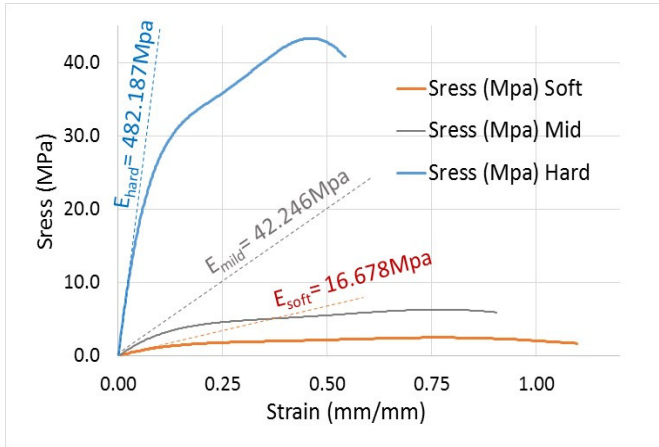
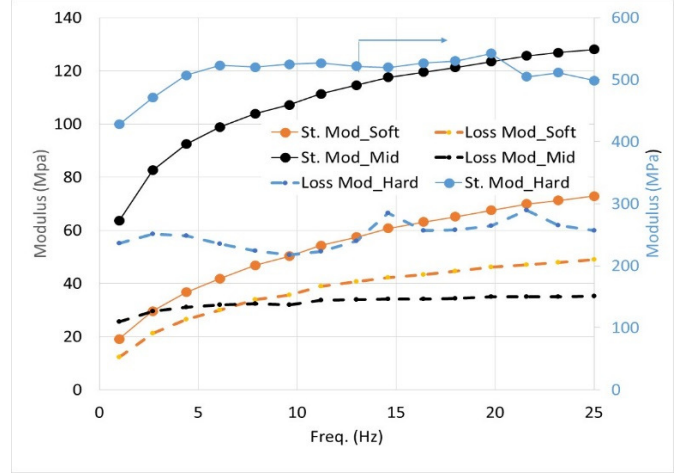
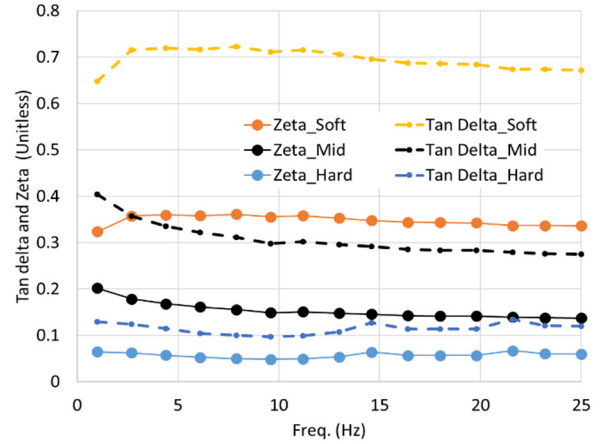


Figure 2. Results of the quasi-static stress-strain of the different LDPE and their moduli.

The damping coefficient, d_h , of Equation 5 was assessed by the measurement of the storage (E') and loss modulus (E'') using the DMA test results. Figure 3 indicates that these are material properties and depend on the forcing frequency, which is brought by the aerodynamic load. Table 2 illustrates the fact that the targeted range of the DMA falls within the operation and near the natural frequency of the cantilever samples, and confirms the well-behaved beam response. Both the storage and loss moduli continued to increase with respect to the frequency in adherence to the classical behavioral of viscoelastic materials. However, as the frequency approached the resonating/natural beam frequency, the behavior continued to show banded moduli, due to the presence of ample viscoelastic damping, particularly for the soft and medium rigid samples.



(a) Storage modulus and loss moduli.



(b) Tan delta and zeta (damping ratio).

Figure 3. Cantilever beam samples from soft, medium, and hard materials.

These samples were characterized with an overwhelming damping, shown by the tan delta plot that averaged nearly 0.70, 0.33, and 0.11 for the soft, medium, and harder LDPE, respectively. The harder samples showed slightly fluctuating behavior. This was mainly due to a decreased availability of damping (i.e., ≈ 0.11). It should be noted that storage modulus and stiffness are linearly related and $\tan(\delta)$ is a direct measure of the damping ratio and is written per the work of Gade and Herlufsen (1994) as shown in Equation 16:

$$\xi = \tan(\delta) / 2 \quad (16)$$

This results in damping ratios (ξ) of 0.348, 0.15, and 0.057 for the soft, medium, and hard sample beams, respectively. Hence, with the evaluated stiffness and damping ratio, one can proceed to evaluate system response.

System Solution

Figure 4 shows the instantaneous values of voltage (V) when the wing's linear stiffness is $k_h = (EI / 3l^3) = 3 \times 10^3$ N/m, where V , as well as other parameters, are all functions of time. Varying the stiffness between $1e3$ and $3e3$ produces results similar to Figure 4 but with different instantaneous values. RMS maps the time domain values of each variable to a single point, thus generating a clearer relationship between experimental parameters and the voltage. Figure 4(f) shows the lift force for a free stream wind speed that was held constant at 55 m/s. Figure 5 shows the RMS values of V as a function of the transverse wing stiffness k_h , where increasing k_h from 1 kN/m to 3 kN/m reduces the RMS voltage by 37%. This was expected, as increased wing stiffness reduces heave h and, subsequently, reduces the piezo bending strain. Figure 5(b) shows that the increased transverse stiffness caused a 2% decrease in RMS of the torsional displacement θ , which had little effect on the piezo voltage, because V depends mostly on the magnitude of bending strain. Furthermore, Figure 5(c) shows an increase in the heave velocity with an increase of transverse stiffness, as expected since increasing the stiffness increases the natural frequency and in turn the velocity.

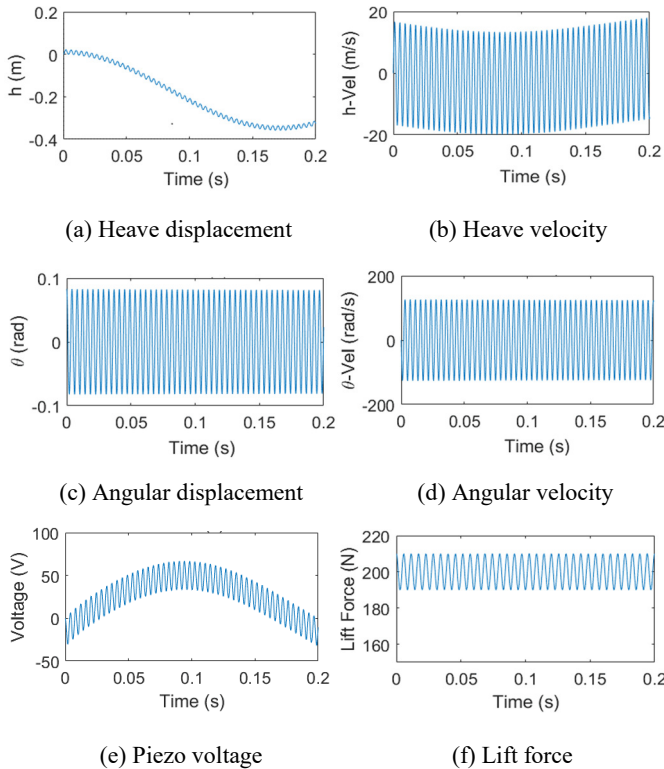


Figure 4. Piezo voltage for actual values of transverse stiffness at $k_h = 3$ kN/m.

Figure 6(c) shows that increasing the torsional stiffness had little effect on the voltage, because it had negligible effect on the bending strain values. Figure 6 does show, however, that increasing the torsional stiffness resulted in increased torsional velocity, because of the increase in the torsional resonance frequency.

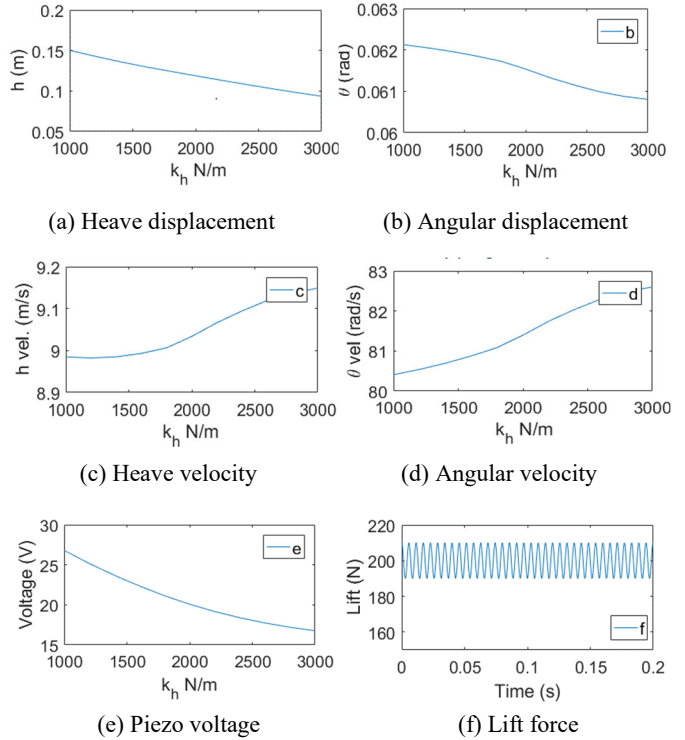


Figure 5. RMS values, effect of transverse wing stiffness (k_h) on piezo voltage.

Figure 7 shows that increasing the circuit load (Ω) caused a significant increase in the voltage, because constant heave (strain) will produce constant current in the piezo and by increasing the load (Ω) the voltage increased ($V = RI$), where I is the circuit current. Furthermore, increasing the load resulted in decreased heave and heave velocity because of the increased dissipation of energy in the resistor. Clearly, increased voltage does not necessarily imply an increase in the energy harvested, because the current drops, thus causing the overall power to drop, since $P = VI = V^2 / R$.

Increased wingspan (l) increased the voltage, because wing bending stiffness is inversely proportional to the cube of the span—i.e., $k_h = (EI / 3l^3)$. Figure 8 shows that increased span caused increased heave and bending strain and, thus, increased the voltage, where increasing the span from $1m$ to $3m$ caused the voltage to increase by 16%. Figure 9 shows the relationship between the voltage and wing mass, where increased the wing mass (m_w) had almost the same effect as decreased transverse stiffness of the wing.

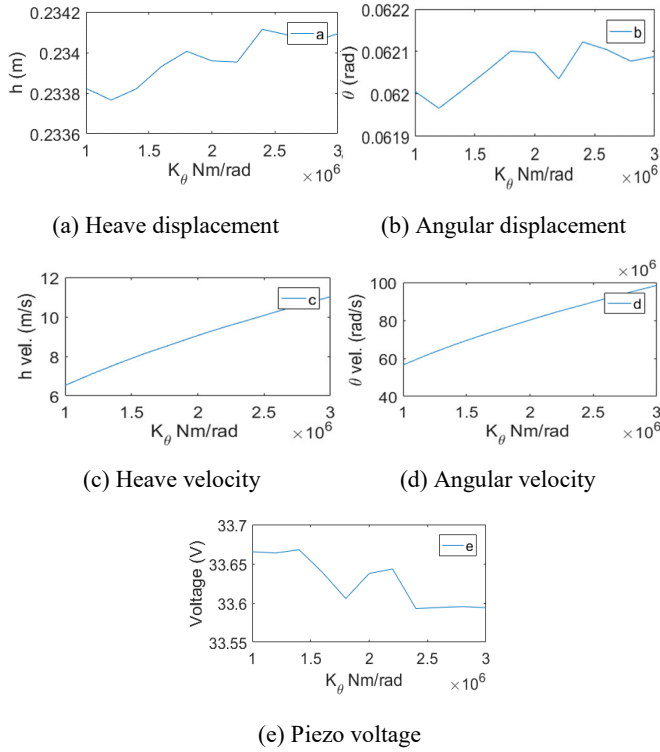


Figure 6. RMS values, effect of wing torsional stiffness k_θ on voltage V.

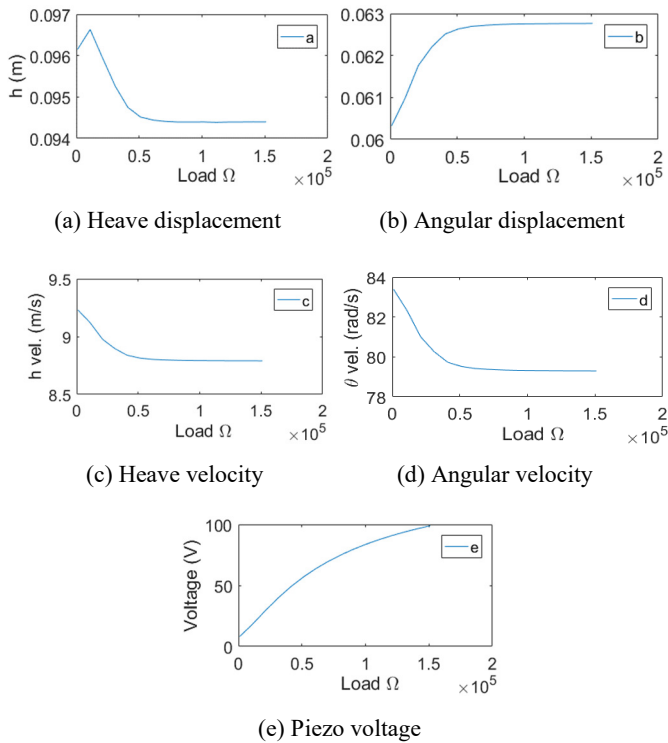


Figure 7. RMS values, effect of circuit load (Ω) on the Piezo voltage.

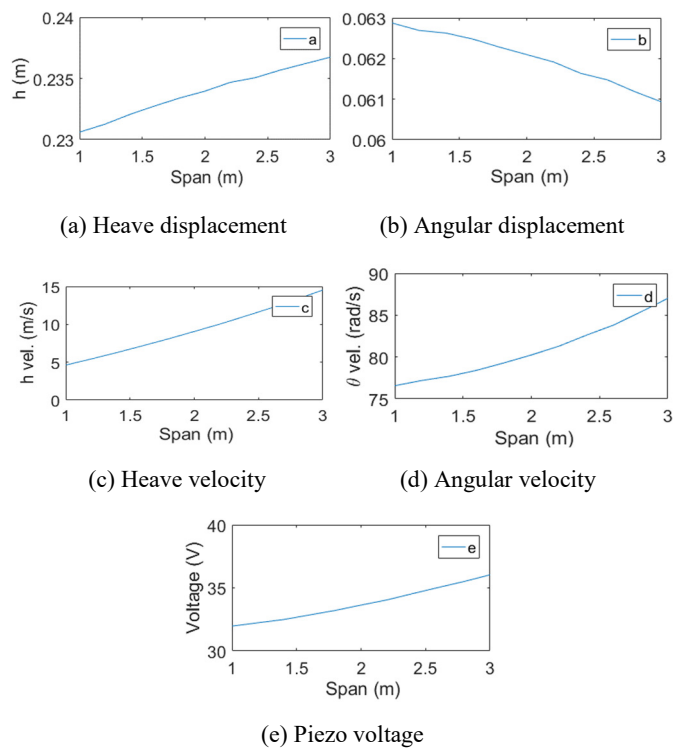


Figure 8. RMS values, effect of wing span (l) on the system behavior and piezo voltage.

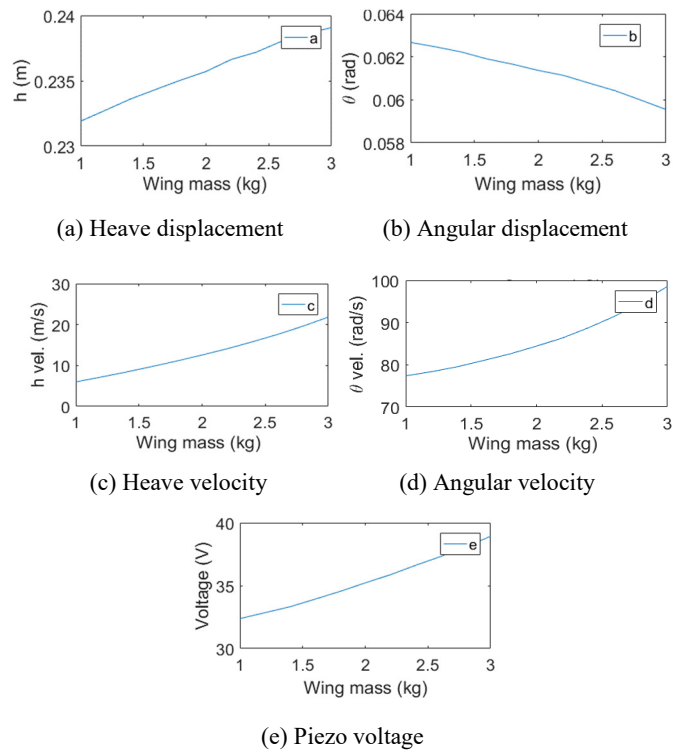


Figure 9. RMS values, effect of wing mass (m_w) on the system's behavior.

Both increased the heave and eventually increased the voltage. This falls directly from the relationship between the resonant frequency and both mass and stiffness, since, $\omega_n = \sqrt{k/m}$ where decreasing the stiffness or increasing the mass has the same effect on the resonant frequency and hence the heave. The effect of increasing (x_θ) on voltage (V) clearly shows a similar effect to increasing the torsional stiffness, because they both contribute to an increase in torque on the wing. Figure 10 is similar to Figure 6 in that they both show an increase in angular displacement. The increase in the voltage in Figure 10 is attributed to the slight increase in the bending strain, due to an increase in the torsional stress as a direct outcome of increasing torque. Both cases depict a small increase in the voltage of about 6%.

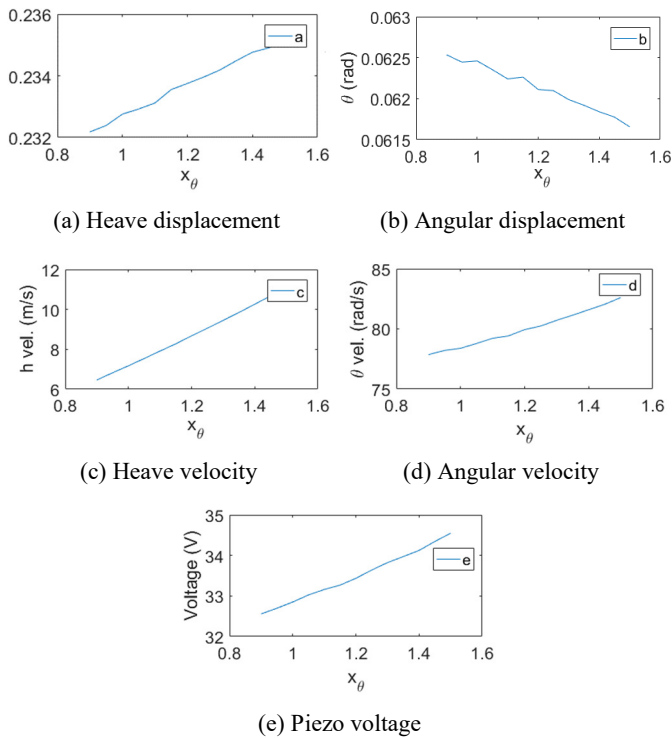


Figure 10. RMS values, effect of (x_θ) on the piezo voltage.

Figures 11 and 12 show that damping had a decreasing effect on the voltage and that the overall value of the voltage had decreased by 6% when the transverse damping was increased from 1 kg/s to 15 kg/s. A similar effect was also seen when the torsional damping was increased from 0 to 0.2 kg.m²/s. The voltage drop in this case was negligible, compared to the considerable increase in damping. However, although the magnitude of damping had increased significantly in both transverse and torsional directions, the damping ratio remained very low, due to the high structural stiffness in corresponding directions.

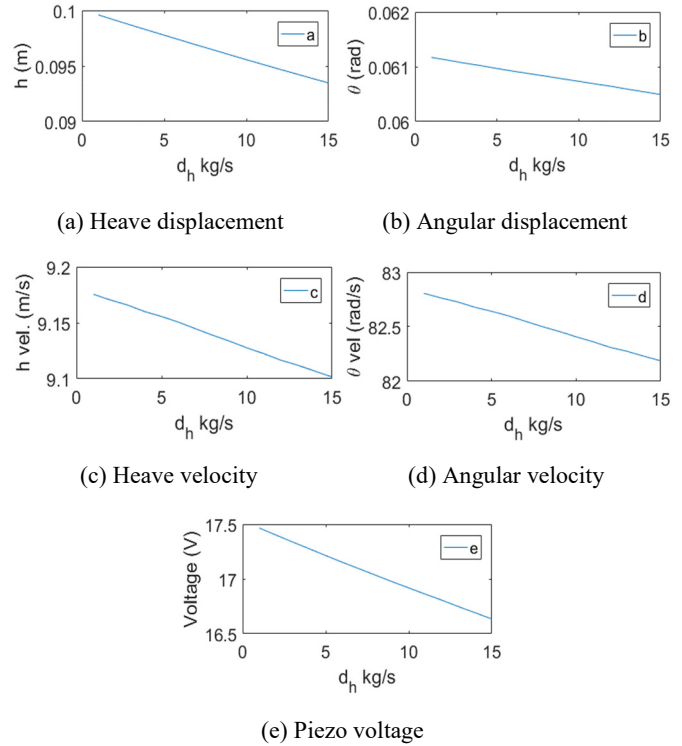


Figure 11. RMS values, effect of transverse damping (d_h) on the piezo voltage.

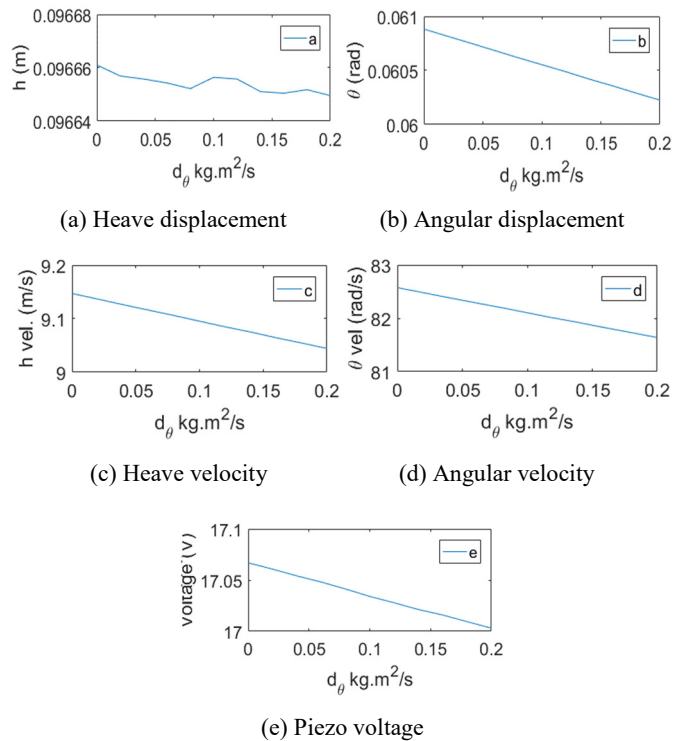


Figure 12. RMS values, effect of torsional damping (d_θ) on the piezo voltage.

Conclusions

Energy harvesting by a piezo-coated airfoil depends on numerous parameters that affect the magnitude of the piezo voltage (i.e., harvested energy) differently. The piezoaeroelastic model equations were coupled with a nonlinear system that required a numerical solution to evaluate the piezo voltage. The piezoaeroelastic model showed that the energy harvested by the piezo element was high when the structure went through occasional bounded instability (i.e., flutter). In this study, each of the parameters was varied between low and high values, while keeping all other parameters at nominal settings while the magnitude of the piezo voltage was evaluated. Since the system was dynamic and coupled, the value of the piezo voltage was time dependent. Therefore, root mean square (RMS) values of all inputs and outputs of the system were evaluated instead of their instantaneous values, and the overall effect of each parameter on the voltage was delineated. Conclusions drawn from this work can be summarized as follows: Transverse stiffness had the highest effect on the voltage harvested, where tripling the stiffness caused a decrease in the voltage by 37%, indicating an inverse relationship between stiffness and harvested energy. Decreasing the wing mass had a similar effect. Therefore, it was concluded that increasing the transverse resonant frequency of the structure resulted in a decrease in the energy harvested.

Damping in both pitch and heave directions had little effect on the energy harvested. This was attributed to the low damping ratio in the structure to begin with. Therefore, increasing the damping by an order of magnitude had a negligible effect on the voltage, mainly because the damping ratio remained low due to the much higher stiffness of the wing structure and the inherent low natural damping in the structure. Increased wingspan increased the voltage, where tripling the wingspan resulted in a 16% increase in the voltage. This was directly related to the first conclusion, where increasing the wing span reduced the stiffness of the wing and increased the bending strain, and subsequently increased the voltage.

Changes in the pitch direction parameters (except x_θ) had little effect on the voltage, indicating that they are less important when designing an energy harvesting system of this type. However, the coupling between heave and pitch had a slight effect on the voltage. Increasing (x_θ) increased the heave velocity and caused a 6% increase in the voltage. Increasing the circuit load increased the voltage but decreased the overall power of the harvester.

Acknowledgments

The authors acknowledge the support of the American University of Iraq-Sulaimani, IRAQ, and Khalifa University of Science and Technology, AD, UAE.

References

- Abdelkefi, A. (2016). Aeroelastic energy harvesting: A review. *International Journal of Engineering Science*, 100, 112-135.
- Abdelkefi, A., Najjar, F., Nayfeh, A. H., & Ayed, S. B. (2011). An energy harvester using piezoelectric cantilever beams undergoing coupled bending-torsion vibrations. *Smart Materials and Structures*, 20(11). doi: 10.1088/0964-1726/20/11/115007
- Abdelkefi, A., Yan, Z., Hajj, M. R., & Yan, Z. (2013). Performance analysis of galloping-based piezoaeroelastic energy harvesters with different cross-section geometries. *Journal of Intelligent Material Systems and Structures*, 25(2), 246-256. doi: <https://doi.org/10.1177/1045389X13491019>
- Akaydin, D., Elvin, N., & Andreopoulos, Y. (2012). The performance of a self-excited fluidic energy harvester. *Smart Materials and Structures*, 21(2). doi: 10.1088/0964-1726/21/2/025007
- Allen, J. J., & Smits, A. J. (2001). Energy harvesting eel. *Journal of Fluids and Structures*, 15(3-4), 629-640.
- Anton, S. R., & Inman, D. J. (2008). Vibration energy harvesting for unmanned aerial vehicles. *Proceedings of SPIE*. doi: 10.1117/12.774990
- Anton, S. R., & Sodano, H. A. (2007). A review of power harvesting using piezoelectric materials (2003-2006). *Smart Materials and Structures*, 16(3), 1-21.
- Bryant, M., & Garcia, E. (2009a). Development of an aeroelastic vibration power harvester. *Proceedings of the SPIE Sixteenth International Symposium on Smart Structures and Materials + Nondestructive Evaluation and Health Monitoring*. doi: 10.1117/12.815785
- Bryant, M., & Garcia, E. (2009b). Energy harvesting: A key to wireless sensor nodes. *Proceeding of the SPIE Second International Conference on Smart Materials and Nanotechnology in Engineering*. doi: 10.1117/12.845784
- Dai, H. L., Abdelkefi, A., & Wang, L. (2014a). Theoretical modeling and nonlinear analysis of piezoelectric energy harvesting from vortex-induced vibrations. *Journal of Intelligent Material Systems and Structures*, 25(14). doi: 10.1177/1045389X14538329
- Dai, H. L., Abdelkefi, A., & Wang, L. (2014b). Piezoelectric energy harvesting from concurrent vortex-induced vibrations and base excitations. *Nonlinear Dynamics*, 77(3), 967-981.
- Dai, H. L., Abdelkefi, A., Yang, Y., & Wang, L. (2016). Orientation of bluff body for designing efficient energy harvesters from vortex-induced vibrations. *Applied Physics Letters*, 108, 175-195. doi: 10.1063/1.4941546
- Erturk, A., & Inman, D. J. (2008a). Issues in mathematical modeling of piezoelectric energy harvesters. *Smart Materials and Structures*, 17. doi: 10.1088/0964-1726/17/6/065016
- Erturk, A., & Inman, D. J. (2008b). A distributed parameter electromechanical model for cantilevered piezoelectric

- energy harvesters. *Journal of Vibration and Acoustics*, 130(4). doi:10.1115/1.2890402
- Erturk, A., Vieira, W. G. R., Marqui, C. D., & Inman, D. J. (2010). On the energy harvesting potential of piezoaeroelastic systems. *Applied Physics Letters*, 96(18). doi: 10.1063/1.3427405
- Gade, S., & Herlufsen, H. (1994). Digital Filter techniques vs. FFT Techniques for Damping Measurements, Bruel & Kjaer Technical Review, No. 1, 1994.
- Hamming, R. W. (1959). Stable predictor-corrector methods for ordinary differential equations. *Journal of the ACM*, 6(1), 37-47.
- Harne, R. L., & Wang, K. W. (2013). A review of the recent research on vibration energy harvesting via bi-stable systems. *Smart Materials and Structures*, 22(2). doi: 10.1088/0964-1726/22/2/023001
- Khameneifar, F., Arzanpour, S., & Moallem, M. (2013). A piezoelectric energy harvester for rotary motion applications: Design and experiments. *IEEE/ASME Transactions on Mechatronics*, 18(5), 1527-1534.
- Kuna, M. (2010). Fracture mechanics of piezoelectric materials—Where are we right now? *Engineering Fracture Mechanics*, 77(2), 309-326.
- Mackowski, A. W., & Williamson, C. H. K. (2013). An experimental investigation of vortex-induced vibration with nonlinear restoring forces. *Physics of Fluids*, 25(8). doi: 10.1063/1.4819082
- Mehmood, A., Abdelkefi, A., Hajj, M. R., Nayfeh, A. H., Akhtar, I., & Nuhait, A. O. (2013). Piezoelectric energy harvesting from vortex-induced vibrations of circular cylinder. *Journal of Sound and Vibration*, 332(19), 4656-4667.
- Nayfeh, A. H., & Mook, D. T. (1979). *Nonlinear oscillations*. New York: Wiley.
- Niell, N. G., & Elvin, A. A. (2009). The flutter response of a piezoelectrically damped cantilever pipe. *Journal of Intelligent Material Systems and Structures*, 20(16), 2017-2026. doi: 10.1177/1045389X09345557
- Pellegrini, S. P., Tolou, N., Schenk, M., & Herder, J. L. (2013). Bistable vibration energy harvesters: A review. *Journal of Intelligent Material Systems and Structures*, 24, 1303-1312. doi: 10.1177/1045389X12444940
- Robbins, W. P., Marusic, I., Morris, D., & Novak, T. O. (2006). Wind-generated electrical energy using flexible piezoelectric materials. *Proceedings of the ASME 2006 International Mechanical Engineering Congress and Exposition*. Retrieved from https://people.eng.unimelb.edu.au/imarusic/publications/Conferences/Robbins_Chicago_2006.pdf
- Shan, X., Song, R., Fan, M., & Xie, T. (2016). Energy-harvesting performances of two tandem piezoelectric energy harvesters with cylinders in water. *Applied Sciences*, 6(8). doi: 10.3390/app6080230
- Song, R., Shan, X., Lv, F., & Xie, T. (2015). A study of vortex-induced energy harvesting from water using PZT piezoelectric cantilever with cylindrical extension. *Ceramics International*, 41(supplement 1), S768-S773.
- Tang, L., Yang, Y., & Soh, C. K. (2009). Toward broadband vibration-based energy harvesting. *Journal of Intelligent Material Systems and Structures*, 21(18), 1867-1897. doi: 10.1177/1045389X10390249
- Taylor, G. W., Burns, J. R., Kammann, S. A., Powers, W. B., & Welsh, T. R. (2001). The energy harvesting eel: A small subsurface ocean/river power generator. *IEEE Journal of Oceanic Engineering*, 26(4), 539-547. doi: 10.1109/48.972090
- Yang, Y., Tang, L., & Li, H. (2009). Vibration energy harvesting using macro-fiber composites. *Smart Materials and Structures*, 18(11). doi: 10.1088/0964-1726/18/11/115025
- Zhou, W., Liao, W. H., & Li, W. J. (2005). Analysis design of a self-powered piezoelectric micro accelerometer. *Proceedings of the SPIE Smart Structures and Materials Conference*. doi: 10.1117/12.601131
- Zhu, Q. (2011). Optimal frequency for flow energy harvesting of a flapping foil. *Journal of Fluid Mechanics*, 675, 495-517.
- Zhu, Q., & Peng, Z. (2009). Mode coupling and flow energy harvesting by a flapping foil. *Physics of Fluids*, 21(3). doi: 10.1063/1.3092484
- Zhu, Q., Haase, M., & Wu, C. H. (2009). Modeling the capacity of a novel Dow-energy harvester. *Applied Mathematical Modelling*, 33, 2207-2217.

Biographies

AMEEN EL-SINAWI joined AUIS in the fall of 2019 as the chair of Engineering Department. Prior to his appointment at AUIS, he held faculty positions for a total of 19 years at Khalifa University, the American University of Sharjah, and King Fahd University of Petroleum and Minerals. He started his engineering career as a research and development engineer at the International Truck and Engine Corporation, USA. He has worked on numerous projects related to active control of machining processes, turbine blade modeling and control, unmanned aerial vehicles, fuel cells, remote sensing, magneto-rheological dampers, structural design and fatigue analysis, and impact dynamics. He has numerous publications and funded research projects in related fields. His research interests include structural damage detection, modeling and control of linear and nonlinear dynamic systems, system identification, MEMS modeling and control, and nondestructive testing. Dr. Sinawi earned his MS and PhD degrees in mechanical engineering from the University of Dayton in 1995 and 1999, respectively. Dr. Sinawi may be reached at Ameen.sinawi@auis.edu.krd

ISAM JANAJREH is a professor and associate chair in the Mechanical Engineering Department at Khalifa University Abu Dhabi. He received his MS and PhD degrees from Virginia Tech. in Engineering Science and Mechanics (ESM) and Mechanical Engineering (ME), specializing in fluid dynamics, thermochemical conversion, solid/fluid interactions, and turbulence modeling. Isam joined KU in

2007, spending one year at MIT as a visiting professor and conducting research on thermochemical conversion and assisting in advising students. He has authored over 100 refereed publications on energy conversion and has made as many contributions to international conferences. He was a key contributor on three Michelin and another three KU patents (Catamarans, Primacy, X-one, bioreactor), and three books (traction, rolling resistance, and noise). He was the organizer of the Arab Academy of Science conference series (2010-2013), a regular reviewer for several international journals (EC&M, Applied Pyrolysis, Renewable Energy, Fuel), chief editor (IJERSTE) and associate editor (IJTEE), and has been a member of ASME, TS&T, Rubber Division, ASCE, and several international scientific committees. Dr. Janajreh may be reached at Isam.janajreh@ku.ac.ac

EFFECT OF GEOMETRIC MODIFICATIONS ON SCRAMJET COMBUSTOR PERFORMANCE

Ayad Alhumadi, Old Dominion University; Alok K. Verma, Old Dominion University

Abstract

In this study, the effects of the backstep location, height, and angle on a supersonic hydrogen/air jet flame engine with a square cross-sectional area geometry were mathematically investigated. The mathematical model incorporated multi-species Navier–Stokes equations, the K-epsilon model, and the axisymmetric turbulence model. Shockwave effects were examined by changing the backstop location, height, and angle; special consideration was given to the combustion efficiency, thrust, pressure losses, and equivalence ratio of the scramjet combustor. The maximum thrust force and minimum pressure loss were observed when the first and second backsteps had heights of 0.5 and 0.25 cm, respectively, and were at 15 and 26 cm, respectively, from the air inlet.

Introduction

A scramjet engine is designed to operate at high speeds. The air entering the isolator makes the flow within the combustion chamber difficult to control. Therefore, understanding the supersonic mixing and the combustion process is required. Because of the high flow speed, the fuel must be mixed with air and be burned in a very short time. Therefore, two backsteps were used in this investigation to create shockwaves in order to decelerate the air to subsonic speed. This deceleration is required in order to increase the mixing efficiency and enable combustion. Kim, Huh, Yoon, Jeung, and Choi (1999) found that shockwaves greatly improve the mixing efficiency and combustion efficiency. Roga (2019) examined the scramjet combustor with diamond-shaped strut injectors at supersonic Mach 4.5 by using a CFD analysis. It was based on a species transport combustor, which is a standard k-epsilon turbulence model. He found the maximum temperature and pressure to be 3517K and 1.487 MPa, respectively, with a combustion efficiency of 87.2%, which was given by the diamond-shaped strut injector. Pandey, Roga, and Choubey (2016) used a scramjet engine at Mach 6 with parallel injection to study the inlet-combustor interaction and flow structure. Three different angles of attack ($\alpha=4^\circ$, $\alpha=0^\circ$, and $\alpha=4^\circ$) were used in their study for parallel injection. Their analysis showed that an angle of attack of $\alpha=0^\circ$ had good agreement qualitatively and quantitatively with experiments. At an angle of $\alpha=4^\circ$, the maximum temperature that occurred in the recirculation area was 2600k compared to angles of $\alpha=0^\circ$ and $\alpha=4^\circ$, and combustion efficiency was the highest (approximately 88%), when compared to $\alpha=0^\circ$ and $\alpha=4^\circ$. A shorter ignition delay was found to be at $\alpha=4^\circ$.

Da, Kim, and Kim (2015) studied the effect of fuel-air equivalence ratio on the flow field properties in a cavity-based mixing mechanism at a freestream Mach number of 2.08, and the performance of injector location on the fuel-air mixing. They observed that the flow field shock structure changed with a change in the fuel-air equivalence ratio, and the total pressure loss depended both on the fuel-air equivalence ratio and fuel type. Also, the spread of fuel in the test section showed a marked variation with the equivalence ratio. Jinda and Kumar (2019) investigated enhanced fuel-air mixing and combustion in supersonic combustors by using a new asymmetric strut-based fuel injection. Their investigation showed that, due to the presence of vortices inside the combustor, the air and fuel mixed properly, which significantly increased the mixing and combustion efficiency of the combustion. In this current study, the authors investigated the relationship between shockwave and pressure losses. An axisymmetric supersonic model combustor was used to compute the effect of shockwaves created by backsteps. A parametric study was performed to determine the effect of variations in the backstep height, location, and angle on the combustion efficiency, total pressure losses, thrust, and equivalence ratio.

Scramjet Geometry

Figure 1 presents a schematic of the geometry analyzed in this current study. This axisymmetric geometry was also used by Olynciw-Mills (2001) and Carson (2004), though those studies only incorporated one backstep in the combustor geometry. Carson used a backward-facing step with two heights (0.32 cm and 0.64 cm) in order to investigate the combustion efficiency by varying the equivalence ratio (Φ) from 1.13 to 1.44. His investigation showed that, for hydrogen, the optimum equivalence ratio was equal to 1.13 with a combustion efficiency of 67.5%. When the equivalence ratio was increased to 1.44, the combustion efficiency decreased. Alhumadi (2012) investigated two single backstep geometries (at locations 15 cm and 26 cm); the results showed that the values of thrust and equivalence ratio for a single backstep were inferior to the values obtained when two backsteps were used. This is an indication that the expansion of flow through two backsteps was more effective in reducing air velocity, which results in a better value of combustion efficiency than when a single backstep is used. The equivalence ratio for the single-backstep and no-backstep geometries was between 1.30 and 1.46, which indicated that there was excess fuel in the fuel oxidizer mixture.

The total length of the combustor configuration used in this present study was 67 cm. The air inlet had a square cross-sectional area of 3.4 cm × 3.4 cm and a fuel injector cross-sectional diameter of 0.2 cm. The fuel injector was located 29 cm from the air inlet. The outlet of the geometry also had a square cross-sectional area with a variable height, y , depending on the value of h_2 .

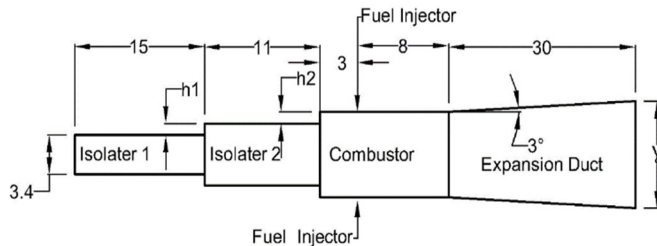


Figure 1. Scramjet geometry.

The geometry was divided into four parts:

- Isolators 1 and 2 (15 cm and 11 cm long, respectively)
- Combustion chamber (11 cm long)
- Fuel injector
- Diverging section (30 cm long)

Isolator 1 had a constant cross-sectional area with a height of 3.4 cm and length of 15 cm. Figure 1 show how the cross-sectional area of Isolator 2 changed, due to the fact that its inlet height had upper and lower backsteps represented by h_1 . Its length was 11 cm and its height was equal to $H_1 = (3.4 + 2h_1)$ cm. The value of h_1 was changed from 0.125 to 0.75 cm in order to investigate the pressure losses, combustion efficiency, thrust, and equivalence ratio as a function of backstep height. The outlet of Isolator 2 also had upper and lower backsteps with a height h_2 that varied from 0.125 to 0.75 cm. The height at the outlet of Isolator 2 was $H_2 = 3.4 + 2(h_1 + h_2)$ cm.

The function of the two isolators was to reduce the interaction with the surroundings and improve the homogeneity of the flow in the combustor (John, 1984). Figures 2 and 3 show that the function of the two backsteps was to create shock and recirculation regions downstream of the steps (Halupovich, Benveniste, & Rom, 1999). The recirculation region reduced the speed of air entering the combustion chamber as it encountered the hydrogen jet fuel that was injected normally to the flow, which resulted in an increase in the strength of the resulting shockwave, a decrease in the average air flow velocity, and an increase in the average pressure in the combustor. The mixing (air and fuel) efficiency increased at low air velocity, which created a mixture that burned instantly and produced highly energetic gas that expanded through the diverging section. The diverging section walls were at an angle of 3.0° to the free stream direction in order to prevent throttle choking (i.e., backfire).

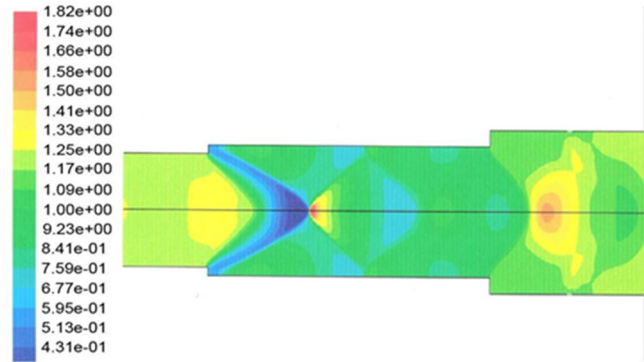


Figure 2. Static pressure contours.

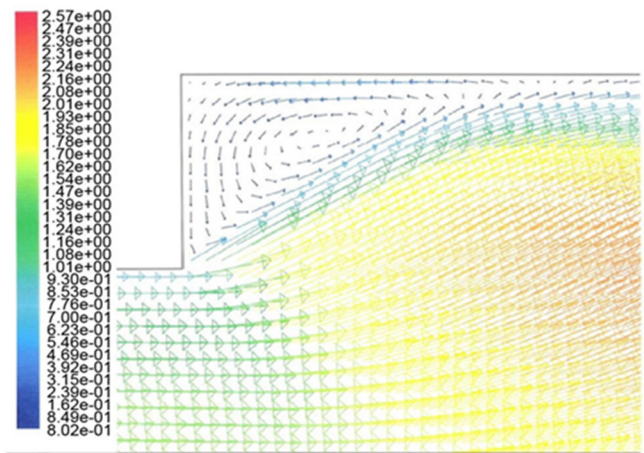


Figure 3. Vortices at the backstep.

Computational Method

Fluent, the computational fluid dynamics (CFD) code, was used to solve the present problem. A density-based solver was chosen for the general conservation equations for continuity, momentum, energy, and species. Those equations were discretized into a system of algebraic equations. These equations were then solved numerically to define the solution field within Fluent. Several iterations needed to be performed before a converged solution was obtained (70,000 iterations were typical). Two options existed for the density-based solver: implicit and explicit. The implicit solution approach is usually preferred to the explicit approach, which has a very strict limit on the time step size. The advantage of the implicit solver is that it performs much faster than the explicit solver and is unconditionally stable with respect to time step size. The solver uses the point implicit Gauss–Seidel/symmetric block (Gauss–Seidel/ILU) method to solve for variables. In order to calculate the specified turbulent flow, the $K-\epsilon$ model was used. This model has three user-defined options: standard, renormalization group (RNG), and realizable. The realizable option was chosen because it provides superior performance for flows involv-

ing rotation, boundary layers under strong adverse pressure gradients, separation, and recirculation.

The species model used finite-rate/eddy-dissipation, since it is suitable for turbulent flows (high Reynolds number), fast chemical reactions, and non-premixed air and fuel. Structured quadrilateral elements were used to create the grid. The independence of present solutions with respect to grid size was ensured by examining grid independence. Grids with 40,000–80,000 cells were examined. A grid with a mesh size of 70,000 cells was established as nominal. The Fluent computational algorithm used in this investigation was validated against the numerical and experimental results from Kim et al. (1999), who examined a scramjet combustor. The boundary conditions for the air entering the isolator were as follows: $P_t = 13.667$ atm, $P_s = 0.8$ atm, and $T_t = 1998$ K. In addition, fuel was injected at $P_t = 2.12$ atm, $P_s = 1.12$ atm, and $T_t = 294$ K.

Results and Discussion

The effects of h_1 , h_2 , L_1 , L_2 , θ_1 , and θ_2 on η_c , Π , T , and Φ were examined. Geometries with and without backsteps were compared in order to evaluate the benefits. Two backsteps were used to reduce the air velocity entering the combustion chamber and increase the mixing efficiency with the fuel for better combustion efficiency. Figure 4 shows how the sudden expansion of the flow in the first and second backsteps created shockwaves. This shock system reduced the speed of the flow. A major disadvantage of the shock system is pressure loss (Jagannath, Naresh, & Pandey, 2007). Shockwaves are distinguished by a sudden change in the characteristics of the medium, such as the pressure, temperature, or speed (Bird, 1967; Anderson, 1989). When air enters the pipe, a boundary layer is formed; this entrance region is considered to be a non-fully developed flow region, and the fluid accelerates or decelerates as it flows, according to the rate of growth of the boundary layer. The calculated Reynolds number indicated that the flow was turbulent (Bardina, Huang, & Coakley, 1997; Jones & Launder, 1972).

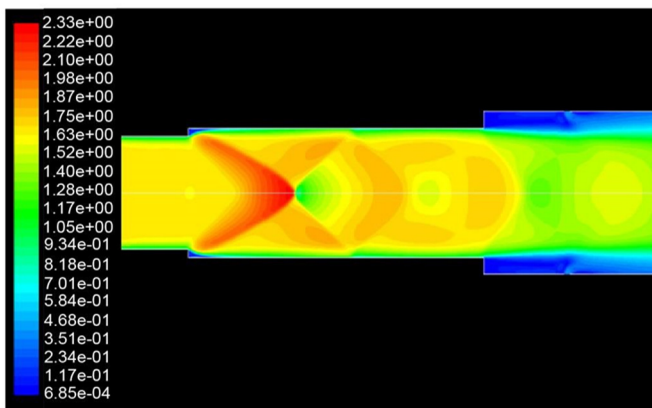


Figure 4. Mach number contours.

The purpose of this current study was to determine the appropriate backstep height, location, and angle in order to minimize pressure loss and maximize thrust. Figure 5 shows the first case that was considered: geometry with no backstep. The hydrogen was injected normal to the air flowing at high speed. The reaction of air with hydrogen in a geometry with no backsteps resulted in a combustion efficiency of 64.6%, thrust of 221.5 N, pressure loss of 0.37 atm, and an equivalence ratio of 1.455.

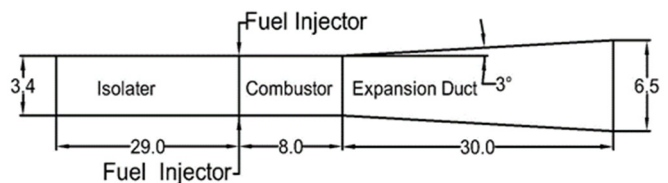


Figure 5. Scramjet geometry with no backstep.

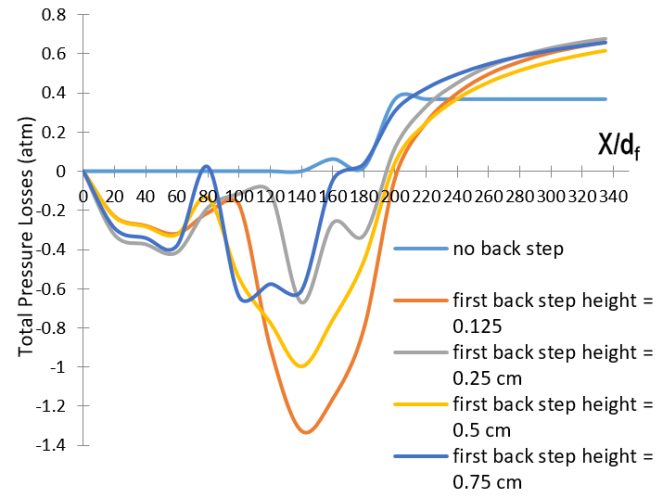
These results were compared with a geometry having two backsteps and with a geometry having one backstep height h of 0.5 cm. The following properties were kept constant:

- Fuel injector diameter: 0.2 cm
- Number of fuel injectors: 2
- Fuel injector: 29 cm from the air inlet
- Location of the first backstep: 15 cm from the air inlet
- Location of the second backstep: 26 cm from the air inlet
- Air inlet dimensions: 3.4 cm \times 3.4 cm Exhaust outlet dimensions: y cm \times y cm
- Geometry: axisymmetric.

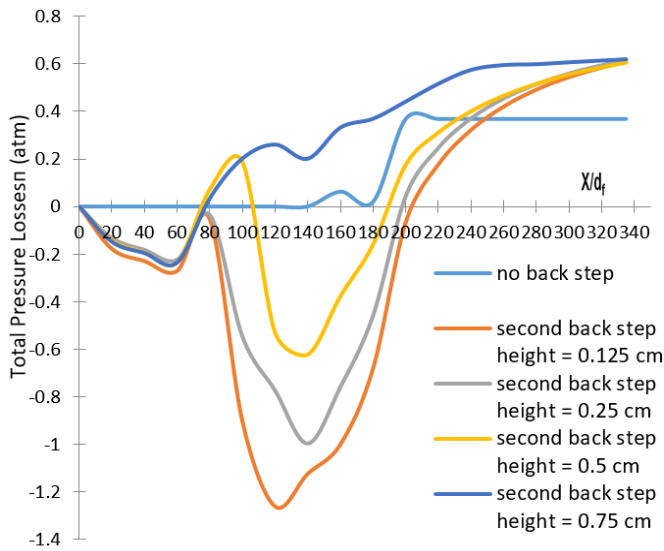
Effect of the Backstep Height on Performance Parameters

To determine the effect of h_1 on η_c , Π , T , and Φ , h_2 was kept constant at 0.25 cm, while h_1 was varied between 0.125 and 0.75 cm. During the steady-state adiabatic process for the supersonic flow in the 15 cm long duct with a constant area, viscous effects caused the flow properties to change along the duct (John, 1984). When the high-temperature air reached the first set of backsteps, expansion waves formed as a result of the sudden deceleration of the air at the backsteps. Between the first and second set of backsteps, a series of expansion waves and shockwaves formed. Figure 6(a) shows how the vortices between the two backsteps caused viscous energy losses and changes in the velocity, density, and pressure. When the air reached the fuel injectors and mixed with the fuel, ignition occurred. The Mach number of the high-temperature mixture increased and the gas further expanded through the diverging channel.

Combustion efficiency is a measure of the useful heat extracted from a fuel when it reacts with an oxidizer, as given by Equation 1:



(a) Effect of h_1 on Π



(b) Effect of h_2 on Π

Figure 6. Effect of h on Π .

$$\text{Combustion efficiency} = \frac{\text{mass of fuel in} - \text{mass of fuel out}}{\text{mass of fuel in}} \quad (1)$$

Figure 7(a) shows an increase in the combustion efficiency for the geometry with two backsteps compared with the geometry with no backstep. Shockwaves created by the first backstep with a height of 0.5 cm increased the local temperature and decreased the flow velocity, which increased the combustion efficiency and thrust. Table 1 presents the per-

centage increase in the combustion efficiency and thrust compared with the geometry with no backstep. Table 2 presents the effect of h_1 on T and Φ .

Table 1. Percent increase in η_c and T .

h_1 (cm)	% Increase in η_c	% Increase in T (N)
0.125	19	20
0.25	21	26
0.50	29	70
0.75	14	26

Table 2. T and Φ for various h_1 .

h_1 (cm)	T (N)	Φ
0.125	267	1.37
0.25	278	1.31
0.50	376	0.98
0.75	279	1.19
No backstep	221	1.46

The equivalence ratio is defined as the actual fuel-to-oxidizer ratio divided by the stoichiometric fuel-to-oxidizer ratio. The case with no backstep showed $\Phi > 1$, which indicated excess fuel in the fuel-oxidizer mixture, while the case with the first backstep at a height of 0.5 cm showed an equivalence ratio very close to 1. An equivalence ratio of < 1 indicates a deficiency in the level of fuel (i.e., excess oxidizer) in the mixture. Therefore, setting the first backstep height at 0.5 cm resulted in a more efficient combustion process compared to other heights for the first backstep. Then, h_1 was kept constant at 0.5 cm and h_2 was changed between 0.125 cm and 0.75 cm in order to determine the effect on η_c , Π , T , and Φ . Figures 6(b), 7(b), and Table 3 show the results of these tests. Figure 6(b) also shows that changing h_2 had no major effect on Π , because of the close proximity of this step to the fuel injector. Table 4 presents the percentage increase in η_c and T compared to a geometry with no backstep. Tables 1 and 4 indicate that the most efficient values for h_1 and h_2 were 0.5 and 0.25 cm, respectively. Tables 2 and 3 indicate that the maximum T was reached when Φ was close to one (0.98 and 0.92). When Figures 6 (a) and 6(b) are compared, the values of Π for changes to h_2 were less than those associated with changes to h_1 .

Effect of the Backstep Location on Performance Parameters

In order to investigate the effect of L_1 and L_2 (i.e., distances of the backsteps from the air inlet) on η_c , Π , T , and Φ , L_2 was held constant at 26 cm, while L_1 was varied between 12 and 21 cm. Based on the results of the parametric

study on the step height, two backstep heights were chosen and kept constant: $h_1 = 0.5$ cm and $h_2 = 0.25$ cm. Figures 8 (a) and 9(a) show the effect of varying L_1 on η_c and Π . Table 5 indicates that T and η_c were optimized (with a minimum Π) when $L_1 = 15$ cm. As L_1 moved towards L_2 , η_c and T decreased, while Π and Φ increased.

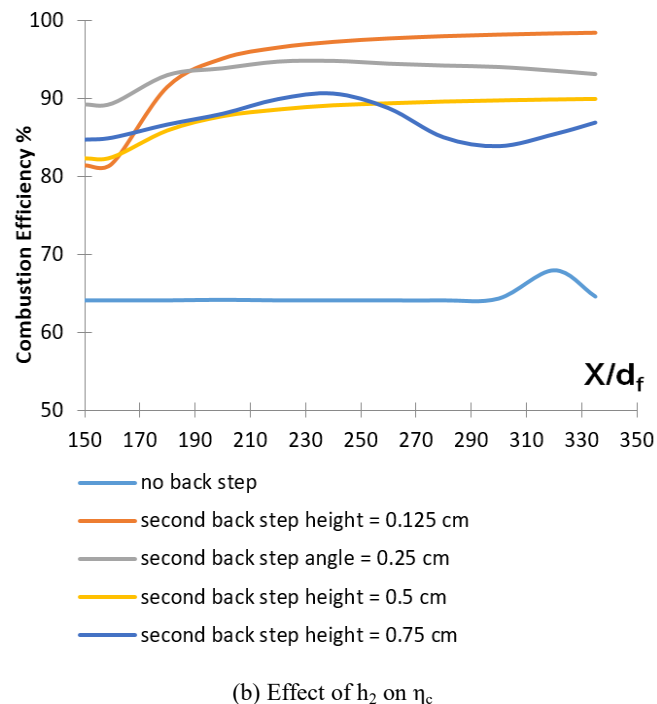
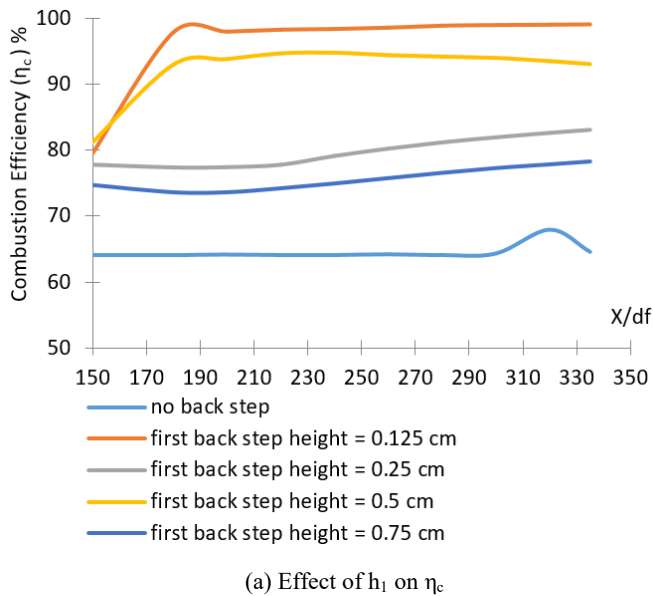


Figure 7. Effect of h on η_c .

This degradation in performance was due to the shock-waves becoming less effective at reducing the flow speed of the air approaching the fuel injector. When the air velocity was high, the mixing efficiency was poor, which decreased η_c . When the reduction in the air flow speed upstream of the fuel injector was examined, $L_1 = 15$ cm was determined to be the most effective location.

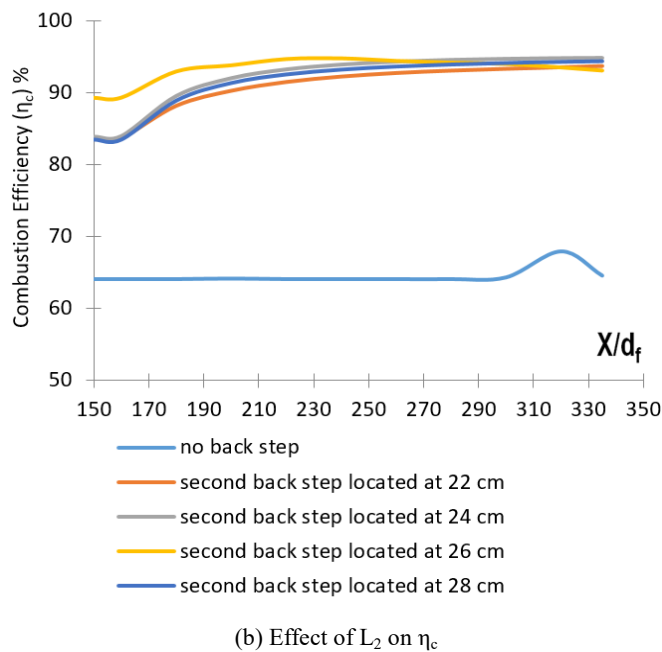
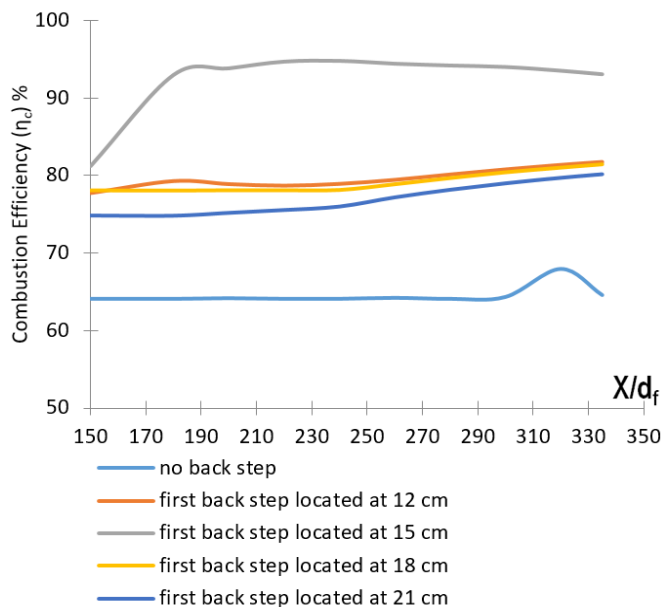


Figure 8. Effect of L on η_c .

Table 3. T and Φ for various h_2 .

h_2 (cm)	T (N)	Φ
0.125	252	1.24
0.25	376	0.98
0.50	375	0.92
0.75	288	1.19
No Backstep	221	1.46

Table 4. Percent increase in η_c and T.

h_2 (cm)	% Increase in η_c	% Increase in T (N)
0.125	19	14
0.25	29	70
0.50	25	70
0.75	22	30

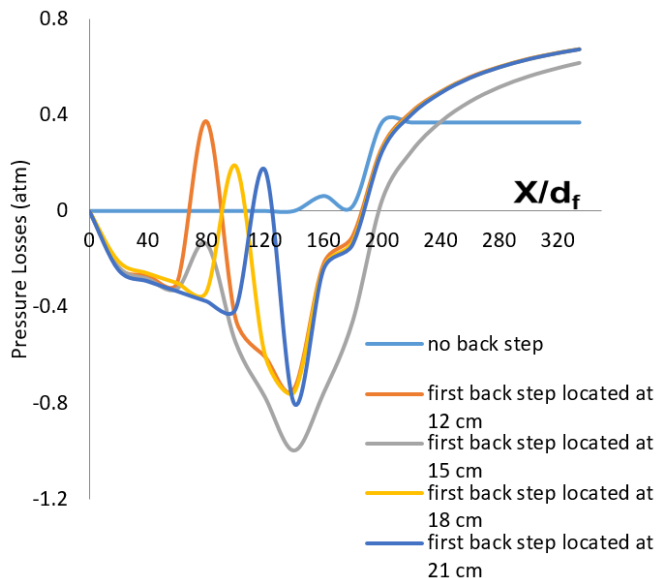
Table 5. η_c , Π , T, and Φ for various values of L_1 .

L_1 (cm)	% η_c	Π (atm)	T (N)	Φ
12	82	0.67	274	1.28
15	93	0.62	376	0.98
18	82	0.67	277	1.26
21	80	0.68	276	1.28
No backstep	65	0.37	221	1.46
Single backstep 15 cm	84	0.69	261	1.31
Single backstep 26 cm	85	0.70	272	1.30

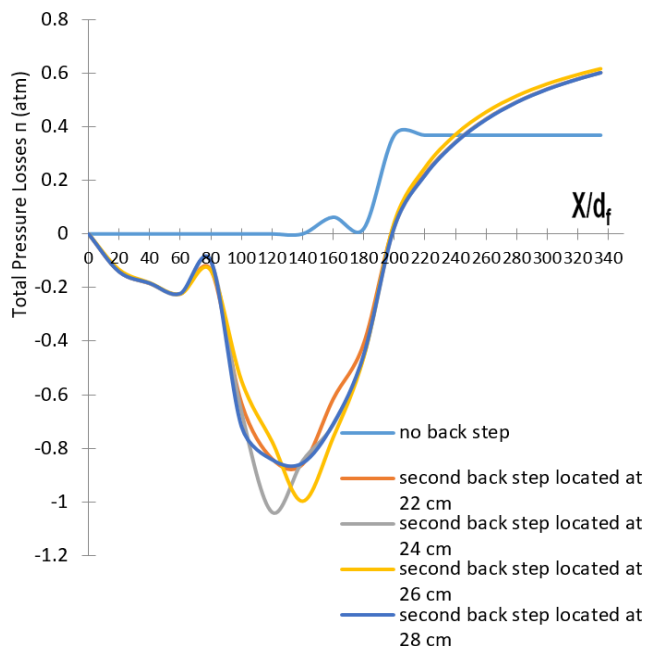
To examine the effectiveness of the geometry with two backsteps, two geometries with single backsteps (at 15 and 26 cm from the air inlet) were investigated. Table 5 lists these results. The thrust and equivalence ratios were not as good with a single backstep as when two backsteps were used. This indicated that the two expansions of the flow with the two backsteps were more effective at reducing the air velocity, which resulted in a better combustion efficiency than when a single backstep was used. The equivalence ratios for the geometries with no backstep and a single backstep were between 1.30 and 1.46, which indicated excess fuel in the fuel-oxidizer mixture. Therefore, more air was needed to complete the combustion, which led to better thrust.

In order to investigate the effect of L_2 on the performance parameters, the most effective value of L_1 (15 cm) was kept constant, while L_2 was varied between 22 and 28 cm. Figures 8(b) and 9(b) show no major effect on Π and η_c when L_2 was varied. This may be due to the close proximity of L_2 to the fuel injector. Table 6 indicates that T was optimized

when L_2 was at 26 cm from the air inlet. As L_2 was moved toward L_1 , T decreased while Φ increased. This degradation in performance was due to the ineffectiveness of the shock-wave/expansion wave system at reducing the flow speed of the air approaching the fuel injector. The high air velocity led to poor fluid mixing and low combustion efficiency. Therefore, the most effective locations for L_1 and L_2 were found to be 15 and 26 cm, respectively.



(a) Effect of L_1 on Π



(b) Effect of L_2 on Π

Figure 9. Effect of L on Π .

Table 6. T and Φ for various values of L_2 .

L_2 (cm)	T (N)	Φ
22	329	1.1
24	349	1.02
26	376	0.98
28	341	1.02
No backstep	221	1.6

Effect of the Backstep angle on Performance Parameters

The effect of varying θ_1 and θ_2 on the performance parameters (i.e., combustion efficiency, pressure loss, thrust, and equivalence ratio) was evaluated. In order to perform a parametric study on θ_1 , θ_2 was kept constant at 90° , while θ_1 was varied between 25° and 90° . Based on the results of the previous parametric study, the most effective values of the following variables were chosen and kept constant: $h_1 = 0.5$ cm, $h_2 = 0.25$ cm, $L_1 = 15$ cm, and $L_2 = 26$ cm. The pressure contours in Figures 10(a-b) show that increasing θ_1 caused the recirculation region immediately downstream of the backstep to increase. In addition, Table 7 shows that the strength of the shockwaves at the first backstep increased, which decreased the flow velocity between the air inlet and first backstep. Figure 11(a) shows how this increased the combustion efficiency, which reached its maximum at $\theta_1 = 90^\circ$.

Table 7. Percent decrease in velocity from the air inlet to the first backstep for various values of θ_1 .

θ_1	$\Delta V/V_i$
25	5.0
45	5.9
65	17.5
90	19.0

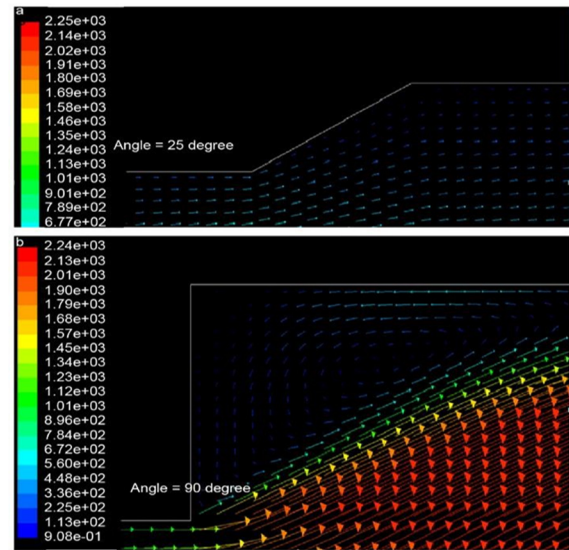


Figure 10. (a-b) As the backstep angles increase, the vortices behind the backstep increase. This reduces the air velocity.

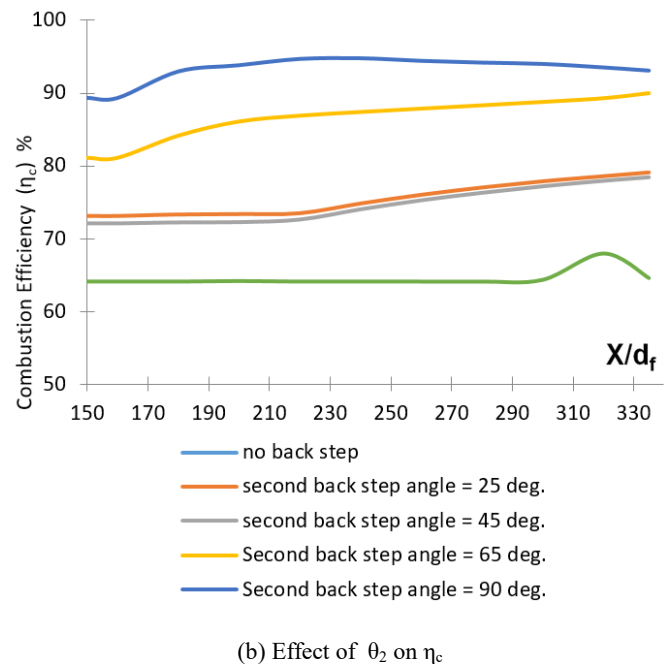
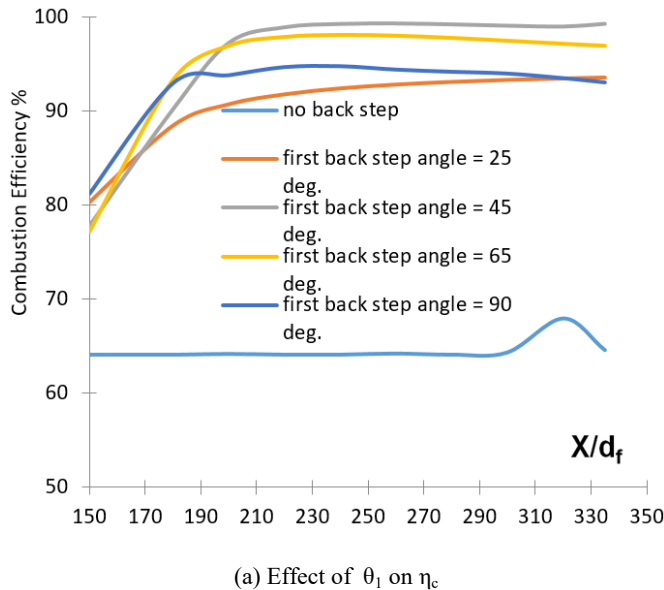
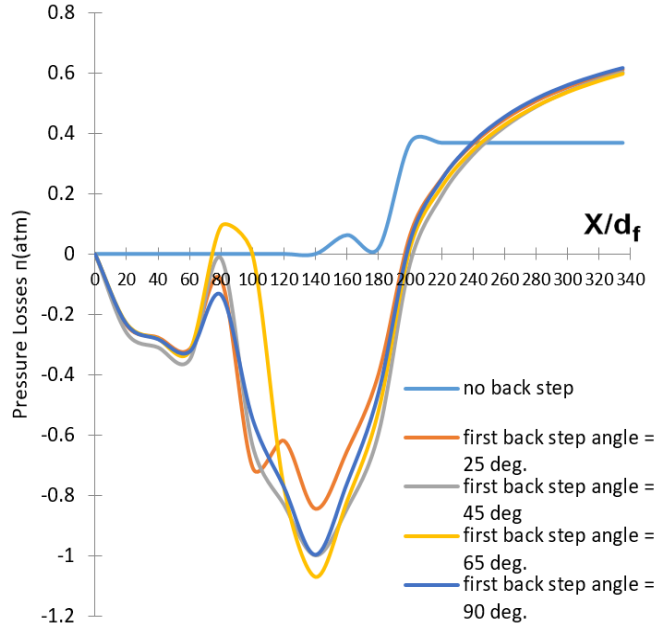
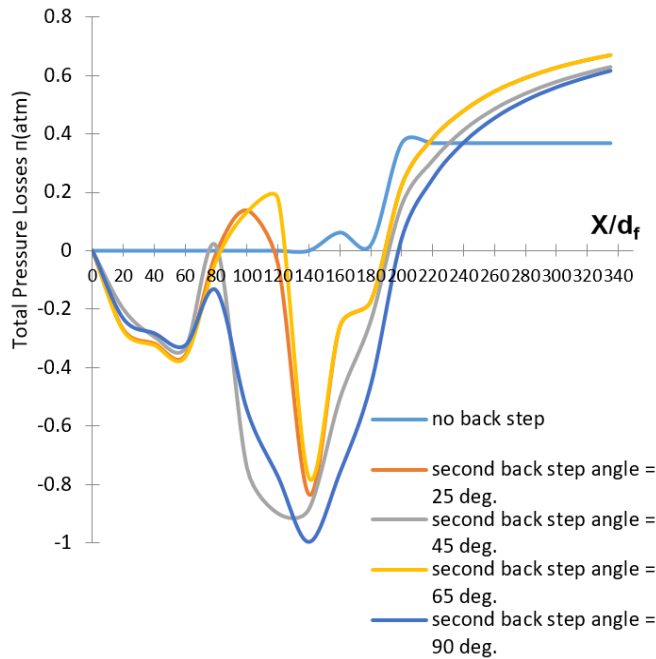


Figure 11. Effect of θ on η_c .

Figure 12(a) indicates a significant variation in pressure loss in the vicinity of the first backstep ($X/d_f = 80$) as a function of θ_1 . However, as the combustor exit was approached, the profiles converged. Table 8 presents the performance parameters as a function of θ_1 .



(a) Effect of θ_1 on Π



(b) Effect of θ_2 on Π

Figure 12. Effect of θ on Π .

Table 8. η_c , Π , T, and Φ for various values of θ_1 .

θ_1 ($^\circ$)	% η_c	Π (atm)	T (N)	Φ
25	94	0.61	342	1.20
45	93	0.60	342	1.14
65	97	0.60	351	1.04
90	99	0.61	377	0.98
No backstep	65	0.37	221	1.46

As θ_1 increased to 90° , the highest engine thrust (with a reasonable Φ) was obtained. Table 9 indicates that the shock system created at $\theta_1 = 90^\circ$ was more effective at reducing the air velocity and increasing the reaction rate, and presents the difference between the maximum and minimum rates of reaction as a function of θ_1 . To examine the effect of varying θ_2 on the performance parameters, θ_1 was held constant at its most effective value of 90° , while θ_2 was varied between 25° and 90° . The pressure contours for various values of θ_2 indicated that increasing θ_2 increased the recirculation zone downstream of the second backstep. This is the same as the previous results for a variable θ_1 . Figure 11 (b) shows the variation in η_c with X/d_f for various values of θ_2 ; η_c increased with θ_2 , due to enhanced fuel-air mixing. Figure 12(b) shows that, when $\theta_2 = 90^\circ$, the pressure losses were minimized, as well as the variation in Π with X/d_f for different values of θ_2 .

Table 9. Difference between maximum and minimum rates of reaction for various values of θ_1 .

θ_1 ($^\circ$)	Rate of reaction ($\text{kg mol/m}^3 \text{ S}$)
25	242
45	433
65	527
90	593
No backstep	134

The shockwave system created by the two backsteps helped enhance the combustion of the mixed reactants by increasing the local temperature and decreasing the local air flow velocity from the air inlet to the second backstep by 52.6%, which resulted in a longer residence time. This is consistent with the experience of Kim et al. (1999). Table 10 presents the performance parameters as a function of θ_2 and indicates that the maximum thrust, where Φ was almost one, was obtained at $\theta_2 = 90^\circ$. Tables 1–10 indicate that the thrust generally decreased with increasing Φ ; therefore, Φ is generally inversely proportional to thrust. The maximum thrust was obtained when Φ was close to one. Table 11 shows that the pressure contours for the different geometric modifications were indicative of the fact that adding the second backstep to the present combustor configuration significantly increased the effectiveness. This is verified by

the data in Table 5, demonstrating the benefit of a pair of backsteps over a single backstep.

Table 10. η_c , Π , T, and Φ for various values of θ_2 .

θ_2 (°)	% η_c	Π (atm)	T (N)	Φ
25	79	0.67	287	1.23
45	78	0.67	293	1.22
65	90	0.63	362	0.91
90	93	0.62	376	0.98
No backstep	65	0.37	221	1.46

Table 11. Percent increase in η_c and T for one and two backsteps compared with no backstep.

Number of backsteps	Location (cm)	% Increase in η_c	% Increase in T
One	15	23	15
One	26	24	19
Two	15–26	30	70

Conclusions

The effects of two backsteps were investigated numerically and compared with geometries having no backstep and a single backstep. The locations, heights, and angles of the backsteps were examined for their effects on the combustion efficiency, pressure losses, thrust, and equivalence ratio of a supersonic non-premixed hydrogen–air jet flame in a model scramjet combustor. The main conclusions are as follows.

1. The geometry with no backstep showed the lowest combustion efficiency and thrust, while the geometries with single backsteps showed better results when the backsteps were located 15 and 26 cm, respectively, from the air inlet. The thrust increased by 15% and 19%, respectively, and the combustion efficiency increased by 23% and 24%, respectively.
2. The geometry with two backsteps showed major improvement compared to the geometry with no backstep. The thrust increased by 41%, and the combustion efficiency increased by 30.0% with an equivalence ratio close to one.
3. An angle of 90° for the first and second backsteps produced a more efficient recirculation zone and was better at reducing the flow velocity compared to the other backstep angles of 65°, 45°, and 25° with minimum pressure losses. This caused intense mixing and increased combustion efficiency.
4. Shockwaves caused by changing the second backstep height and location had little effect on the pressure losses when compared with changing the second

backstep angle. This is because the backstep was near the fuel injector and the shockwave strength and recirculation zone efficiency varied with the angle. The results showed that optimizing the locations, heights, and angles of the first and second backsteps can increase combustion efficiency and thrust.

References

- Anderson, J. D. (1989). *Hypersonic and High Temperature Gas Dynamics*, McGraw Hill, New York, NY. ISBN: 1-56347-780-7/978-1-56347-780-5
- Alhumadi, A. (2012). *Numerical Study of the Performance of a Model Scramjet Engine* (Doctoral dissertation). Retrieved from https://digitalcommons.odu.edu/mae_etds/98
- Bardina, J. E., Huang, P. G., & Coakley, T. J. (1997). *Turbulence Modeling Validation, Testing and Development*. NASA Technical Memorandum 110446.
- Bird, G. A. (1967). The Velocity Distribution Function within a Shockwave. *Journal of Fluid Mechanics*, 30(3), 479-487. DOI: 10.1017/S0022112067001557
- Carson, R. A. (2004). *Numerical Study of Combustion of Hydrogen and Ethylene in a Two-dimensional Dual-mode Scramjet Combustor* (Unpublished master's thesis). Old Dominion University, Norfolk, VA.
- Halupovich, Y., Benveniste, N., & Rom, J. (1999). Numerical Solution of the Turbulent Supersonic Flow over a Backward Facing Step. *Fluid Dynamics Research*, 24(5), 251-273. DOI: 10.1016/S0169-5983(98)00025-2
- Jagannath, R., Naresh, N. G., & Pandey, K. M. (2007). Studies on Pressure Loss in Sudden Expansion in Flow through Nozzles: A Fuzzy Logic Approach. *ARPN Journal of Engineering and Applied Sciences*, 2(2), 50-61.
- John, J. E. A. (1984). *Gas Dynamics*. Allyn and Bacon, Boston, MA. ISBN: 0205080146/9780205080144
- Jones, W. P., & Launder, B. E. (1972). The Prediction of Laminarization with a Two Equation Model of Turbulence. *International Journal of Heat and Mass Transfer*, 15(2), 301-314. DOI: 10.1016/0017-9310(72)90076-2
- Kim, J.-H., Huh, H., Yoon, Y., Jeung, I. -S., & Choi, J. -Y. (1999). *Effects of Shockwaves on a Supersonic Hydrogen Air Jet Flame in a Model Scramjet Combustor*. The Second Asia-Pacific Conference on Combustion, Tainan, Taiwan, pp. 587-590.
- Pandey, K. M., Roga, S., & Choubey, G. (2016). Numerical investigation on hydrogen-fueled scramjet combustor with parallel strut fuel injector at a flight Mach number of 6. *Journal of Applied Fluid Mechanics*, 9(3), 1215-1220.
- Roga, S. (2019, August). CFD Analysis of Scramjet Engine Combustion Chamber with Diamond-Shaped Strut Injector at Flight Mach 4.5. *Journal of Physics: Conference Series*, 1276(1), 012041. IOP Publishing.
- Olynciw-Mills, M. (2001). *Investigation of Dual-Mode Combustion with Large Upstream Interaction*

(Unpublished master's thesis). Old Dominion University, Norfolk, VA.

Das, R., Kim, J. S., & Kim, H. D. (2015). Supersonic cavity-based combustion with kerosene/hydrogen fuel. *Journal of Thermal Science*, 24(2), 164-172.

Jinda, S., & Kumar, S. (2019). *CFD Modelling of Scramjet Combustor*. Seventh International Conference on Theoretical, Applied Computational and Experimental Mechanics, At: Aerospace Department, IIT Kharagpur

η_c combustion efficiency = $m_{f1} - m_{f2} / m_{f1}$
 Equivalence Ratio = $\Phi = (\text{fuel/air})_{\text{actual}} / (\text{fuel/air})$

θ_1 first backstep angle ($^\circ$)
 θ_2 second backstep angle ($^\circ$)
 Π static pressure = $P_1 - P_2$
 y exhaust outlet height (cm)

Biographies

AYAD ALHUMADI earned his master's degree in mechanical engineering from Buffalo State University (majoring in thermal science and minoring in math) and PhD from Old Dominion University (majoring in thermal science and minoring in aerospace). Dr. Alhumadi works at Old Dominion University in the Mechanical Engineering Technology Department. Before teaching, he worked for a number of companies as a process engineer and design engineer. Dr. Alhumadi may be reached at ahuma001@odu.edu

ALOK K. VERMA is Ray Ferrari Professor in the Engineering Technology Department at Old Dominion University. Dr. Verma received his BS in Aeronautical Engineering from IIT Kanpur, MS in Engineering Mechanics and PhD in Mechanical Engineering from ODU. Professor Verma is a licensed professional engineer in the state of Virginia, a certified manufacturing engineer, and has certifications in Lean Manufacturing and Six Sigma. Dr. Verma may be reached at averma@odu.edu

Nomenclature

A_1 inlet area
 A_2 outlet area
 h_1 first backstep height
 h_2 second backstep height
 H_1 total height of inlet isolator 2
 H_2 total height of outlet isolator 2
 L_1 first backstep location
 L_2 second backstep location
 \dot{m} mass flow rate
 m_a mass of air
 m_f mass of fuel
 m_{f1} mass of fuel at the inlet
 m_{f2} mass of fuel at the outlet
 P_1 inlet pressure
 P_2 outlet pressure
 P_s static pressure
 P_t total pressure
 RNG renormalization group
 T thrust $\equiv (P_2 A_2 - P_1 A_1) + \dot{m} (V_2 - V_1)$
 T_t total temperature
 V_1 inlet velocity
 V_2 outlet velocity
 ϵ epsilon

AN ANALYSIS OF BONE AND WOOD CHARCOAL COLOR CASE-HARDENED STEEL SAMPLES

Alex Johnson, Millersville University of Pennsylvania; Blaise Mibeck, Energy and Environmental Research Center;
Chris Beddoe, Energy and Environmental Research Center; Ravindra Thamma, Central Connecticut State University

Abstract

Color case hardening (CCH) using the bone and charcoal pack process is a carburizing method that has a long history. Though similar to many modern carburizing processes that yield better results (in terms of carbon consistency, case depth, and hardness) the CCH process has maintained popularity in the firearms industry, where it has historically been used as a treatment for firearm components. The CCH process, much like conventional case-hardening methods, yields a high carbon, file-hard shell that surrounds a softer, lower-carbon inner core. Unlike conventional case-hardening methods, the CCH process produces a surface that often displays a range of decorative colors. Preliminary examination of these surfaces shows that the process can produce, under some conditions, highly structured iron oxide nanoparticles that may prove useful in a variety of industries.

Introduction

Carburizing, the technology of infusing the surface of low-carbon steel with high concentrations of carbon to permit hardening is an ancient process that goes back at least to the days of the Roman Empire. A recent study involving metallurgical samples of five pieces of Roman armor, dated to about AD 120, indicated a high concentration of carbon on the hardened steel surface of the iron armor (Fulford, Sim, Doig, & Painter, 2005). Case-hardened surfaces exhibit several desirable tendencies, such as a hard, high-carbon shell surrounding a softer, low-carbon core that supports the hardened surface (Johnson & Weeks, 1977). While the ancient process of carburizing continues into modern times, there is a similar process referred to as color case hardening that, while still in use, has been limited to a much narrower sector. Color case hardening (CCH) is a carburizing process that results in the usual surface-hardening characteristic, but additionally a CCH surface exhibits a mottled color appearance (see Figure 1). Author Oscar Gaddy (1997), described these colors as a “range from straw color to brown, dark blue, light blue, white and shades of red, and are closely related to, but not identical to, temper colors that one obtains by heating polished steel in air to temperatures of 400 to 600°F.” Gaddy’s research interest was in recreating the colors that often appeared on fine sporting arms from the 19th and 20th centuries. Indeed, the firearms industry has been the primary user of the color case-hardening process, and it continues today within a limited sector of the firearms industry.



Figure 1. Color case-hardened sample pieces.

Though many authors, primarily of gunsmithing texts, have written about the process over the years (Howe, 1941; MacFarland, 1966; Vickery, 1955), few have fully described the procedure to achieve the distinctive, mottled color surface characterized by the bone and wood charcoal color case-hardening process. Part of the reason for this could simply be the authors themselves were describing the process second hand, without first-hand knowledge (Kelly, 2010). It is also possible that many of the authors felt that the color case-hardening process (when used with firearm-related parts) was potentially dangerous when done by those un-experienced with the concepts of heat treatment in firearm-related applications. Indeed, many authors of these texts cautioned against the use of the process, stating that it was an uncertain process that could result in damage to the firearm and injury to the user if not done correctly (Kelly, 2010). The other reason that the process may not have been described accurately was to protect trade secrets. When the Colt Manufacturing Company phased out their single-action army revolver in the 1930s and attempted to bring it back in the 1950s, they experienced considerable difficulty when they attempted to recreate the color case hardening that they had used in their pre-war revolvers. The period that had passed since they had last performed this operation had seen many employees familiar with the process retire or pass away, taking with them the knowledge of the process (Gaddy, 1997).

Kevin Kelly (2010) in his book, *What Technology Wants*, coins the term “Technium,” which, as he states, is “a word to designate the greater, global, massively interconnected system of technology vibrating around us.” The connection

that humans have shared with technology throughout history has shown that the advancement of technologies is not always uniform. Some technologies advance quickly, while others lag behind, often to be lost to the past. Though in many instances the rise and fall of technology runs parallel to human needs but, in other instances, technologies are deliberately held back or their use is marginalized. In many ways, this explains the color case-hardening process, which has never completely gone out of use from the time that it was first used; however, its use has largely been confined to the firearms sector and, for whatever reason, little academic research has been done. Yet, CCH is a process that is worthy of research. Color case-hardened surfaces exhibit some striking differences from the surfaces of parts produced with other carburizing operations.

The surface of a CCH part produced by the wood and bone charcoal process often exhibits highly complex crystalline structured surfaces that could prove useful in many fields (Pilotek & Tabellion, 2005). The surface structure of the color case-hardened surface consists of heavy concentrations of iron oxide, which, preliminary research shows, can be manipulated to present different sizes of nanoparticles. The potential to control the surface structure and size of the iron oxide shows the potential for use in a variety of applications. One area that shows promise is as a coating for use in the oil and gas industry in regards to steel pipe coatings. The process of manipulating nanoparticles is an area of interest to researchers today (Mirza, Rasu, & Desilva, 2016), but the process of using color case hardening as a means of forming these nanoparticles does not appear to have been explored.

Carburizing in Modern Industry

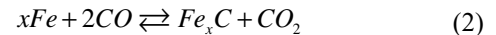
Carburizing is a method in which carbon is infused into the surface of low-carbon steel, providing the ability for the part to be heat treated using the same processes as high-carbon tool steels. Pack carburizing, one of the oldest methods known, involves placing the low-carbon steel parts in a carburizing container filled with a carburizing mixture. The container is sealed and then heated to temperatures suitable for the work that is being done, though 898-954°C seems to be quite common in industry (Grossman, 1937). As the container is heated, the carbon material in the container creates carbon monoxide and carbon dioxide gasses that infuse into the surface of the steel once the austenite transformation phase has been achieved. Carbon penetration is faster at higher temperatures, and carbon depth is largely a product of time in which the parts are exposed to the carbon-rich atmosphere. The length of time that the parts are heated and the temperature used are useful parameters in estimating the depth of carbon penetration in the parts.

Many different carbon-containing mixtures have been used as carburizing agents, but the common form is charcoal. Carbon alone is not all that efficient in producing carbon monoxide and, in order to facilitate this process, an

energizer is added to the pack. The energizer can be an inorganic such as carbonate, or an oxide or cyanide (Gaddy, 1997). The gasses are produced in the form of a simple reaction with the oxygen and carbon in the box, as by Equation 1:



The CO reacts with the steel during the austenitic phase, according the reaction described by Equation 2:



The Fe_3C forms on the surface of the steel during the austenitic phase (Grossman, 1937). As this reaction occurs, a surface layer of high-carbon steel is quickly built up. Due to the low-carbon content in the core, carbon atoms will attempt to reach equilibrium with the result that they will diffuse further into the surface during the austenite phase. How fast this diffusion occurs is to a degree dependent on temperature and the diffusion coefficient of the material (Woodworth, 1997). Though these processes share similarities with the methods used for color case hardening, there are some differences in the procedures that are used. In industry, pack carburizing is typically done at much higher temperatures than what is conventionally used for the CCH process. For instance, Grossman stated that the 898-954°C range is the norm (Grossman, 1937). Experiments with the CCH process have shown that temperatures much higher than 815°C result in little color patterns visible on the parts. At the lower temperature range used with the CCH process, though, surfaces tend to absorb greater concentrations of carbon, while the carbon penetration is considerably less than with more conventional methods (Gaddy, 1997).

The other main difference between the two processes is that in most industrial applications the parts that are being carburized are generally allowed to cool to room temperature after the carburizing cycle, removed, and heated again before being quenched (Johnson & Weeks, 1977). Though this process does provide some advantages, such as better retention of the carburizing mixture, parts case hardened in this manner do not exhibit the complex surface structure that the CCH process produces. The CCH process differs from the aforementioned approach in that the parts are immediately quenched directly from the crucible, taking care to eliminate outside contact with the air, which would immediately scale the surface. This results in the carburizing mixture going into the quench with the parts.

Experimental Details

Figure 2 shows six samples that were prepared using 1018 cold-rolled mild steel, 0.125-in² x 2 in-long stock, for testing. All samples were annealed and then surface ground using a 120-grit wheel to ensure consistency. The six samples were heat treated using different carburizing mixtures; some of the samples were only carburized and not hardened. All samples were carburized using mild-steel carburizing

vessels and carriers to avoid any potential for cross contamination. Distilled water, temperature controlled to 20°C was used in 18-liter containers for the samples that were hardened. Between tests, the water was discarded and the container thoroughly cleaned before the next test cycle.

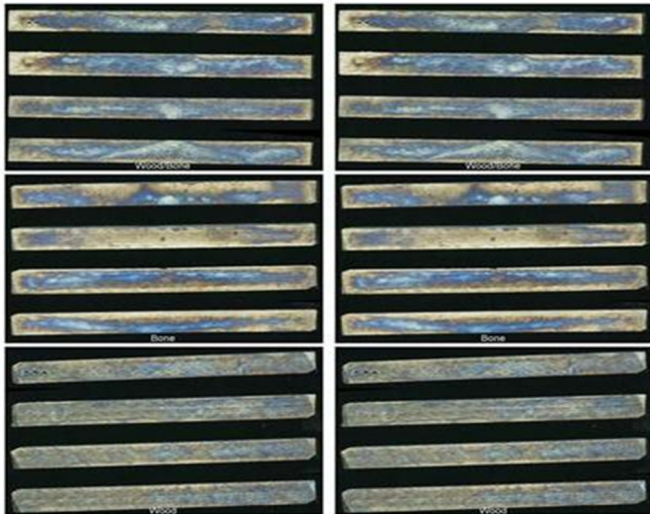


Figure 2. Color case-hardened samples.

A Johnson Gas heat treatment furnace controlled with a Honeywell UDC Digital Control was used for the heat treatment cycles. All samples were allowed to stabilize in the furnace at 801°C and soaked at that temperature for 1 ½ hours prior to either being removed or quenched. Wood and bone charcoal used in this study was obtained from Brownells, Inc. (2015). The bone charcoal was listed as 10 x 28 sieve size and the wood charcoal was number six mesh size. Prior to packing, all parts were cleaned with denatured alcohol to remove any residual oils that, experience has shown, will disrupt the CCH process (Kelly, 2010). Following the heat treatment operations, the six samples were mounted in epoxy and cross-sectioned. The face of each sample mount was successively ground and then polished to 4000 grit. Samples were not gold or carbon coated; instead, they were prepared with copper tape. Silver paint was applied to ensure good electrical conduction from the sample to ground. All observations were made with a JEOL 5800 scanning electron microscope with an Oxford Inca EDS system. Hardness tests were performed with a Micro Vickers Hardness Tester.

Color Case-Hardening Procedure

Unlike conventional carburizing operations, where the parts are generally carburized and allowed to cool, followed by a separate heating cycle to achieve critical temperatures and then quenched, CCH requires that the parts be removed immediately from the carburizing materials into the quench tank. For the parts to exhibit the characteristic colors, the parts must not be exposed to outside air for any length of

time during the period that they are released from the carburizing materials into the quenchant. The methods that can be used to achieve this are varied, but for this study the following arrangement was utilized.

Figure 3 shows the new mild-steel carburizing vessels that were fabricated to avoid any potential for cross contamination. All parts were packed in a pre-specified ratio and type of carburizing mixture that was then placed in the bottom of the crucible, filling it about halfway. The sample piece was then carefully placed in the center of the crucible in an upright position, at which point additional mixture was added to the vessel to fill it. Care was taken to keep the parts centered in the crucible and away from the sidewalls. Periodically, the sides of the vessel were tapped with a steel rod to settle the carburizing mixture around the part and remove any voids. Once the vessel was packed, it was fitted with a loose-fitting bottom cap and the assembly was fitted to a steel carrier. The samples were heated to 801°C, starting with a cold furnace for a period of two hours; the first half hour was not counted in order to allow the pack to normalize to the temperature of the furnace. Figure 3 shows how each 18-liter container was fitted with a steel cover plate with an opening at the center in order to aid in the quenching process. The parts were removed from the oven and transferred to the steel plate at which time the crucible was slid over the center hole in the lid, dropping the contents into the quenchant.

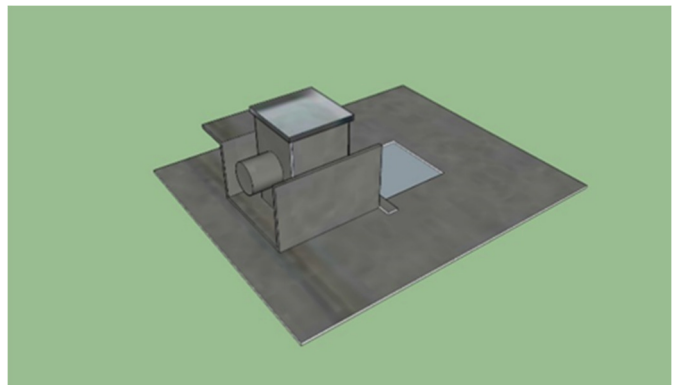


Figure 3. Crucible, carrier, and tank cover used for bone and charcoal color case hardening.

The importance of reducing contact with the outside air cannot be overstated. Earlier attempts to recreate the CCH process were not successful, due largely to the arrangement of removing the pack from the furnace and the quenching operation that followed. Any air that contacts the parts prior to their entry into the quenchant will result in a dull gray, scaled, oxidized surface. A short air gap is permissible, as the parts are partially protected by the gas envelope as they drop from the crucible but, with any substantial drop, the parts will not be colored. The arrangement described above reduces the air gap to less than 0.812 mm, which proved to be ideal.

Results and Discussion

Surface Structure

As Gaddy reported in his 1997 study, the effects of the CCH process on the surface structure of the steel are quite unusual. Observations from this current study agreed with what Gaddy found in the form of crystalline structures of about 1 μ m in size on samples that had been carburized in mixtures with high percentages of bone charcoal (Gaddy, 1997). These globules were generally surrounded by structures that would measure in the nanoparticle range; also, as the percentage of bone charcoal was decreased, and wood charcoal increased, the surface structures exhibited regions of amorphous structure blended with the crystalline structures exhibited with bone charcoal. Figure 4 shows that, with higher concentrations of bone, the surface structures that were produced fell just past the range that one would associate with nanoparticles; however, as the bone decreased, and the mixture used consisted predominately of wood charcoal, the surface structure showed a fine to nearly amorphous structure, which could be within the normal nanoparticle range of 1-100nm in size (Pilotek & Tabellion, 2005).

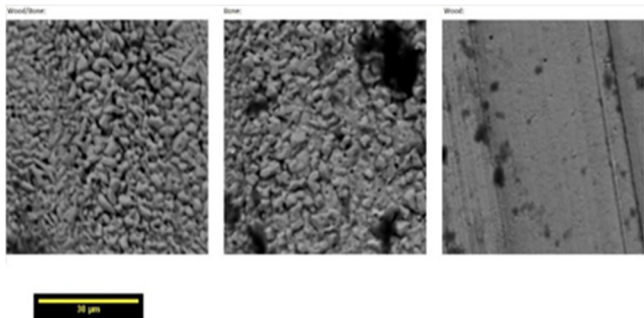


Figure 4. Surface structures of hardened samples. Wood bone (far left), wood (right); and bone (center).

Figure 5 shows that samples also revealed considerable difference in surface structure in hardened versus unhardened states, with hardened samples exhibiting a more refined crystalline structure than those of samples that were not hardened.

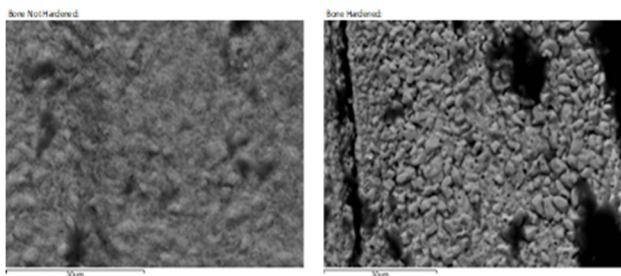


Figure 5. Surface structure of hardened versus non-hardened bone samples.

Chemical analysis of the surface showed that the crystalline structure on the surface was composed largely of iron oxide with small quantities of calcium and phosphorus. The appearance of these elements was interesting, and Gaddy attributed the concentrations of these to the tri-calcium phosphate content of the bone charcoal that was used in the study (Gaddy, 1997). Table 1 provides the chemical analysis of the different samples tested.

Table 1. Elements measured in surface structures of samples.

Sample	C	O	Fe	other	Fe:C	Fe:O
Bone not hardened	46.45	29.92	22.98	0.66	0.49	0.77
Wood/bone	49.04	12.39	36.82	1.76	0.75	2.97
Wood	55.73	11.5	31.33	1.43	0.56	2.72
Wood/bone not hardened	61.08	12.32	25.09	1.51	0.41	2.04
Bone	71.81	7.42	20.1	0.67	0.28	2.71

Optical Properties

One interesting aspect of nanoparticles is that they often have unusual optical properties (Hewakuruppu, Dombrowsky, Chen, Timchenko, Jiang, Baek, & Taylor, 2013). Earlier research indicated that there was some correlation between the structure of the surface and the colors that were produced. To study this impact, preliminary observations were made of the color spectrum on the samples and it was found during the analysis that the areas that exhibited concentrations of blue also exhibited higher concentrations of oxygen than the gray areas in the samples. Figure 6 provides a comparison of the different elements based on color areas.

Comparing Grey Blue and Bright Blue areas on sample 1475F

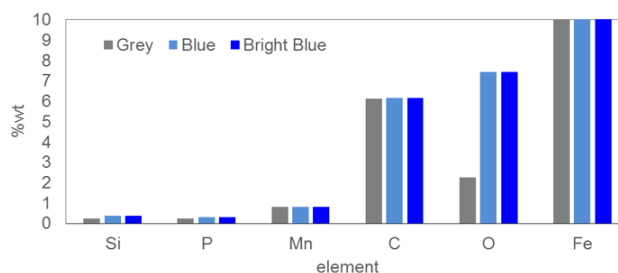


Figure 6. Testing shows that non-colored areas contain less oxygen than blue and bright blue areas.

Case Depth

At the lower temperatures used in the CCH process, the surface tends to absorb a higher concentration of carbon much more quickly than with conventional carburizing operations; however, the depth of this carbon penetration is

also shallower (Woodworth, 1997). The lower temperature range characteristic of CCH processes is one of the major disadvantages when comparing this process to other carburizing methods. Color case hardening requires temperatures below 1500°F in order to be successful in obtaining good color patterns. As was mentioned previously, normal carburizing operations in industry take place in a temperature range from 898°C to 954°C and use more-efficient carburizing mixtures containing highly efficient energizers. Figure 7 illustrates the relationship between temperature time and case depth when using energized wood charcoal. However, though not mentioned in the chart, the energizer that this table was based on was likely considerably more efficient than the bone charcoal that acts as the energizer in the CCH process.

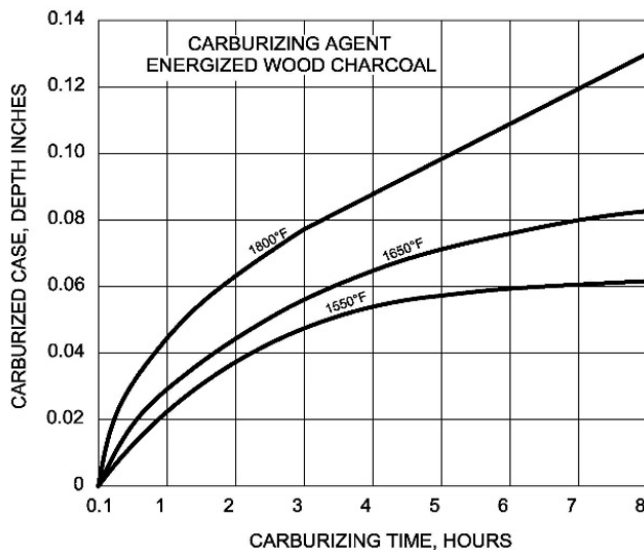


Figure 7. Carburization rate with energized wood charcoal at differing temperatures (Johnson & Yearwood, 2014).

Given the much lower temperatures utilized in the CCH process and the relative inefficiency of the bone charcoal as an energizer, it should be expected that case depths are going to be substantially less than would be expected with more efficient processes. Gaddy's original research looked at the use of the CCH process used by firearms manufacturers, particularly those of the late 19th and early 20th centuries. He noted that in most instances the firearm receivers exhibited characteristics suggesting that they were often quenched at temperatures under the critical temperature range and had very shallow, but file-hard case depths measuring 0.025-0.050 mm (Gaddy, 1997).

These shallow depths would support the hypothesis that these early makers carburized for relatively short length of times at temperatures on the lower end of critical, perhaps even quenching at temperatures considerably under the critical range. In the samples that were observed, case depth was found to range from about 0.101-0.152 mm, though the

samples were likely carburized and tempered at higher temperature ranges and for greater periods of time than what 18th and 19th century firearms manufacturers would have used (Gaddy, 1997). Figure 8 illustrates a comparison between three samples carburized in different carburizing mixtures. By far the deepest case was obtained using a 50/50 ratio of wood and bone, about 0.152 mm, with the depth of the sample carburized in bone measuring about 0.101 mm. The sample carburized with wood only shows little to no depth, likely due to the lack of any form of energizer to enhance carbon monoxide production.

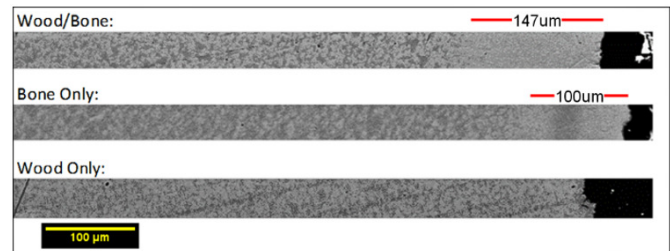


Figure 8. Comparing case depths of hardened samples.

Case Hardness

Color case hardening, just like other carburizing methods, is intended to modify the mechanical properties of low-carbon steel. As mentioned previously, the early uses of this were largely firearms related and, in most instances, the parts that this process was applied to were well suited to this form of heat treatment. Parts that were exposed to considerable amounts of wear were generally made from either high-carbon steels or were subjected to a more conventional carburizing operation, whereby they developed much deeper cases more suitable for the expected use of the parts. As a result, case hardness or depth is not generally the first priority when performing the CCH process, but rather the decorative element of the colors produced, which was noted in Gaddy's earlier research (1997). For this current study, a micro-Vickers hardness test was used on the sectioned samples. This method is preferred over conventional Rockwell hardness tests for case-hardened surfaces (Herring, 2012). Figure 9 provides a photograph of a cross section tested with the Vickers method, and Figure 10 shows the results of the six samples tested.

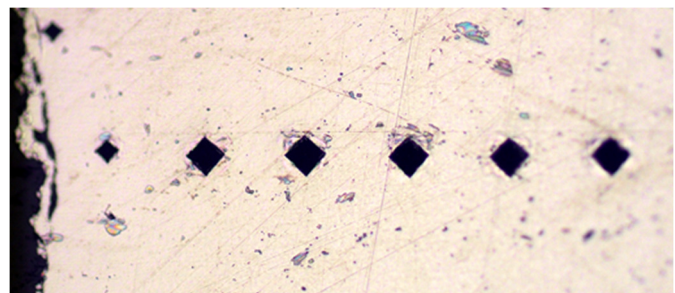


Figure 9. Bone sample showing the Vickers indentations in the surface.

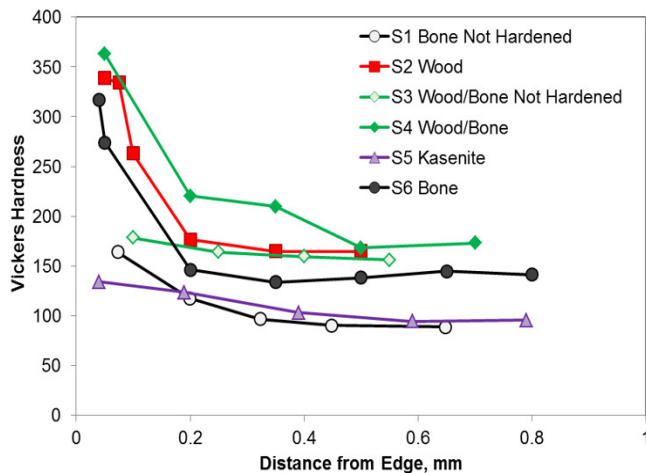


Figure 10. Vickers hardness test results of the six samples.

While the results, in terms of hardness, in Figure 10 are not that impressive, what it suggests is actually quite interesting. The CCH process does not operate at the higher temperatures that are currently the industry standard, yet does tend to yield higher concentrations of carbon at the surface. What the Vickers test seems to show is that the carbon distribution drops off dramatically the further into the case you go. At the surface, the hardness can be described as file hard and measures around 60-62 Rockwell on the surface; but, as the case goes deeper and the carbon concentration declines, the steel behaves like lower-carbon steels with a gradual reduction in the ability to be hardened effectively. Figure 11 illustrates this effect in relation to the carbon content of the steel in relation to hardness.

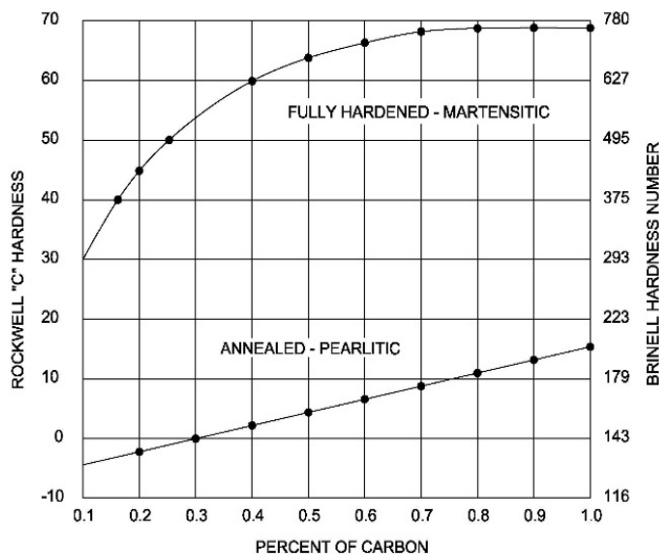


Figure 11. Approximate impact of carbon percentage on hardness of carbon steel in both martensitic and pearlitic conditions (Johnson & Weeks, 1977; Johnson & Yearwood, 2014).

Conclusions

Formation of nanoparticles is currently an area of intense interest to researchers. Given this interest, the use of the CCH process to create a nanostructured surface of iron oxide has a great deal of potential in many sectors and is as yet an area that appears to have seen little research. While the results of this preliminary study show promise, further research is needed regarding the complex surface structures created in the CCH process. The results of this study demonstrate that it might be possible to control the size and structure of the surface. Many technologies have come and gone over the years and, in most instances, this is the result of natural progression. Though many more-effective methods of carburizing have been developed over the years, color case hardening has survived due to the connection that it has maintained with the firearms manufacturing sector. Though the mechanical properties leave much to be desired in regards to carbon case depth, carbon distribution, and hardness, it is the vibrant display of colors produced that are so admired by firearms fanciers that have kept color case hardening alive and saved it from the often lethal effects of time and technological progress.

References

- Brownells-Heat treating charcoal. (n.d.). Retrieved from Brownells: <http://www.brownells.com/gunsmith-tools-supplies/metal-prep-coloring/color-case-hardening/heat-treating-charcoal-prod1231.aspx>
- Fulford, M., Sim, D., Doig, A., & Painter, J. (2005). In defense of Rome: a metallographic investigation of Roman ferrous armour from Northern Britain. *Journal of Archaeological Science*, (32), 241-250.
- Gaddy, O. (1997). The color case hardening of firearms part 1. *The Double Gun Journal*.
- Grossman, M. A. (1937). *A review of some fundamentals of carburizing*. Nineteenth Annual Convention of the American Society for Metals (pp. 1-12). Atlantic City: American Society for Metals.
- Herring, D. H. (2012, August). *Common pitfalls in hardness testing*. Retrieved from Gear Solutions: http://www.gearsolutions.com/media/uploads/assets/PDF/Articles/Aug_12/0812_Herring.pdf
- Hewakuruppu, Y. L., Dombrovsky, L. A., Chen, C., Timchenko, V., Jiang, X., Baek, S., Taylor, R. A. (2013, August 20). Plasmonic "pump-probe" method to study semi-transparent nanofluids. *Applied Optics*, 52(24), 6041-6050. DOI: 10.1364/AO.52.006041
- Howe, J. V. (1941). *The modern gunsmith*. New York: Funk & Wagnalls Company.
- Johnson, C. G., & Weeks, W. R. (1977). *Metallurgy* (5th ed.). (J. G. Anderson, Ed.) Alsip: American Technical Publishers, Inc.
- Johnson, A., & Yearwood, D. (2014). The metallurgical challenge: A meaningful learning activity. *Technology Interface International Journal*, 14(2), 54-62.

-
- Kelly, K. (2010). *What technology wants*. New York: Viking.
- MacFarland, H. E. (1966). *Gunsmithing simplified*. New York: A.S. Barnes & Company.
- Mirza, M. M., Rasu, E., & Desilva, A. (2016). Surface Coatings on Steel Pipes Used in Oil and Gas Industries - A Review. *American Chemical Science Journal*, 13 (1), 1-23.
- Pilotek, S., & Tabellion, F. (2005). Nanoparticles in Coatings. *European Coatings Journal*, (4).
- Vickery, W. F. (1955). *Advanced Gunsmithing*. Georgetown, SC: Small-Arms Technical Publishing Company.
- Woodworth, J. V. (1997). Casehardening processes. In *hardening, tempering annealing and forging of steel* (p.142). New York: The Norman W. Henley Publishing Co.

nology Incorporated. Mr. Beddoe can be reached at cbeddoe@undeerc.org

RAVINDRA THAMMA is a professor and chair of the Manufacturing and Construction Management Department at Central Connecticut State University. Dr. Thamma received his PhD from Iowa State University. His teaching and research interests include robotics, linear control systems, and intelligent systems. Dr. Thamma may be reached at thammarav@mail.ccsu.edu

Biographies

ALEX JOHNSON is an assistant professor in the Department of Applied Engineering, Safety and Technology at Millersville University of Pennsylvania. He earned his BS, MS (Industrial Technology, 2001), and PhD (Teaching and Learning, 2010) degrees from the University of North Dakota. Prior to joining Millersville, Dr. Johnson worked as an assistant professor in the Department of Technology at the University of North Dakota. Dr. Johnson's research interests include engineering and technology education, manufacturing processes, and small wind turbine technology. Dr. Johnson may be reached at alex.johnson@millersville.edu

BLAISE MIBECK is a research scientist at the EERC, where he develops experimental apparatus and analytical techniques. His current interests include quantitative phase analysis, powder x-ray diffraction, computer-controlled scanning electron microscopy, and other material science techniques for the analysis of geological samples. His experience includes work in mercury monitoring, operation of bench-scale flue gas simulators, and developing calibration sources for mercury analysis. He participates in numerous projects where he devises test programs, adapts equipment for nonstandard applications, and develops new operating procedures. He is an associate member of Sigma Xi and holds an MS degree in physics from the University of North Dakota and a BS degree in physics from Lake Forest College. Mr. Mibeck may be reached at bmibeck@undeerc.org

CHRIS BEDDOE is a research engineer in the Applied Geology Laboratory at the EERC, where his work focuses on the derivation of mechanical and chemical properties of rocks and engineered materials of importance to the oil and gas and emerging CO₂ storage industries. He holds a BS degree in mechanical engineering and is pursuing a BS degree in electrical engineering from the University of North Dakota. Prior to his position at the EERC, he served as a Manufacturing Process Engineer at Hutchinson Tech-

UNDERSTANDING THE INFLUENCE OF COLLECTOR SPEED ON THE PROPERTIES OF ELECTROSPUN MEMBRANES FOR USE IN MEMBRANE DISTILLATION

Olawale Makanjuola, Khalifa University of Science and Technology; Khadije El Kadi, Khalifa University of Science and Technology; Isam Janajreh, Khalifa University of Science and Technology

Abstract

Electrospinning is a fast-growing production method for nanoscale fibers, and involves spraying an electrically charged polymeric solution on a rotating drum. Desalination, gas separation, pharmaceutical drug synthesis, and concentration are in heavy use of this technology. The peculiar properties of electrospun membranes—as far as hydrophobicity, high porosity, selectivity, and stability—continue to attract their application in the oil and gas, desalination, medical, and food industries. Their fabrication relies on multiple parameters, including solution properties (i.e., viscosity, conductivity, and surface tension) and operational parameters (i.e., feed rate, applied voltage, tip-to-collector distance, and temperature). Manipulation of these parameters can lead to desirable properties with added values. In this study, the authors evaluated the influence of the collector speed parameter on the properties of desalination membranes. The fabricated membranes were made from a 10% (w/w) poly (vinylidene fluoride-co-hexafluoropropylene) and characterized for morphology, pore size, porosity analysis, surface wettability, and mechanical properties. Results suggest that the collector speed has negligible effect on most electrospun membrane desalination properties and, thus, on mass flux production except porosity and mechanical strength where collector speed has a significant influence.

Introduction

Electrospinning is a rapidly emerging fiber production method that produces nanoscale fibers by drawing charged polymeric threads from solutions or melts in the presence of strong electric fields (Ahmed, Lalia, & Hashaikeh, 2015; Bhardwaj & Kundu, 2010; Doshi & Reneker, 1995). Figure 1 shows the schematic of a simple electrospinning setup with a drum-type collector. Electrospinning has gained significant attention in the research community for the production of desalination membranes (Ahmed, Lalia, Hilal, & Hashaikeh, 2014; Essalhi & Khayet, 2014; Francis, Ghafour, Alsaadi, Nunes, & Amy, 2014; Moradi, Monfared, Amini, & Dastbaz, 2016; Tijing, Choi, Lee, Kim, & Shon, 2014; Tijing, Woo, Johir, Choi, & Shon, 2014).

More specifically, electrospun membranes are attractive for membrane distillation (MD), a non-isothermal mem-

brane process, because they tend to have higher porosities (i.e., 10-20% more) than that of conventional membranes made by phase inversion (Subramanian & Seeram, 2013). Additionally, they are characterized by higher surface hydrophobicity than membranes produced from the same materials via other methods (Kaur, Sundarajan, Rana, Sridhar, Gopal, Matsuura, & Ramakrishna, 2014; Lee, Boo, Ryu, Taylor, & Elimelech, 2016), a property which is desirable for MD. Several factors affect the electrospinning process and, ultimately, the resulting membranes. These factors include solution properties, such as viscosity, conductivity, and surface tension, and operational parameters, such as feed rate, applied voltage, tip-to-collector distance, humidity, and temperature. Researchers have indicated that by appropriately varying any of these parameters, nanofibrous materials and membranes with desirable physical properties can be made (Bhardwaj & Kundu, 2010; Doshi & Reneker, 1995; Huang, Zhang, Kotaki, & Ramakrishna, 2003). Moreover, different arrangements of fibers can be obtained by using a rotating collector (drum), but how these arrangements affect the properties of the membranes is still unraveling.

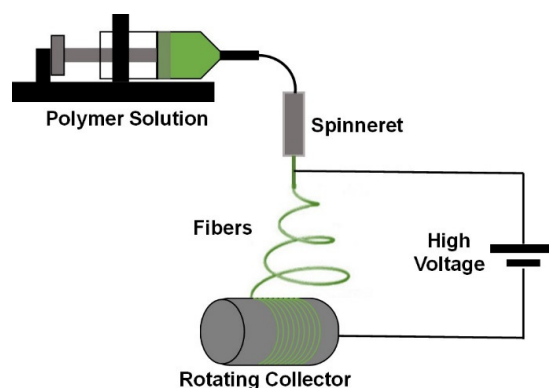


Figure 1. Electrospinning schematic.

While extensive studies have been conducted to understand how operational and solution parameters affect the properties of electrospun membranes applied to desalination, most of these have paid less attention to the effect of a collector's rotating speed on membrane properties for desalination. In this paper, the authors report current findings on how collector speed affects the properties of MD membranes fabricated by electrospinning and, thus, the distilla-

tion flux. In this current study, electrospun membranes were made from a 10% (w/w) poly (vinylidene fluoride-co-hexafluoropropylene) solution under different collector speeds. The fabricated membranes were characterized for morphology, pore size, porosity analysis, surface wettability, and mechanical properties. Additionally, the distillation flux was estimated and compared for the different fabricated membranes.

Materials and Methods

PVDF-HFP (Kynar Powerflex LBG, $M_w = 450,000$ gmol^{-1}), acetone (Aldrich, CHROMASOLV, for HPLC, $\geq 99.8\%$), and N, N-dimethylacetamide (Aldrich, CHROMASOLV plus, for HPLC, $\geq 99.9\%$) used for membrane fabrication were all used as received. A polymer solution was prepared by dissolving 10 wt% PVDF-HFP in a mixture of solvents at room temperature. The solvent mixture contained, by weight, 70% acetone and 30% N, N-dimethylacetamide. Dissolution of the polymer in the solvent mix was achieved by magnetically stirring the solution at 300 rpm for 24 hours, followed by atmospheric degas for 30 minutes. The solution was loaded into a 10-mL plastic syringe connected via a Teflon pipe to an 18-gauge stainless steel needle (internal diameter = 0.838 mm). The loaded syringe was clamped into a Nanon-01A electrospinning setup (MECC Japan) containing a rotating drum collector covered with aluminum foil.

Figure 1 shows how the electrospinning procedure was conducted under the following conditions: 25 kV potential, 15 cm tip-to-collector distance, 1 mL h^{-1} feed rate, 50% relative humidity, and room temperature. To evaluate the effect of collector speed on the properties of the resulting membrane, the drum rotational speed was varied from 100 to 1000 rpm. After spinning the 30-mL polymer solution, the membrane was separated from the aluminum foil and dried in an oven at 50°C for 24 hours. Table 1 lists the membranes that were produced, and are coded according to collector speed.

Table 1. Membrane coding with associated properties.

Membrane code	Collector Speed (rpm)	Thickness (μm)
M1	100	185 ± 3.24
M3	300	183 ± 4.39
M5	500	185 ± 3.38
M7	700	183 ± 4.18
M10	1000	150 ± 5.42

As part of investigating the effect of collector speed on the properties of membranes and their performance in an MD test, the permeation flux yield (J) was assessed theoretically using Equation 1:

$$J = c_m \Delta P_{sat} \quad (1)$$

where, ΔP_{sat} is the transmembrane water vapor pressure difference estimated using the Antoine equation (Blackshaw, 1979). On the other hand, c_m is the mass transport coefficient that can be described using the simplified Knudsen-Poiseuille combination model (Chen, Ho, & Yeh, 2009; Janajreh, El Kadi, Hashaikh, & Ahmed, 2017; El Kadi, Janajreh, & Hashaikh, 2017), as described by the mass coefficient in Equation 2, and each is defined in Equations 2 and 3:

$$c_m = c_K + c_P \quad (2)$$

$$c_K = 1.064 \frac{\epsilon r_p}{\tau \delta_m} \sqrt{\frac{M_w}{RT_m}} \quad (3)$$

$$c_P = 0.125 \frac{\epsilon r_p^2}{\tau \delta_m} \frac{M_w P_m}{RT_m \mu_v} \quad (4)$$

As can be seen from Equations 3 and 4, the mass transfer coefficient is highly dependent on membrane properties, mainly the porosity, pore size, thickness, and tortuosity. In this regard, the performance of direct-contact MD using membranes M1 through M10 was estimated assuming a counter flow configuration with a feed temperature of 75°C, permeate temperature of 25°C, flow velocities of 0.1 m/s, and a temperature polarization coefficient of 0.7.

Results and Discussion

To aid in the discussion of the results, the fabricated membranes were coded according to the collector speed (see again Table 1). This table also provides data for associated membrane thickness. With the exception of M10, all of the membranes had nearly the same thicknesses, as measured by a micrometer. This was probably because equal volumes of polymer solution were spun for the same amount of time for of all the membranes. Notably, the very high speed of 1000 rpm caused the fibers of M10 to be more spread out across the collector surface; hence, the lower thickness.

Figure 2 shows that, as obtained from capillary flow porometry measurements, pore size increased only slightly with increasing collector speed, giving M10 the largest mean and maximum pore size. A low collector speed favors a more random orientation of fibers as they are collected. This, in turn, increases the chances for large pores to become smaller along a 2-dimensional plane. However, as the rotational speed of the drum was increased, the tendency of produced fibers to align in the direction of rotation increased, thereby reducing the chances of closing large pores

once they formed. Figure 3 shows that porosity, on the other hand, was observed to be significantly affected by collector speed. The general decrease in overall porosity with increasing collector speed was likely due to unidirectional alignment of fibers which can close 3-dimensional pore spaces. In MD, high membrane porosity is desired for higher fluxes and lower conduction heat losses (Mulder, 2012). However, very high porosity can compromise the mechanical strength of the membrane. Fortunately, the mechanical strength requirement for MD is much lower than that for pressure-driven membrane processes (Khayet & Matsuura, 2011).

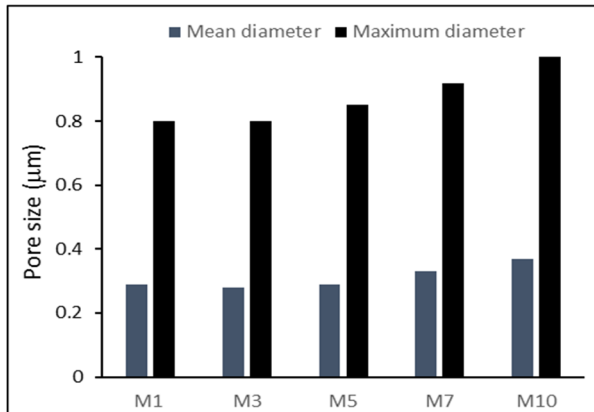


Figure 2. Membranes mean and maximum pore size diameter.

One of the main requirements of MD membranes is that they be hydrophobic (i.e., non-wetted). In fact, membrane superhydrophobicity is desired in order to prevent pore wetting during long-term MD processes. The cylindrical nanofibers obtained from electrospinning feature a first-level re-entrant structure that makes electrospun membranes more hydrophobic than membranes made using the more common phase inversion process (Lee et al., 2016). Surface wettability of the membranes was evaluated using contact angle measurements. Figure 4 shows that the contact angle (i.e., hydrophobicity) of the membrane was only slightly affected by collector speed. While the contact angle was higher for speeds above 100 rpm, how the speed affected contact angle was not particularly clear. Perhaps the surface roughness was slightly elevated by alignment of the fibers in one direction. The liquid entry pressure (LEP) was the minimum amount of pressure that had to be applied before the non-wetted membrane was wetted. High LEP is desirable in order to sustain the MD process. Figure 5 shows that, like the contact angle data, LEP was generally higher at collector speeds above 100 rpm. Notably, the LEP of the M10 was the lowest, likely because this membrane had the highest maximum pore size (1.01 µm). LEP is related to contact angle and pore size by the Laplace-Young equation (Franken, Nolten, Mulder, Bargeman, & Smolders, 1987):

$$LEP = \frac{-4B\gamma_L \cos \theta}{\delta_{max}}$$

where, B is a dimensionless geometrical factor that accounts for pore irregularity, γ_L is the surface tension of the test liquid (water in the current case), θ is the contact angle, and δ_{max} is the maximum pore diameter. Thus, large pores will result in low LEP. To understand if δ_{max} for M10 was solely responsible for its low LEP, the dimensionless parameter B was calculated for all of the membranes and compared in Table 2. Since all of the membranes had nearly the same B value, one can conclude that the large pore size of the M10 membrane was the reason for its low LEP.

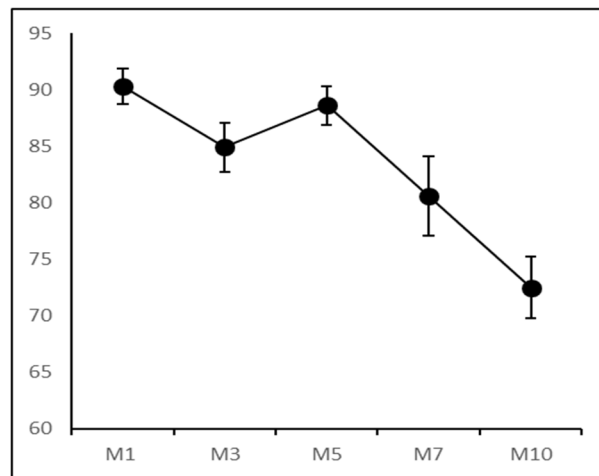


Figure 3. Membranes mean porosity measurement.

Table 2. Dimensionless parameter B for M1 – M10 membranes.

Membrane code	Dimensionless factor B ($\times 10^{-6}$)
M1	1.01
M3	1.04
M5	1.07
M7	1.18
M10	1.12

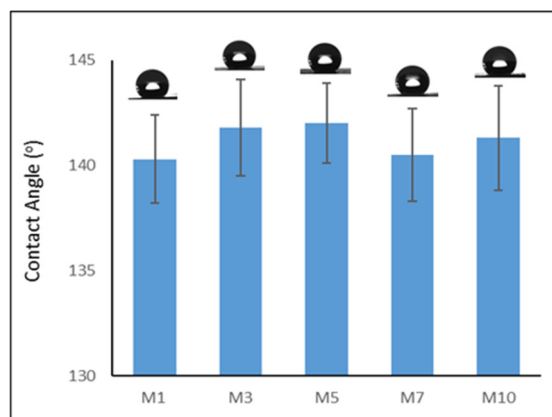


Figure 4. Contact angle measurements of membranes.

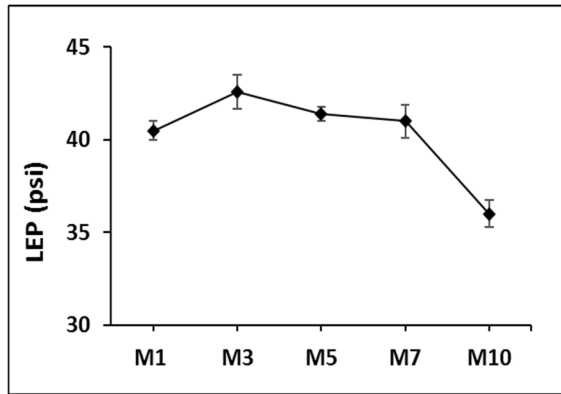
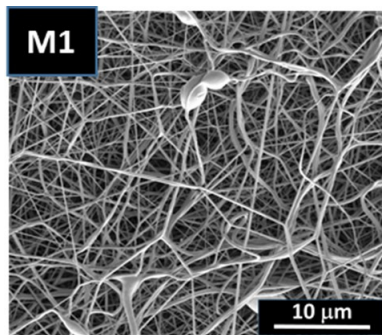
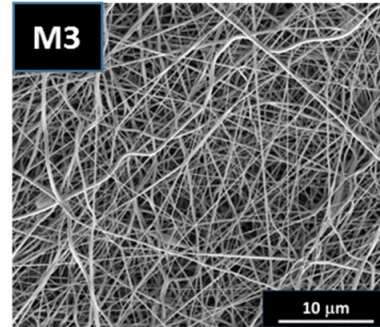


Figure 5. Liquid entry pressure of membranes.

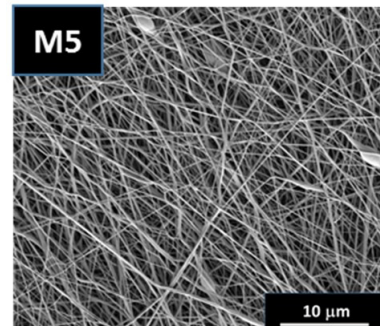
Figure 6(a-e) shows the surface micrograph of the fabricated membranes obtained using a Quanta FEG 250 FEI scanning electron microscope operated at 2kV. Smooth fibers with negligible beads were obtained for M1–M10, and all of the membranes had roughly equal average fiber diameters of about 140 nm. As the collector speed increased, the fibers became more aligned in the direction of collector rotation. The micrograph of M10, however, suggests that at very high collector speeds, deposition of fibers on the collector becomes quite unstable, thereby preventing alignment of fibers in the rotational direction. Finally, the mechanical properties of the membranes were evaluated using a universal tensile testing machine. A dog-bone specimen of each membrane was pulled in tension along two axes (i.e., parallel and perpendicular to the direction of collector rotation). Figure 7(a) shows the stress-strain curves for the membranes tensioned parallel to the direction of collector rotation. As the figure suggests, tensile strength in this direction increased from about 7.2 MPa to 9.8 MPa with rotational speed. This may have been due to the fibers aligning themselves in the rotational direction as speed increased, leading to strengthening of the membranes. However, at extremely high speeds (1000 rpm), deposition of fibers on the collector was unstable and alignment of fibers was lost, leading to a reduction in strength. Percent elongation of the membranes varied from about 54% to 72% with no clear correlation with collector speed.



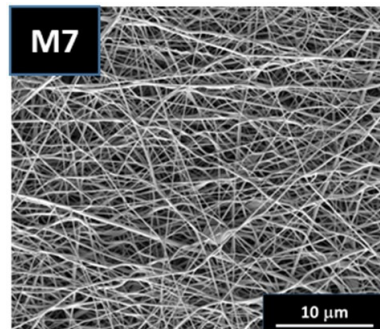
(a) M1 membrane fibers



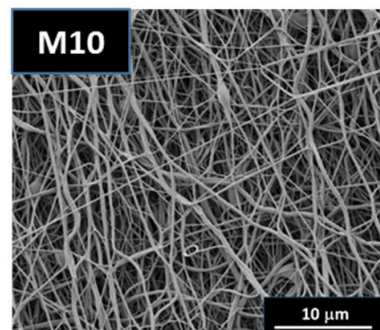
(b) M3 membrane fibers



(c) M5 membrane fibers



(d) M7 membrane fibers



(e) M10 membrane fibers

Figure 6. SEM images for M1 – M10.

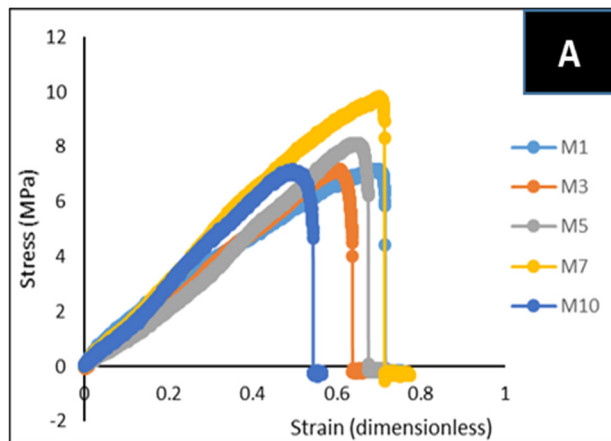
Intuitively, one would expect the tensile strength of the membranes to decrease with collector speed, when tensioned perpendicular to the rotational direction, since alignment of fibers will approach zero in this direction. Indeed, what was observed approximated what one would expect. Figure 7(b) shows that the tensile strength decreased with increasing collector speed from about 6.82 MPa to 2.1 MPa, as the collector speed was increased from 100 to 1000 rpm. Percent elongations for this loading were generally higher than that obtained for parallel loading and varied from about 76% to 97%. The reason for this was probably because the fibers reorient themselves to align with the direction of applied tensile force. In general, as the deposition of polymer fibers on the collector approaches random orientation, the tensile strength of electrospun membranes in both loading directions approaches the same value.

Figure 8 shows the estimated average mass flux, as per Equation 1, for different membranes used in direct contact MD, where all flow parameters were fixed. The highest flux of almost 21.4 kg/m².h was recorded for M10, which had the lowest thickness of 150μm and largest mean pore size of around 0.37 μm. When M1 and M7 were compared with each other, it was found that the much higher porosity of M1 (90.35%), compared to 80.6% for M7, dominated other properties and led to higher flux than that of M7. The poorest flux was recorded for M3 and was clearly due to the relatively small pore size of 0.28 μm. Pore size and porosity were found to be the most dominant parameters, due to their higher-order effect, as seen in Equations 3 and 4. With the exception of porosity, the changes in membrane parameters from earlier results were negligible. Therefore, the overall averaged mass flux illustrated a maximum gain of 2.7%, when collector speed was increased by 700 rpm.

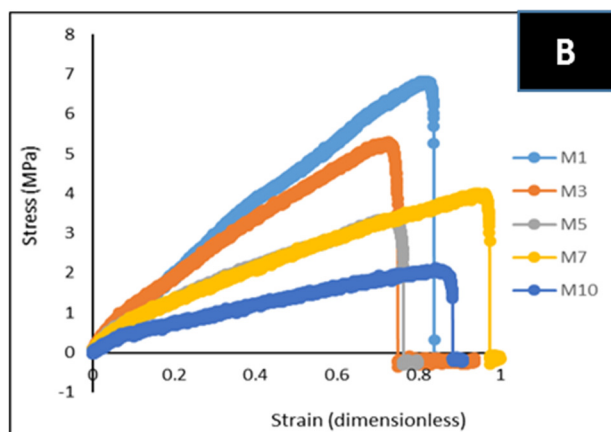
Conclusions

The collector speed parameter of the electrospinning membrane was studied in order to assess its influence on the properties of 10% (w/w) poly (vinylidene fluoride-co-hexafluoropropylene). The synthesized membranes were and characterized for morphology, pore size, porosity analysis, surface wettability, and mechanical properties. Furthermore, their desalination performance was assessed following well-developed and validated literature models. Based on the results obtained, it appeared that the collector speed had a negligible effect on most electrospun membrane MD properties and, thus, on mass flux production except porosity and mechanical strength where collector speed exerts a significant influence. The highest attained flux was 21.4 kg/m².h, recorded for M10, which was characterized as having the lowest thickness (150 μm) and largest mean pore size (roughly 0.37 μm). The pore sizes of M1 and M7 were found to be 90.35% and 80.6%, respectively. The smallest flux was recorded for M3, which was also characterized with the smallest pore size of 0.28 μm. Changes in membrane parameters were negligible, except for porosity and

pore size when the collected speed changed. The overall gain in the permeated flux was 2.7% when collector speed was increased to 700 rpm.



(a) Tensioned parallel to rotational direction



(b) Tensioned perpendicular to rotational direction

Figure 7 Stress-strain curves for M1 – M10.

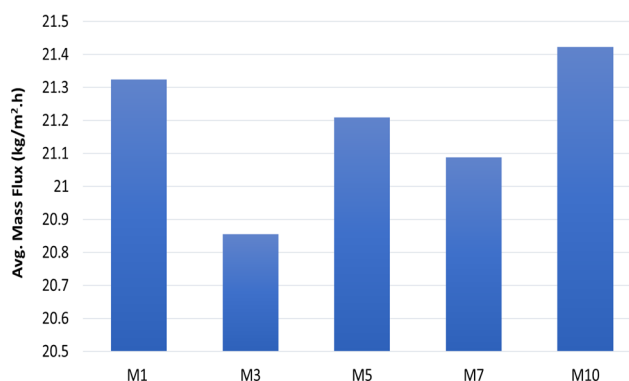


Figure 8. Comparison of average yield mass flux of direct contact MD process using membranes M1, M3, M5, M7, and M10.

Acknowledgements

Support received from ADNOC Takreer Refinery Center of Membrane and Advanced Water Technology at Khalifa University is highly acknowledged.

References

- Ahmed, F. E., Lalia, B. S., Hilal, N., & Hashaikh, R. (2014). Underwater superoleophobic cellulose/electrospun PVDF-HFP membranes for efficient oil/water separation. *Desalination*, 344, 48-54.
- Ahmed, F. E., Lalia, B. S., & Hashaikh, R. (2015). A review on electrospinning for membrane fabrication: challenges and applications. *Desalination*, 356, 15-30.
- Bhardwaj, N., & Kundu, S. C. (2010). Electrospinning: a fascinating fiber fabrication technique. *Biotechnology advances*, 28(3), 325-347.
- Blackshaw, G. L. (1979). Elementary principles of chemical processes by Richard M. Felder and Ronald W. Rousseau, John Wiley and Sons (1978), 571 *AIChE Journal*, 25(2), 382-382.
- Chen, T. C., Ho, C. D., & Yeh, H. M. (2009). Theoretical modeling and experimental analysis of direct contact membrane distillation. *Journal of Membrane Science*, 330(1-2), 279-287.
- Doshi, J., & Reneker, D. H. (1995). Electrospinning process and applications of electrospun fibers. *Journal of electrostatics*, 35(2-3), 151-160.
- El Kadi, K., Janajreh, I., & Hashaikh, R. (2017, December). Low Energy Desalination via DCMD: The Role of Superhydrophobicity and Optimal Flow Conditions. In 2017 International Renewable and Sustainable Energy Conference (IRSEC) (pp. 1-6). IEEE.
- Essalhi, M., & Khayet, M. (2014). Self-sustained webs of polyvinylidene fluoride electrospun nano-fibers: Effects of polymer concentration and desalination by direct contact membrane distillation. *Journal of Membrane Science*, 454, 133-143.
- Francis, L., Ghaffour, N., Alsaadi, A. S., Nunes, S. P., & Amy, G. L. (2014). PVDF hollow fiber and nanofiber membranes for fresh water reclamation using membrane distillation. *Journal of Materials Science*, 49(5), 2045-2053.
- Franken, A. C. M., Nolten, J. A. M., Mulder, M. H. V., Bargeman, D., & Smolders, C. A. (1987). Wetting criteria for the applicability of membrane distillation. *Journal of Membrane Science*, 33(3), 315-328.
- Huang, Z. M., Zhang, Y. Z., Kotaki, M., & Ramakrishna, S. (2003). A review on polymer nanofibers by electrospinning and their applications in nanocomposites. *Composites science and technology*, 63(15), 2223-2253.
- Janajreh, I., El Kadi, K., Hashaikh, R., & Ahmed, R. (2017). Numerical investigation of air gap membrane distillation (AGMD): Seeking optimal performance. *Desalination*, 424, 122-130.
- Kaur, S., Sundarajan, S., Rana, D., Sridhar, R., Gopal, R., Matsuura, T., & Ramakrishna, S. (2014). The characterization of electrospun nanofibrous liquid filtration membranes. *Journal of Materials Science*, 49(18), 6143-6159.
- Khayet, M., & Matsuura, T. (2011). *Membrane distillation: principles and applications*. Elsevier.
- Lee, J., Boo, C., Ryu, W. H., Taylor, A. D., & Elimelech, M. (2016). Development of omniphobic desalination membranes using a charged electrospun nanofiber scaffold. *ACS applied materials & interfaces*, 8(17), 11154-11161.
- Moradi, R., Monfared, S. M., Amini, Y., & Dastbaz, A. (2016). Vacuum enhanced membrane distillation for trace contaminant removal of heavy metals from water by electrospun PVDF/TiO₂ hybrid membranes. *Korean Journal of Chemical Engineering*, 33(7), 2160-2168.
- Mulder, J. (2012). *Basic principles of membrane technology*. Springer Science & Business Media.
- Subramanian, S., & Seeram, R. (2013). New directions in nanofiltration applications—Are nanofibers the right materials as membranes in desalination? *Desalination*, 308, 198-208.
- Tijing, L. D., Choi, J. S., Lee, S., Kim, S. H., & Shon, H. K. (2014). Recent progress of membrane distillation using electrospun nanofibrous membrane. *Journal of Membrane Science*, 453, 435-462.
- Tijing, L. D., Woo, Y. C., Johir, M. A. H., Choi, J. S., & Shon, H. K. (2014). A novel dual-layer bicomponent electrospun nanofibrous membrane for desalination by direct contact membrane distillation. *Chemical Engineering Journal*, 256, 155-159.

Biographies

OLAWALE MAKANJOLAB is a membrane fabricator, who completed his MSc in Materials Science and Engineering from Khalifa University with collaboration from MIT (2018) and is now pursuing a PhD from NYU. He has a notable contribution to membrane fabrication for membrane distillation technology and has published several works in international journals such as the *Journal of Membrane Science* and *Desalination*. Mr. Makanjoulab may be reached at olawale.makanjuola@ku.ac.ae

KHADIJE EL KADI is a research engineer in the Center of Membrane and Advanced Water Technology at Khalifa University of Science and Technology, Abu Dhabi, UAE. El Kadi received her MSc in Mechanical Engineering from Khalifa University with collaboration from MIT (2018), and her BSc in Sustainable and Renewable Energy Engineering from the University of Sharjah with honors (2016). Khadije is a CFD modeler focusing on thermo fluids and phase change problems as membrane distillation, freeze desalination, solar pond, and wind energy. She has published over 15 articles in international journals, such as *Desalination*, *Oil & Gas Science and Technology*, and *IEEE*. Ms. El Kadi may be reached at khadije.elkadi@ku.ac.ae

ISAM JANAJREH is a professor and associate chair in the Mechanical Engineering Department at Khalifa University Abu Dhabi. He received his MS and PhD degrees from Virginia Tech. in Engineering Science and Mechanics (ESM) and Mechanical Engineering (ME), specializing in fluid dynamics, thermochemical conversion, solid/fluid interactions, and turbulence modeling. Isam joined KU in 2007, spending one year at MIT as a visiting professor and conducting research on thermochemical conversion and assisting in advising students. He has authored over 100 refereed publications on energy conversion and has made many contributions to international conferences. He was a key contributor on three Michelin and another three KU patents (Catamarans, Primacy, X-one, bioreactor), and three books (traction, rolling resistance, and noise). He was the organizer of the Arab Academy of Science conference series (2010-2013), a regular reviewer for several international journals (EC&M, Applied Pyrolysis, Renewable Energy, Fuel), chief editor (IJERSTE) and associate editor (IJTEE), and has been a member of ASME, TS&T, Rubber Division, ASCE, and several international scientific committees. Dr. Janajreh may be reached at Isam.janajreh@ku.ac.ae

Appendix A: Nomenclature and Abbreviations

Abbreviations

MD	Membrane distillation
LEP	Liquid entry pressure
PVDF	Polyvinylidene fluoride
HFP	Hexafluoropropylene

Symbols

J	Average permeation mass flux (kg/m ² .h)
c_m	Membrane mass transfer coefficient (-)
ΔP_{sat}	Transmembrane water vapor pressure (Pa)
c_k	Knudsen mass transfer model coefficient (-)
c_p	Poiseuille mass transfer model coefficient (-)
ε	Membrane porosity ratio (-)
r_p	Membrane pore radius (m)
τ	Membrane tortuosity (-)
δ_m	Membrane thickness (m)
M_w	Membrane molecular weight (g/mol)
R	Universal gas constant (J/mol. K)
T_m	Membrane mean temperature (K)
P_m	Membrane mean pressure (Pa)
μ_v	Water vapor viscosity (kg/m.s)

USING AUTOMATED HORIZON DETECTION TO DETERMINE IMAGE ACQUISITION TIME

Curtis Cohenour, Ohio University

Abstract

Horizon extraction from aerial imagery is a useful tool for determination of roll and pitch. This can be used as primary or supplementary attitude information for aerial vehicles or ground vehicles. In this study, horizon extraction was used to determine aircraft roll from a series of aerial images. Roll information was also extracted from the Global Positioning System (GPS) / Inertial Measurement Unit (IMU). The roll from the image was correlated with the GPS/IMU roll in order to determine the time each image was captured. The resulting time-synchronized images could then be projected over the terrain to form a geo-registered map view of the terrain, such as Google Earth. The horizon was modeled as a straight line. The sky was modeled as white with a pixel value of 255 out of 255. The ground value was chosen from the imagery as the mean of the non-sky values by examining a histogram of the image intensity data. The horizon line was used to separate sky from ground. The slope and intercept of the line were computed using ordinary least squares (OLS). The algorithm is straightforward and well suited to this data set. Using roll angle extracted from imagery to compute time is a novel application of horizon extraction. In this case it was used to correct image time errors. The algorithm could also be used to synchronize images collected without time information.

Introduction

In this study, an aerial image data set—consisting of images and pose data—was corrupted, due to errors in the time stamping of the images. The pose data came from a Global Positioning System (GPS) / Inertial Measurement Unit (IMU) and included position velocity attitude and time (PVAT). The GPS time was used to set the system time. The images were time stamped using the system time. During post-flight analyses, it was discovered that the image time stamps were incorrect. To correct the image time stamps, a horizon extraction algorithm was created in order to extract the aircraft roll angle. The roll angle was then correlated with the GPS inertial roll angle to identify the errors and correct the image time stamps. True time was defined as the GPS second of the week (SOW) from the GPS receiver. The data collection system set the computer system time to the true time. The images were time stamped as they were received with the computer system time. Any difference between the image time and the true time represented a time error. Collecting images with accurate time synchronization can be challenging. Time synchronization errors can lead to errors in projection or navigation, depending on the application. In the past, Ohio University (OU)

worked with the Air Force Research Lab on projects involving the projection of imagery over terrain (Cohenour, Price, Rovito, & van Graas, 2015a; Cohenour, Price, Rovito, & van Graas, 2015b). In this case, errors in the GPS receiver created errors in the image time stamps. These time errors were computed during post processing by using ordinary least squares (OLS) with the time error as an independent variable. The flight test data collection system was then revised to correct the time stamps by modifying the GPS receiver firmware and the data collection software. OU has collected image and navigation data on the OU-owned and operated DC-3 and ground vehicles (Fischer & Raquet, 2011). This project included several data collection systems, each with unique challenges.

The OU Baron 58 was equipped for a flight test with a forward-looking camera, sensors, and a data collection system. To determine the accuracy of the image time synchronization, ground tests were conducted using the OU GPS timing board developed by Cohenour (2019). This device has sixteen light emitting diodes (LEDs) that show the GPS second of the week (SOW) modulo 64 with a resolution of 1/1024 of second. These tests showed errors of one or two seconds in the time synchronization. The errors were corrected in software and the system retested before the flight. Unfortunately, time synchronization errors developed during the flight and the images collected in the air were not synchronized with the GPS data. In this paper, the author explains how the image time stamps were corrected so that the image data could be used.

Correcting the time stamps was performed by extracting the aircraft roll from the images and then correlating the roll from the images with the roll angle from the GPS / IMU. There are several publications regarding the extraction of the horizon from an image. The dissertation by Crisman (2016) includes a summary of horizon extraction methods—optimization, classification, and line/edge detection. Crisman further assumed the horizon to be a curve. In this current paper, the horizon was modeled as a straight line. In both cases, pixels were assigned a value for sky or ground, based on the intensity of the pixel. Parameters of the line were computed to minimize the amount of sky below the horizon and the amount of ground above the horizon. In the Crisman study, a color camera was used and the sky was assumed to be blue, as opposed to the ground which is not blue. The image data collected for this current study was captured from a black-and-white (BW) camera. Instead of using color (blue), image intensity was used. The sky was bright, nearly saturating the camera, while the ground intensity was the mean of the non-sky area based on a histogram of the image.

In a study by Bouyssounouse, Nefian, Thomas, Edwards, Deans, and Fong (2016), the attitude of a planetary rover was derived by comparing the image horizon with a model of the horizon as seen from the rover. The horizon model was derived from a terrain database. Given the estimated location and attitude of the rover, the predicted horizon was computed from the terrain database. The location and attitude of the rover was then refined using maximum likelihood estimation. With a rover on the ground, terrain features such as mountains provide a complex horizon with high observability. In this data set, with an aircraft at altitude, the horizon tends towards a straight line and the terrain features do not provide a significant improvement in observability. For this reason, the horizon model used in this current study was a straight line. In a study by Carrio, Bavle, and Campoy (2018), an edgeless algorithm was used to create a redundant attitude system using an infrared (IR) camera in a system that was assumed to be a straight line; the author of this current study made the same assumption.

Another system described by Ahmad, Bebis, Nicolescu, Nefian, and Fong (2015) used machine learning and dynamic programming to create a horizon that was more complex than simple line segments and curves. The algorithm used here was successful in part because the image data contained a well-defined straight horizon. In addition, the images and the GPS/IMU data were recorded on the GPS second, such that the error between the image time stamps and the GPS/IMU data was an integer number of seconds.

Hardware

Flight test data were collected using the OU Baron 58 on May 6, 2016. Figure 1 shows a block diagram of the image and GPS/IMU component. The camera was a Prosilica GC1350. The 1-pulse-per-second (1PPS) output of the Novatel GPS/IMU was connected to the camera sync port. The camera captured and outputted one image per second, on the second. The Novatel GPS/IMU transmitted position and attitude data to the data collection system every second, on the second. The data collection system used the GPS time from the Novatel to synchronize the system time to GPS time. The Ethernet interface between the camera and the data-collection computer provided setup information for the camera and recorded images from the camera. As images were received from the camera, they were time stamped (in the file name) using synchronized system time and saved to disk.

Theoretically, the images should have been time stamped with GPS time, but they were not. Possible reasons for this are that there were serial messages “hung” in the buffer such that when the software synced the system time, it was using an old message; or, the images were “hung” in the image buffer and were not being time stamped and recorded in real time. Once collected, the data were useless unless the correct time could be recovered.

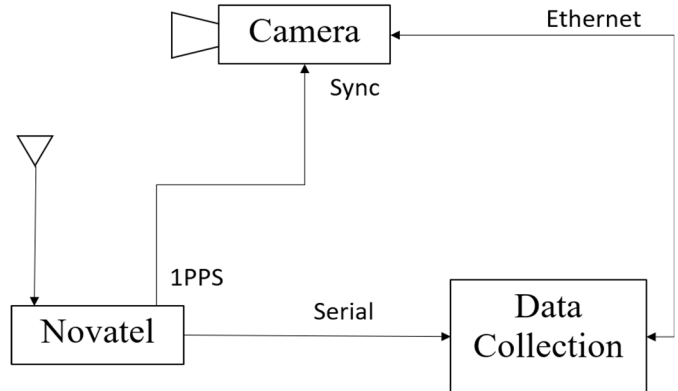


Figure 1. Hardware configuration.

Ground Testing

Figure 2 shows how the ground tests were conducted using the OU GPS clock Cohenour, 2019). The clock in Figure 2 had a GPS receiver and displayed the GPS second of the week (SOW) modulo 64 with a resolution of 1/1024 sec and an accuracy better than 0.1 msec. The integration time (exposure time) of the images was in excess of 1 msec. To verify the time synchronization, an image of the clock was captured and the pattern of lights on the clock was decoded to extract the true GPS time at which the image was captured. This was compared to the synchronized system time in the image file name. Any errors between the synchronized system time in the file name and time derived from the image of the clock was an error attributable to the data collection equipment. Errors of one and two seconds were found in ground tests. These errors were identified as software issues and the software was modified to correct the time synchronization.

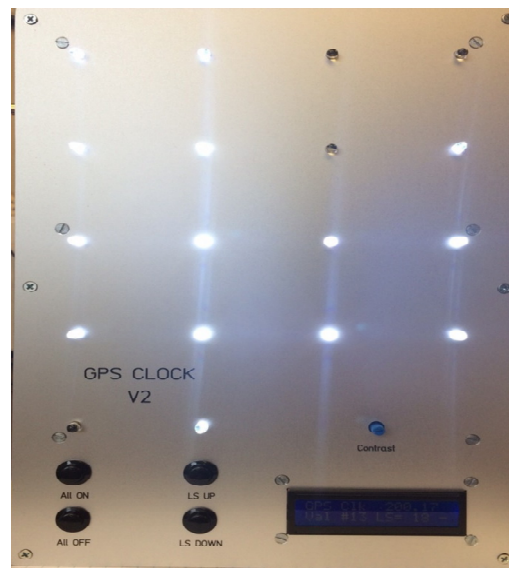


Figure 2. GPS clock, 16 LEDs display GPS SOW modulo 64 with 1/1024 second resolution and an accuracy of 100µsec.

Once the ground tests were completed, the system was flown. However, in working with the imagery, it was discovered that there were large time registration errors. This was obvious by looking at the aircraft location in Google Earth and comparing it to the airborne image data. The time synchronization errors rendered the data set unusable. To salvage the data set, the errors were identified using the horizon algorithm to identify and correct the data set.

Horizon Algorithm

Figure 3 is an image from the Baron flight test of May 6, 2016. The aircraft is in a roll to line up with East State Street in Athens, Ohio. The camera was mounted in the nose of the aircraft and pitched down 11°. The horizon is a straight line. A dark line shows the horizon, as calculated by the algorithm. Each pixel in the image has a value of 0 to 255. A model image was created where points above the line were assigned a value of 255 for sky, and points below the line were assigned a value of 85 for ground. The parameters of the line were computed in order to minimize the error between the image and the model.



Figure 3. Image from the OU Barron 58 turning to line up with East State Street in Athens, Ohio. The dark line at the horizon was generated using the OLS algorithm.

Figure 4 shows a histogram of the image data. The sky is to the right and the ground is to the left. The sky is nearly saturated with 25,000 points, having an intensity of 255/255. The ground has a peak at 85. The ground intensity was set to 85/255, based on the horizontal location of the non-sky peak in Figure 4. The image in Figure 3 is 1024 x 1360. To model the horizon, the coordinates were shifted such that the center of the image was at (0,0) with the x-axis increasing from left to right, and the y-axis increasing from the bottom of the image to the top of the image. The horizon was initialized as a horizontal line at $y = 0$ with a slope of 0. In Equation 1, both m and b are initialized to zero:

$$y = mx + b \quad (1)$$

where, y is the vertical coordinate in pixels with 0 at the center of the image increasing toward the top of the image; x is the horizontal coordinate in pixels with 0 at the center and increasing to the right; m is the slope of the line in y pixels per x pixel; and, b is the y intercept in pixels.

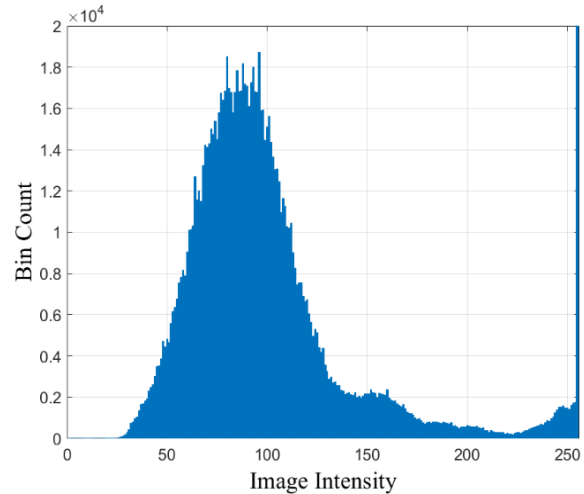


Figure 4. Histogram of image data: the ground is set at 85, the sky is set to 255, the peak at 255 continues to 25,000.

A model of the horizon is constructed in Equation 2, where the sky intensity above the line was set to 255/255 and the ground intensity, below the line, was set to 85/255:

$$y \geq mx + b \quad (2)$$

This is summarized in Equation 3:

$$\hat{P}_{x,y} = \begin{cases} I_{sky} & \text{for } y \geq mx + b \\ I_{ground} & \text{for } y < mx + b \end{cases} \quad (3)$$

where,

$\hat{P}_{x,y}$ is the pixel in the model image.

\hat{P} is located at coordinates x and y .

I_{sky} is the sky intensity 255/255.

I_{ground} is the ground intensity 85/255.

The model image was subtracted from the actual image and squared pixel by pixel. The 1,392,640 squared pixel errors were summed and divided by 1,392,640 to get the RMS error for the image. Ordinary least squares (OLS) (Kariya & Kurata, 2004) was used to find the values of m and b that produced the lowest RMS error. The computed RMS error is given by Equation 4:

$$E_{RMS} = \left(\sum_{x=1}^{1360} \sum_{y=1}^{1024} (\hat{P}_{x,y} - P_{x,y})^2 \right) / 1,392,640 \quad (4)$$

where, E_{RMS} is the RMS error between the model image and $P_{x,y}$ is the pixel in the image located at location x and y .

With I_{sky} and I_{ground} as constants, the only variables in Equations 3 and 4 are m and b , and Equation 4 can be re-written as Equation 5:

$$E_{RMS} = f(m, b) \quad (5)$$

Values for m and b were found by minimizing E_{RMS} in Equation 5. This minimization was performed using OLS. OLS is a stepwise procedure. As the model horizon approached the true horizon, the errors in both sky and ground were reduced and the values for E_{RMS} were reduced. The roll angle was determined from m using Equation 6:

$$\phi = \tan^{-1}(m) \quad (6)$$

where, ϕ is the roll angle of the aircraft in radians and \tan^{-1} is the arctangent.

This process was repeated for each image in order to generate the roll angle as a function of time. Figure 5 shows the results. The vertical axis was the roll angle in degrees, and the horizontal axis was the GPS SOW. An “o” was used to plot the GPS/IMU solution, and a “+” was used to plot the roll angle derived from the automated horizon extraction algorithm. The time was offset by 486,998 seconds for clarity in the graph. The image roll angle lagged the GPS/IMU roll angle by a few seconds, and the image roll angle was slightly less than the GPS/IMU roll angle.

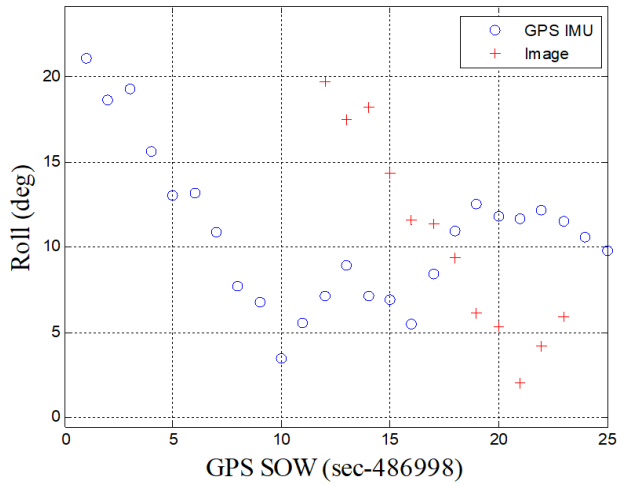


Figure 5. Roll angle from GPS/IMU “o”, and image horizon “+” verses time in seconds.

Time Synchronization

Cross correlation was performed on the data segment in Figure 5. This resulted in an image lag time of 11 seconds, and a roll offset of +1.386 degrees. Eleven seconds was the

time-stamp error for this portion of the data set. The offset of +1.386 degrees was the mechanical offset, in roll, of the camera. Figure 6 shows the data from Figure 5 that were replotted with these roll and time offsets. One possibility for the time error is that the image buffer contained 11 saved images. The images were named and written to disk 11 seconds after they were captured and, therefore, time stamped with an error of 11 seconds. As the number of images in the image buffer changed during the flight, the time error also changed. The process was repeated for additional segment of data to correct the entire data set. The error standard deviation for the data in Figure 6 was 0.186 degrees.

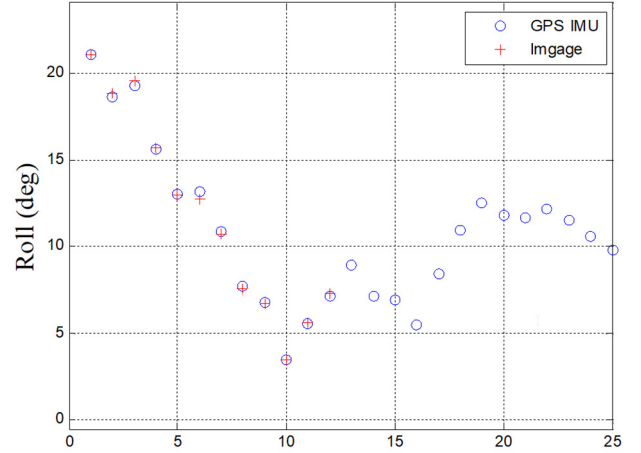


Figure 6. Image roll was shifted by -11 seconds in time and +1.386 degrees in roll.

Conclusions

The OU Baron flight test of May 5, 2016, was rendered unusable, due to timing errors between the GPS/IMU data and the image data. These errors were observable in the timing of the aircraft banking maneuvers. A simplified horizon extraction algorithm was developed to extract the aircraft roll angle from the image data. The roll angle was then correlated with the roll derived from the GPS/IMU data to extract the image time error. The results of one segment of data were described in this paper. Since the time error changed during the flight test, the process was repeated for other segments of the flight. The algorithm’s success was due in part to the flight test conditions. In this flight test, the horizon was a straight line. There was a distinct change in the image intensity at the horizon. The horizon was approximately in the center of the image providing high observability. Other situations, including mountainous areas, low contrast, or other camera angles, may be less suited to this technique. Under these favorable circumstances, the horizon algorithm provided an accurate means of roll extraction from imagery with a standard deviation of 0.186 degrees. The algorithm allowed the recovery of useful data from this flight test.

References

- Ahmad, T., Bebis, G., Nicolescu, M., Nefian, A., & Fong, T. (2015). *An edge-less approach to horizon line detection*. Paper presented at the 2015 IEEE 14th International Conference on Machine Learning and Applications (ICMLA), Miami, Florida, December 9-11 (pp. 1095-1102).
- Bouyssounouse, X., Nefian, A., Thomas, A., Edwards, L., Deans, M., & Fong, T. (2016). *Horizon based orientation estimation for planetary surface navigation*. Paper presented at the 2016 IEEE International Conference on Image Processing (ICIP), Phoenix, Arizona, September 25-28 (pp. 4368-4372).
- Carrio, A., Bavle, H., & Campoy, P. (2018). Attitude estimation using horizon detection in thermal images. *International Journal of Micro Air Vehicles*, 10(4), 352-361.
- Cohenour, C. (2019). A diagnostic clock for verification of image time synchronization. *International Journal of Engineering Research and Innovation*, 11(1), 37-45.
- Cohenour, C., Price, R., Rovito, T., & van Graas, F. (2015a). Camera models for the wright patterson air force base (wpafb) 2009 wide area motion imagery (wami) data set. *IEEE Aerospace & Electronic Systems Magazine*, 30(6), 4-15.
- Cohenour, C., Price, R., Rovito, T., & van Graas, F. (2015b). Corrected pose data for the wright patterson air force base (wpafb) 2009 wide area motion imagery (wami) data set. *SPIE Journal of Applied Remote Sensing*, 9(1), 096048.
- Crisman, D. (2016). *Horizon Detection in the Visible Spectrum*. Retrieved from <https://apps.dtic.mil/dtic/tr/fulltext/u2/1029726.pdf>
- Fischer, K., & Raquet, J. (2011). Precision position, navigation, and timing without the global positioning system. *Air and Space Power Journal*, 25(2), pp. 24-33.
- Kariya, T., & Kurata, H. (2004). *Generalized Least Squares*. Hoboken: Wiley.

with the Air Force Research Laboratory in Dayton, Ohio, aimed at understanding and correcting image georegistration errors from several airborne platforms. Dr. Cohenour may be reached at cohenour@ohio.edu

Biography

CURTIS COHENOUR is an assistant professor in the Department of Engineering Technology and Management at Ohio University. He received his BS from West Virginia Institute of Technology in 1980, MS from Ohio University in 1988, and PhD in Electrical Engineering from Ohio University in 2009. He is a registered professional engineer in West Virginia and Ohio. Dr. Cohenour has worked in industry as an electrical engineer in the areas of control systems, automation, and power. He joined Ohio University in 2002 as a research engineer working for the Ohio University Avionics Engineering Center. He has worked on projects covering a wide variety of avionics and navigation systems such as the Instrument Landing System (ILS), Microwave Landing System (MLS), Distance Measuring Equipment (DME), LAAS, WAAS, and GPS. His recent work includes research

DEEP NEURAL NETWORKS AND UNIVERSAL APPROXIMATORS

Ying Liu, Savannah State University; Asad Yousuf, Savannah State University

Abstract

There are many studies of approximations by deep neural networks. In this paper, the authors provide yet another proof that deep neural networks are universal approximators. An arbitrary binary target function can be effectively rewritten in terms of a set of strings, or a set of subsets. The authors show that a single hidden neuron can identify, and only identify, a single string or a single subset; therefore, an arbitrary binary target function can be effectively rewritten in the form of a deep neural network, thereby proving that deep neural networks can effectively implement any target mappings.

Introduction

Neural networks and deep learning currently provide the best solutions to many supervised learning problems. In 2006, a study (Hinton, Osindero, & Teh, 2006) was done, which introduced the idea of deep neural networks that use greedy layer-wise training (LeCun, Bengio, & Hinton, 2015), or train layers sequentially starting from the bottom (input) layer. The deep neural network first trains a simple supervised model then adds a new layer on top and trains the parameters for the new layer alone. Layers are continuously added and trained in this fashion until a deep network is established (Bengio, 2009; TensorFlow, 2017; Torch, 2017; Theano, 2017; Coursera, 2017; Bengio, Courville, & Vincent, 2013; Schmidhuber, 2015; Ciresan, Meier, & Schmidhuber, 2012).

Hinton's (2006) initial attempt was to train one layer at a time; deep neural networks, however, can train all layers together. Examples include TensorFlow (2017), Torch (2017), and Theano (2017). Google's TensorFlow is an open source software library for dataflow programming across a range of tasks. It is a symbolic math library used for machine learning applications such as neural networks (Amari, Kurata, & Nagaoka, 1992; Byrne, 1992; Kubat, 2015) and as well for both research and production at Google. Torch (2017) is an open source machine learning library and a scientific computing framework. Theano (2017) is a numerical computation library for Python. The approach using the single training of multiple layers gives advantages to neural networks over other learning algorithms. One question is the existence of a solution for a given problem. This will often be followed by an effective solution development (i.e., an algorithm for a solution). This will often be followed by the stability of the algorithm, itself then followed by an efficiency study of solutions in terms of time complexity and

space complexity. Although these theoretical approaches are not necessary for the empirical development of practical algorithms, the theoretical studies do advance the understanding of the problems. The theoretical studies will prompt new and better algorithm development for practical problems.

Hornik, Stinchcombe, and White (1989) established that the standard multi-layer feed-forward networks with hidden layers using arbitrary squashing functions are capable of approximating any measurable function from one finite dimensional space to another to any desired degree of accuracy, provided a sufficient number of hidden units are available. In this sense, multi-layer feed-forward networks are a class of universal approximators. Deep belief networks (DBN) are generative neural network models with many layers of hidden explanatory factors, recently introduced by Hinton et al. (2006) along with a greedy layer-wise unsupervised learning algorithm. The building block of a DBN is a probabilistic model called a restricted Boltzmann machine (RBM), used to represent one layer of the model. Restricted Boltzmann machines are interesting because they have been successfully used as building blocks for training deeper models. Le Roux and Bengio (2008) proved that adding hidden units yields strictly improved modeling power, and that RBMs are universal approximators of discrete distributions.

Liu (1993; 1995; 1997b; 2002; 2018b; 2018c) and Liu and Wang (2018) proved that the implementation of deep neural networks affords a complete expansion that can be used to expand any target functions. Cheng, Li, and Lu (2019) introduced a type of convolutional neural network that can implement the Fourier and local Fourier transformations for approximation in a large class of problems. Cybenko (1989) showed that a finite sum of any continuous sigmoid function could be used to approximate any univariate function using functional analysis. In this paper, the authors provide yet another proof that deep neural networks are universal approximators. The advantage of this proof is that it is very simple and effective. An arbitrary binary target function can be effectively rewritten in the form of a deep neural network, thus proving that deep neural networks can implement any target mappings. This has real applications, as many universities offer machine learning courses. If students take courses on differential equations or partial differential equations before machine learning, they are taught how to think about the sequence of questions to ask: 1) existence of solutions; 2) effective solutions; 3) stability of solutions; and, 4) efficiency of solutions. This will become a challenge to machine learning instructors. A typical

textbook (Kubat, 2015) will state something like this: Mathematicians have been able to prove that neural networks are universal approximators, but theorems do not explain how to construct a neural network. In this paper, the authors will completely solve the problem of the existence of solutions and the problem of effective solutions in the classrooms.

In this paper, the authors will explain how a deep neural network (DNN) is an artificial neural network (ANN) with multiple hidden layers between the input and output layers, and then discuss basic notation that shows that an arbitrary binary target function can be effectively rewritten in terms of a set of strings, or a set of subsets. Using simple examples to illustrate the idea in detail, the authors also prove that an arbitrary binary target function can be effectively rewritten in the form of a deep neural network, thus proving that deep neural networks can effectively implement any target mappings, and that multi-valued and continuous-valued deep neural networks extend this algorithm to multi-valued neurons and continuous-valued neurons.

Basic Notation

An arbitrary binary target function can be effectively rewritten in terms of a set of strings, or a set of subsets, in which binary neurons are used (Amari et al., 1992; Byrne, 1992; Kubat, 2015). An input instance is $00 \dots 0$, or $0 \dots 01$, etc. An instance space (Kubat, 2015), or Universe, is a set of all instances, as given in Equation 1:

$$X = \{0 \dots 00, 0 \dots 01, 0 \dots 11, \dots\} \quad (1)$$

Let d be the number of variables, $X = \{0, 1\}^d$ and $|X| = 2^d$.

A target function, or concept, or truth, C , is a mapping, where $C: X \rightarrow Y$. Without loss of generality, it is assumed there is only one variable in Y for now. For the case of multiple variables in Y , it is treated as multiple mappings. A hypothesis, h , where $h: X \rightarrow Y$, is an approximation of the target function, C . All hypotheses together form the hypothesis space (Kubat, 2015), as given in Equation 2:

$$H = \{h_0, h_1, h_2, \dots, h_{|H|-1}\} \quad (2)$$

For each instance $x \in X$:

00... 00
00... 01
...
11 ... 11

where, $y \in Y$ can be 0 or 1, giving $|H| = 2^{|X|}$ hypotheses (Kubat, 2015).

For example,

x_0	x_1	x_2	h_0	h_1	h_2
0	0	0	0	1	0
0	0	1	0	0	1
0	1	0	0	0	0
0	1	1	0	0	0
1	0	0	0	0	0
1	0	1	0	0	0
1	1	0	0	0	0
1	1	1	0	0	0

A mapping can be divided into two groups by the output variable, where $y = 0$ or 1 ; keeping one group will automatically infer the other group. For example:

x_0	x_1	x_2	y
0	0	0	0
0	0	1	1
0	1	0	0
0	1	1	1
1	0	0	1
1	0	1	0
1	1	0	0
1	1	1	0

can be rewritten as:

x_0	x_1	x_2	y
0	0	1	1
0	1	1	1
1	0	0	1

Furthermore, since all of the values in the last column are the same, these values can be omitted, yielding:

x_0	x_1	x_2
0	0	1
0	1	1
1	0	0

Now let d be the number of variables in the instance space, $X = \{0, 1\}^d$, a mapping, $h: X \rightarrow Y$, is simply a set of strings or a subset of $X = \{0, 1\}^d$. For the above example, the mapping is given by Equation 3:

$$h = \{001, 022, 100\} \quad (3)$$

Once again, only the variables with values of 1's are kept, and those variables with value of 0's are omitted; because if one set of variables is known, the other set of variables can be inferred. Let $\{0, 1, 2, \dots, d-1\}$ be used to represent these variables. For example:

$$\begin{aligned} 001 &\rightarrow \{x_0 = 0, x_1 = 0, x_2 = 1\} \\ &\rightarrow \{x_2 = 1\} \\ &\rightarrow \{2\} \end{aligned}$$

Now a mapping, $h: X \rightarrow Y$, is simply a set of subsets of $\{0, 1, 2, \dots, d-1\}$. In the above example, the mapping is given by Equation 4:

$$h = \{\{2\}, \{1, 2\}, \{0\}\} \quad (4)$$

To summarize, given an arbitrary binary target function, it can be effectively rewritten in terms of a set of strings or a set of subsets given in Equation 5 and 6:

$$h = \{s_0, s_1, s_2, \dots\} \quad (5)$$

$$s_i \subseteq \{0, 1, 2, \dots, d-1\} \quad (6)$$

Rewrite a Mapping in Terms of a Deep Neural Network

A single string or a single subset can be identified by a single hidden neuron and this neuron will only identify the string or the subset; therefore, an arbitrary binary target function can be effectively rewritten in the form of a deep neural network. Without loss of generality, it is assumed that there is only one variable in Y for now. For the case of multiple variables in Y , it is treated as multiple mappings. The deep neural network used here will have one input layer, one output layer, and one hidden layer. The neuron values are given by Equation 7 (Amari et al., 1992; Byrne, 1992; Kubat, 2015):

$$y_i = f(\sum w_{ij} x_j + b_i), i = 1, 2, 3, \dots \quad (7)$$

where, f is a sigmoid function given by Equation 8:

$$f(x) = \frac{1}{1 + e^{-x}} \quad (8)$$

Given an arbitrary target function, as noted previously, it can be rewritten as indicated by Equations 9 and 10:

$$h = \{s_0, s_1, s_2, \dots\} \quad (9)$$

$$s_i \subseteq \{0, 1, 2, \dots, d-1\} \quad (10)$$

The construction of a DNN is simple:

- The input layer has d neurons.
- Each neuron in the hidden layer identifies one string in a target function, $h = \{s_0, s_1, \dots\}$, so the number of neurons in the hidden layer is $|h|$, which is the number of strings or the number of subsets.

- The output layer has one neuron; the neuron value is 1, if any one of hidden the layer neurons is 1.

To compute the connection weights, a constant, L , will be introduced; without a loss of generality, let $L = 10$. Next, the connection weight for one hidden neuron will be computed. Assume s is a subset in a mapping, h , and assume a hidden neuron will identify s . Let s be a subset given by Equations 11 and 12:

$$\{j_0, j_1, j_2, \dots\} \quad (11)$$

$$s \subseteq \{0, 1, 2, \dots, d-1\} \quad (12)$$

To assign connection weights:

- For each of the input neurons, j_0, j_1, j_2, \dots , the connection weights from the hidden neuron to j_0, j_1, j_2, \dots are L .
- For all other input neurons, the connection weights are $-L$.
- Set the bias to be $-(|s| - 1) \cdot L$.

The proof that this simple ANN will implement a target function is explained as follows. Assuming an input string is, $s = \{j_0, j_1, j_2, \dots\}$, this string will be identified by a hidden neuron with weight, L , for input neurons $\{j_0, j_1, j_2, \dots\}$, and weight, $-L$, for all other input neurons. This neuron has d weights because there are d input-neurons. The number of weights, with value of L , is $|s|$, and the number of weights, with value of $-L$, is $(d - |s|)$. For the original string, s , the weighted sum of inputs is given by Equation 13:

$$\begin{aligned} &\sum (w_{ij} x_j) + b_i \\ &= (|s| \cdot L \cdot 1) + (d - |s|) \cdot (-L) \cdot 0 - (|s| - 1) \cdot L \\ &= |s| \cdot L + 0 - |s| \cdot L + L = L \end{aligned} \quad (13)$$

where, $(|s| \cdot L \cdot 1) = |s| \cdot L$ is the contribution for the input neurons with the value of 1; there are $|s|$ such terms; the connection weights are L ; and 1 is the input neuron value.

and where, $(d - |s|) \cdot (-L) \cdot 0 = 0$ is the contribution for the input neurons with the value of 0; there are $(d - |s|)$ such terms; the connection weights are $-L$; and 0 is the input neuron value.

and where, $-(|s| - 1) \cdot L = -|s| \cdot L + L$ is the bias.

At this time, a single bit in the string, s , will be changed. First, a single bit in s with a value of 1 is changed to 0, so the number of 1's is $(|s| - 1)$ and the number of 0's is $(d - |s|)$ for connection weights of $-L$ and number of 0's is 1 for connection weights of L , therefore, the weighted sum of inputs is given by Equation 14:

$$\sum(w_{ij}x_j) + b_i = (|s|-1) \cdot L \cdot 1 + 1 \cdot L \cdot 0 + (d-|s|) \cdot (-L) \cdot 0 - (|s|-1) \cdot L = 0 \quad (14)$$

Secondly, if a single bit of 0's in string, s , is changed to 1's, so the number of 0's is $(d - |s| - 1)$, and one neuron has both value 1 and weight $(-L)$, therefore, the weighted sum of inputs is given by Equation 15:

$$\sum(w_{ij}x_j) + b_i = (|s| \cdot L \cdot 1) + (d - |s| - 1) \cdot (-L) \cdot 0 + 1 \cdot (-L) \cdot 1 - (|s| - 1) \cdot L = 0 \quad (15)$$

Similarly, if two of the 1's in string, s , are changed to 0's, the weighted sum of inputs is given by Equation 16:

$$\sum(w_{ij}x_j) + b_i = (|s| - 2) \cdot L \cdot 1 + 2 \cdot L \cdot 0 + (d - |s|) \cdot (-L) \cdot 0 - (|s| - 1) \cdot L = -L \quad (16)$$

If two of the 0's in string, s , are changed to 1's, so the number of 0's is $(d - |s| - 2)$, and two neurons have both value 1 and weight $(-L)$, therefore, the weighted sum of inputs is given by Equation 17:

$$\sum(w_{ij}x_j) + b_i = (|s| \cdot L \cdot 1) + (d - |s| - 2) \cdot (-L) \cdot 0 + 2 \cdot (-L) \cdot 1 - (|s| - 1) \cdot L = -L \quad (17)$$

If a single bit of 0's in string, s , is changed to 1's, and a single bit of 1's is changed to 0's, the result is still $-L$. If an input string differs from the given string, s , by 0 bit, 1 bit, 2 bits, 3 bits, ..., the weighted sums of inputs are given by Equation 18:

$$\sum(w_{ij}x_j) + b_i = L, 0, -L, -2L, \dots \quad (18)$$

Let the hidden layer be given by Equation 19:

$$\{m_0, m_1, m_2, \dots\} \quad (19)$$

and the neuron values given by Equations 20 and 21:

$$m_i = f\left(\sum w_{ij}x_j + b_i\right), i = 1, 2, 3, \dots \quad (20)$$

$$f(x) = \frac{1}{1 + e^{-x}} \quad (21)$$

Let a neuron, m , be the hidden neuron to identify the string, s ; the hidden neuron will identify the correct string with a value given by Equation 22:

$$m = \frac{1}{1 + e^{-L}} \approx 1 \quad (22)$$

If there is a single bit difference, the hidden neuron will identify the string with a value given in Equation 23:

$$m = \frac{1}{1 + e^0} \approx 0.5 \quad (23)$$

If there is a two-bit difference, the hidden neuron will identify the string with a value given in Equation 24:

$$m = \frac{1}{1 + e^L} \approx 0 \quad (24)$$

If an input string differs from the string, s , by 0 bit, 1 bit, 2 bits, 3 bits, ..., the hidden neuron will identify the string with values given in Equation 25:

$$m = 1, 0.5, 0, 0, \dots \quad (25)$$

This hidden neuron can clearly identify only one string, or one subset, s . From the previous section, a target function is written in terms of a set of subsets. For each subset in the target function, there is one hidden neuron that can identify it and only it. The hidden layer has one neuron for each subset, so the neural network can implement the target function.

Examples

Figure 1 is an example of how to identify simple digits (Kubat, 2015). Each digit is converted into 7 bits: 0, 1, ..., 6. Figure 2 shows the bit location.



Figure 1. An example of how to identify simple digits.

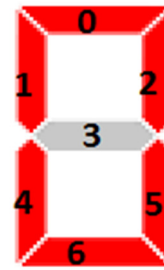


Figure 2. Input bit assignments.

The 10 input vectors for the digits in Figure 2 have 7 bits and are given by Equation 26:

$$\begin{aligned} I_0 & (1, 1, 1, 0, 1, 1, 1) \\ I_1 & (0, 0, 1, 0, 0, 1, 0) \\ I_2 & (1, 0, 1, 0, 1, 0, 1) \\ & \dots \\ I_9 & (1, 1, 1, 1, 0, 1, 1) \end{aligned} \quad (26)$$

where I_0 is an image of “0”, I_1 is an image of “1”, The 10 output vectors for digits in Figure 2 have 10 bits and are given by Equation 27:

$$\begin{aligned} O_0 & (1,0,0,0,0,0,0,0,0,0) \\ O_1 & (0,1,0,0,0,0,0,0,0,0) \\ O_2 & (0,0,1,0,0,0,0,0,0,0) \\ & \dots \\ O_9 & (0,0,0,0,0,0,0,0,0,1) \end{aligned} \quad (27)$$

Let the hidden layer be given by Equation 28:

$$\{m_0, m_1, m_2, \dots\} \quad (28)$$

Let m_0 identify $I_0 = (1, 1, 1, 0, 1, 1, 1)$, which can also be written as a subset $\{0, 1, 2, 4, 5, 6\}$. The connection weights for m_0 are L to the input neurons $\{0, 1, 2, 4, 5, 6\}$ and $-L$ to the rest of the input neurons. Together the connection weights are $\{10, 10, 10, -10, 10, 10, 10\}$. Similarly, let m_1 identify $I_1 = (0, 0, 1, 0, 0, 1, 0)$, the connection weights are $\{-10, -10, 10, -10, -10, 10, -10\}$; the m_2 connection weights are $\{10, -10, 10, 10, 10, -10, 10\}$, etc. This 3-layer neural network will classify the 10 digits correctly.

Another example is to identify ASCII codes from A to Z. The 26 input vectors for A to Z have 8 bits and are given by Equation 29:

$$\begin{aligned} I_A & = 01000001, \\ I_B & = 01000010, \\ & \dots \end{aligned} \quad (29)$$

The 26 output vectors for A-Z have 26 bits and are given by Equation 30:

$$\begin{aligned} O_A & = 10000\dots, \\ O_B & = 01000\dots, \\ & \dots \end{aligned} \quad (30)$$

Let the hidden layer be given by Equation 31:

$$\{m_A, m_B, \dots, m_Z\} \quad (31)$$

Let m_A identify $I_A = (0, 1, 0, 0, 0, 0, 0, 1)$, which can also be written as a subset $\{1, 7\}$. The connection weights for m_A are $\{-10, 10, -10, -10, -10, -10, -10, 10\}$. Similarly, let m_B identify $I_B = (0, 1, 0, 0, 0, 0, 1, 0)$, the connection weights for m_B are $\{-10, 10, -10, -10, -10, -10, 10, -10\}$.

Multi- and Continuous-Valued Deep Neural Networks

Multi-valued neurons can be an extension of binary neurons via multiple-valued logic (Aizenberg, 2011), where the value of a neuron depends on the argument of an underlying complex

number, z . The argument of z is in $[0, 2\pi)$, which can be divided into k sectors. If z 's argument is located in the j^{th} sector: $2\pi j / k \leq \arg(z) < 2\pi (j+1) / k$, then the neuron value is mapped into integer value j . A multi-valued function can also be directly approximated with binary neurons. Assuming that a multi-value neuron has k different values, it can then be converted into a certain number of binary neurons. The mappings from k -valued integers to binary neurons are not unique, and different mappings will result in different performance results. Liu (1997a) found, based on stock market data experiments, that the best mapping from a k -value integer to k binary neurons is given by Equation 32 or Equation 33:

$$\begin{aligned} 0 & \rightarrow \dots 000001 \\ 1 & \rightarrow \dots 000011 \end{aligned} \quad (32)$$

or

$$\begin{aligned} k-1 & \rightarrow \dots 000001 \\ k-2 & \rightarrow \dots 000011 \end{aligned} \quad (33)$$

An arbitrary k -value target function can be effectively rewritten in the form of a binary target function, which can be further rewritten into a deep neural network. A continuous-valued neuron can also be approximated by k multi-valued neurons, where k is very large.

Conclusions

Hornik et al. (1989) showed that multi-layer feed-forward networks with enough hidden layers are universal approximators. Le Roux and Bengio (2008) showed that the restricted Boltzmann machines are universal approximators of discrete distributions. Liu and Wang (2008) proved that deep neural networks can implement an expansion and that the expansion is complete, which can then be used to expand any target functions. Cheng, Li, and Lu (2019) introduced a type of convolutional neural network that can implement the Fourier and local Fourier transformations for approximation in a large class of problems. Cybenko (1989) showed that a finite sum of any continuous sigmoid function can be used to approximate any univariate function using functional analysis. In this paper, the authors provided yet another proof. The advantage of this proof is that it is very simple. An arbitrary binary target function can be effectively rewritten in terms of a set of strings, or a set of subsets. It was shown that a single hidden neuron can identify a single string or a single subset; therefore, an arbitrary binary target function can be effectively rewritten in the form of a deep neural network, thus proving that deep neural networks can effectively implement any target mappings. The authors did not seek efficient implementation of deep neural networks in terms of low time complexity and space complexity, given an arbitrary target function. They simply meant to prove that it is effectively possible to implement any target function by using deep neural networks.

Acknowledgments

The authors would like to thank Gina Porter for proof reading this paper.

References

- Aizenberg, I. (2011). *Complex-Valued Neural Networks with Multi-Valued Neurons*. (1st ed.). Springer-Verlag.
- Amari, S., Kurata, K., & Nagaoka, H. (1992). Information Geometry of Boltzmann Machine. *IEEE Trans., Neural Network*, 3(2), 260-271.
- Bengio, Y. (2009). Learning Deep Architectures for AI. *Foundations and Trends in Machine Learning*, 2(1), 1-127. Retrieved from <http://dx.doi.org/10.1561/2200000006>
- Bengio, Y., Courville, A., & Vincent, P. (2013). Representation Learning: A Review and New Perspectives. *IEEE Transactions on Pattern Analysis and Machine Intelligence*, 35(8), 1798-1828. Retrieved from doi:10.1109/tpami.2013.50.
- Byrne, W. (1992). Alternating Minimization and Boltzmann Machine Learning. *IEEE Trans., Neural Network*, 3(4), 612-620.
- Cheng, X., Li, Y., & Lu, J. (2019). Butterfly-Net: Optimal Function Representation Based on Convolutional Neural Networks. Retrieved from <https://arxiv.org/pdf/1805.07451>
- Ciresan, D., Meier, U., & Schmidhuber, J. (2012). Multicolumn deep neural networks for image classification. 2012 IEEE Conference on Computer Vision and Pattern Recognition, 3642-3649. Retrieved from doi:10.1109/cvpr.2012.6248110.
- Coursera. (2017). Coursera, Your Course to Success. Retrieved from <https://www.coursera.org/>
- Cybenko, G. (1989). Approximation by Superposition of a sigmoid function. *Mathematics of Control, Signals, and System*, 2, 303-314.
- Hinton, G. E., Osindero, S., & Teh, Y. (2006). A Fast Learning Algorithm for Deep Belief Nets. *Neural Computation*, 18, 1527-1554.
- Hornik, K., Stinchcombe, M., & White, H. (1989). Multilayer Feedforward Networks are Universal Approximators. *Neural Networks*, 2, 359-366.
- Kubat, M. (2015). *An Introduction to Machine Learning*. (1st ed.). Springer.
- Le Roux, N., & Bengio, Y. (2008). Representational Power of Restricted Boltzmann Machines and Deep Belief Networks. *Neural Computation*, 20(6), 1631-1649.
- LeCun, Y., Bengio, Y., & Hinton, G. (2015). Deep Learning. *Nature*, 521(7553), 436-444.
- Liu, Y. (1993). Image Compression Using Boltzmann Machines. *Proc. SPIE*, 2032, 103-117.
- Liu, Y. (1995). Boltzmann Machine for Image Block Coding. *Proc. SPIE*, 2424, 434-447.
- Liu, Y. (1997a). High Order Polytomous Boltzmann Machine and Forecasting Time Series I. *Proc. SPIE*, 3077, 396-408.
- Liu, Y. (1997b). Character and Image Recognition and Image Retrieval Using the Boltzmann Machine. *Proc. SPIE*, 3077, 706-715.
- Liu, Y. (2002). Attrasoft Image Retrieval. US Patent, 7,773,800. Retrieved from <http://www.google.com/patents/US7773800>
- Liu, Y., & Wang, S. H. (2018). Completeness Problem of the Deep Neural Networks. *American Journal of Computational Mathematics*, 8, 184-196. Retrieved from <https://doi.org/10.4236/ajcm.2018.82014>
- Liu, Y. (2018). Linear Neurons and Their Learning Algorithms. *Journal of Computer Science and Information Technology*, 6(2), 1-14.
- Liu, Y. (2018). Square Neurons, Power Neurons, and Their Learning Algorithms. *American Journal of Computational Mathematics*, 8, 296-313. Retrieved from <https://doi.org/10.4236/ajcm.2018.84024>
- Schmidhuber, J. (2015). Deep Learning in Neural Networks: An Overview. *Neural Networks*, 61, 85-117. Retrieved from doi:10.1016/j.neunet.2014.09.003.
- Theano, (2019). Theano 1.0. Retrieved from <http://deeplearning.net/software/theano/Tensorflow>
- Tensorflow. Retrieved from <https://www.tensorflow.org>
- Torch, (2019). Torch, A scientific computing framework for LuaJIT. Retrieved from <http://torch.ch>

Biographies

YING LIU is an Associate Professor of Computer Science Technology at Savannah State University. He received his MS and PhD degrees in physics from Carnegie-Mellon University, and a master's degree in computer science from the University of South Carolina. Dr. Liu has multiple Microsoft certifications, including MCSE (Microsoft Certified System Engineer) and MCDBA (Database Administrator). He has published over 60 research papers, and holds one patent and over 30 software copyrights. Dr. Liu has extensive experience in software research, and development in image recognition. Dr. Liu may be reached at liuy@savannahstate.edu

ASAD YOUSUF is the Chair of the Department of Engineering Technology at Savannah State University. He received his BS in Electrical Engineering from NED University, MS in Electrical Engineering from the University of Cincinnati with an emphasis on computer systems, and his doctorate from the University of Georgia. He has published several papers in technical journals and conference proceedings. He has years' of experience in managing federally funded grants, having received over \$2.5M in grant awards in the last few years. Dr. Yousuf may be reached at yousufa@savannahstate.edu

INSTRUCTIONS FOR AUTHORS: MANUSCRIPT FORMATTING REQUIREMENTS

The INTERNATIONAL JOURNAL OF MODERN ENGINEERING is an online/print publication designed for Engineering, Engineering Technology, and Industrial Technology professionals. All submissions to this journal, submission of manuscripts, peer-reviews of submitted documents, requested editing changes, notification of acceptance or rejection, and final publication of accepted manuscripts will be handled electronically. The only exception is the submission of separate high-quality image files that are too large to send electronically.

All manuscript submissions must be prepared in Microsoft Word (.doc or .docx) and contain all figures, images and/or pictures embedded where you want them and appropriately captioned. Also included here is a summary of the formatting instructions. You should, however, review the [sample Word document](http://ijme.us/formatting_guidelines/) on our website (http://ijme.us/formatting_guidelines/) for details on how to correctly format your manuscript. The editorial staff reserves the right to edit and reformat any submitted document in order to meet publication standards of the journal.

The references included in the References section of your manuscript must follow APA-formatting guidelines. In order to help you, the sample Word document also includes numerous examples of how to format a variety of scenarios. Keep in mind that an incorrectly formatted manuscript will be returned to you, a delay that may cause it (if accepted) to be moved to a subsequent issue of the journal.

1. **Word Document Page Setup:** Two columns with $\frac{1}{4}$ " spacing between columns; top of page = $\frac{3}{4}$ "; bottom of page = 1" (from the top of the footer to bottom of page); left margin = $\frac{3}{4}$ "; right margin = $\frac{3}{4}$ ".
2. **Paper Title:** Centered at the top of the first page with a 22-point Times New Roman (Bold), small-caps font.
3. **Page Breaks:** Do not use page breaks.
4. **Figures, Tables, and Equations:** All figures, tables, and equations must be placed immediately after the first paragraph in which they are introduced. And, each must be introduced. For example: "Figure 1 shows the operation of supercapacitors." "The speed of light can be determined using Equation 4:"
5. **More on Tables and Figures:** Center table captions above each table; center figure captions below each figure. Use 9-point Times New Roman (TNR) font. Italicize the words for table and figure, as well as their respective numbers; the remaining information in the caption is not italicized and followed by a period—e.g., "*Table 1*. Number of research universities in the state." or "*Figure 5*. Cross-sectional aerial map of the forested area."
6. **Figures with Multiple Images:** If any given figure includes multiple images, do NOT group them; they must be placed individually and have individual minor captions using, "(a)" "(b)" etc. Again, use 9-point TNR.
7. **Equations:** Each equation must be numbered, placed in numerical order within the document, and introduced—as noted in item #4.
8. **Tables, Graphs, and Flowcharts:** All tables, graphs, and flowcharts must be created directly in Word; tables must be enclosed on all sides. The use of color and/or highlighting is acceptable and encouraged, if it provides clarity for the reader.
9. **Textboxes:** Do not use text boxes anywhere in the document. For example, table/figure captions must be regular text and not attached in any way to their tables or images.
10. **Body Fonts:** Use 10-point TNR for body text throughout (1/8" paragraph indentation); indent all new paragraphs as per the images shown below; do not use tabs anywhere in the document; 9-point TNR for author names/affiliations under the paper title; 16-point TNR for major section titles; 14-point TNR for minor section titles.

11. **Personal Pronouns:** Do not use personal pronouns (e.g., "we" "our" etc.).
12. **Section Numbering:** Do not use section numbering of any kind.
13. **Headers and Footers:** Do not use either.

-
14. **References in the Abstract:** Do NOT include any references in the Abstract.
 15. **In-Text Referencing:** For the first occurrence of a given reference, list all authors—last names only—up to seven (7); if more than seven, use “et al.” after the seventh author. For a second citation of the same reference—assuming that it has three or more authors—add “et al.” after the third author. Again, see the *sample Word document* and the *formatting guide for references* for specifics.
 16. **More on In-Text References:** If you include a reference on any table, figure, or equation that was not created or originally published by one or more authors on your manuscript, you may not republish it without the expressed, written consent of the publishing author(s). The same holds true for name-brand products.
 17. **End-of-Document References Section:** List all references in alphabetical order using the last name of the first author—last name first, followed by a comma and the author’s initials. Do not use retrieval dates for websites.
 18. **Author Biographies:** Include biographies and current email addresses for each author at the end of the document.
 19. **Page Limit:** Manuscripts should not be more than 15 pages (single-spaced, 2-column format, 10-point TNR font).
 20. **Page Numbering:** Do not use page numbers.
 21. **Publication Charges:** Manuscripts accepted for publication are subject to mandatory publication charges.
 22. **Copyright Agreement:** A copyright transfer agreement form must be signed by all authors on a given manuscript and submitted by the corresponding author before that manuscript will be published. Two versions of the form will be sent with your manuscript’s acceptance email.
 23. **Submissions:** All manuscripts and required files and forms must be submitted electronically to Dr. Philip D. Weinsier, manuscript editor, at philipw@bgsu.edu.
 24. **Published Deadlines:** Manuscripts may be submitted at any time during the year, irrespective of published deadlines, and the editor will automatically have your manuscript reviewed for the next-available issue of the journal. Published deadlines are intended as “target” dates for submitting new manuscripts as well as revised documents. Assuming that all other submission conditions have been met, and that there is space available in the associated issue, your manuscript will be published in that issue if the submission process—including payment of publication fees—has been completed by the posted deadline for that issue.

Missing a deadline generally only means that your manuscript may be held for a subsequent issue of the journal. However, conditions exist under which a given manuscript may be rejected. Always check with the editor to be sure. Also, if you do not complete the submission process (including all required revisions) within 12 months of the original submission of your manuscript, your manuscript may be rejected or it may have to begin the entire review process anew.

Only one form is required. Do not submit both forms!

The form named “paper” must be hand-signed by each author. The other form, “electronic,” does not require hand signatures and may be filled out by the corresponding author, as long as he/she receives written permission from all authors to have him/her sign on their behalf.



www.ijeri.org

Print ISSN: 2152-4157
Online ISSN: 2152-4165



www.iajc.org

INTERNATIONAL JOURNAL OF ENGINEERING RESEARCH AND INNOVATION

ABOUT IJERI:

- IJERI is the second official journal of the International Association of Journals and Conferences (IAJC).
- IJERI is a high-quality, independent journal steered by a distinguished board of directors and supported by an international review board representing many well-known universities, colleges, and corporations in the U.S. and abroad.
- IJERI has an impact factor of **1.58**, placing it among an elite group of most-cited engineering journals worldwide.

OTHER IAJC JOURNALS:

- The International Journal of Modern Engineering (IJME)
For more information visit www.ijme.us
- The Technology Interface International Journal (TIIJ)
For more information visit www.tiij.org

IJERI SUBMISSIONS:

- Manuscripts should be sent electronically to the manuscript editor, Dr. Philip Weinsier, at philipw@bgsu.edu.

For submission guidelines visit
www.ijeri.org/submissions

TO JOIN THE REVIEW BOARD:

- Contact the chair of the International Review Board, Dr. Philip Weinsier, at philipw@bgsu.edu.

For more information visit
www.ijeri.org/editorial

INDEXING ORGANIZATIONS:

- IJERI is currently indexed by 16 agencies. For a complete listing, please visit us at www.ijeri.org.

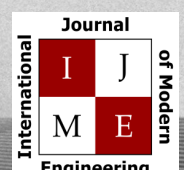
Contact us:

Mark Rajai, Ph.D.

Editor-in-Chief
California State University-Northridge
College of Engineering and Computer Science
Room: JD 4510
Northridge, CA 91330
Office: (818) 677-5003
Email: mrajai@csun.edu



www.tiij.org



www.ijme.us

THE LEADING JOURNAL OF ENGINEERING, APPLIED SCIENCE AND TECHNOLOGY

The latest impact factor (IF) calculation (Google Scholar method) for IJME of 3.0 moves it even higher in its march towards the top 10 engineering journals.

**IJME IS THE OFFICAL AND FLAGSHIP JOURNAL OF THE
INTERNATIONAL ASSOCIATION OF JOURNALS AND CONFERENCE (IAJC)**

www.iajc.org



The International Journal of Modern Engineering (IJME) is a highly-selective, peer-reviewed journal covering topics that appeal to a broad readership of various branches of engineering and related technologies. IJME is steered by the IAJC distinguished board of directors and is supported by an international review board consisting of prominent individuals representing many well-known universities, colleges, and corporations in the United States and abroad.

IJME Contact Information

General questions or inquiries about sponsorship of the journal should be directed to:

Mark Rajai, Ph.D.

Editor-in-Chief

Office: (818) 677-5003

Email: editor@ijme.us

Department of Manufacturing Systems Engineering & Management

California State University-Northridge

1811 Nordhoff St.

Northridge, CA 91330